Textured Ferroelectric Thin Films: Synthesis, Characterization, and Influence of Compositional Grading on the Dielectric Behavior

Thesis by

Mohamed Y. El-Naggar

In Partial Fulfillment of the Requirements

for the Degree of

Doctor of Philosophy

California Institute of Technology

Pasadena, California

2006

(Defended September 8, 2006)

To my loving parents, Suad El-Masry and Youssef El-Naggar.

Acknowledgements

I will begin by acknowledging the money. Most of the work in this thesis was funded by the Department of Defense MURI award DAAD19-01-1-0517, administered by the Army Research Office. For the last two years, I also enjoyed a generous fellowship from Applied Materials, Inc., for which I am truly grateful.

Money is important, but people make things happen. My parents, Suad El-Masry and Youssef El-Naggar, are in my biased opinion, the best parents in history. I am not only referring to the occasional check, but to an overall style of parenthood: a unique blend of unconditional support and inquisitiveness that has always driven me to succeed. My brothers and sisters have been especially understanding of my absence in the past few years. Their support has meant a great deal to me. Frank and Dolores Yanni have been my caretakers for many years now, and I am proud to consider them my second family. I don't know if I can ever reciprocate the favors they have done me, but I will cherish them forever.

Dave Goodwin is a true gentleman. His wisdom and quiet, imperturbable demeanor has influenced me greatly, in the most positive of ways. I have come to think of him as a true avatar of academic gentry. Dave, I am in your debt forever.

The other members of my Ph.D. committee, in their distinct ways, made this

thesis possible. Kaushik Bhattacharya helped me navigate through the world of active materials, and besides being one of the quickest people I know (perhaps not physically, but that remains to be proven on the racquetball court), he is a world-class teacher. He has that enviable ability to elucidate esoteric ideas but to also look beyond a problem's solution for real insight. Guruswami Ravichandran, who sometimes seems to have a hand in every research project at Caltech, is a role model for me. Almost every time I ran into him, he would motivate me by asking: "Are you writing more papers?" I often wondered if he was serious when he asked this same question twice, a few hours apart. I suspect he was! I am also grateful to Sossina Haile, who agreed to serve on my committee and who maintains a fantastic x-ray facility, of which I have been a real beneficiary.

David Boyd helped me get started from that very first summer at Caltech. Day to day, he was my lab-mate-in-arms, and I appreciate his help, guidance, and most important of all: his enthusiasm. I have no doubt that we will collaborate further in the future. I would also like to thank everyone in the Goodwin research group. The many lunches that we enjoyed at Dave's expense helped bring us closer together.

I thank my friends, Joe Klamo, Jen Ruglovsky, Kaushik Dayal, Sam Taira, Michael Wolf, Alex Taflanidis, Nick Hudson, Tim Chung, Kristo Kriechbaum, and Matt Dicken for many unforgettable lunch conversations and good times. Joe Klamo has been my roommate, personal comedian, and racquetball nemesis for a few years now. For helping me understand the infield fly rule, and for being there through the good and bad times, I am truly grateful. He, of course, has more reason to be grateful to

me, having introduced him to my collaborator and friend, Jen Ruglovsky. Jen always managed to make research more fun. Matt Dicken -a good man, and thorough- provided me with many samples and collaborated with me directly on the pulsed laser deposition portion of this thesis. Kaushik Dayal had a fundamental contribution to the work on compositionally-graded ferroelectrics, and I look forward to further collaborations with him. Our many coffee breaks at 3 p.m. are some of my best memories at Caltech.

Last, but first and foremost in my heart and mind, I thank the brilliant and beautiful Elizabeth for making life as wonderful as can be. I look forward to always having her by my side.

Abstract

This dissertation focuses on two topics concerning the connections between structure and property in ferroelectric thin films. First, the metalorganic chemical vapor deposition (MOCVD) and characterization of highly-oriented $Pb_xBa_{1-x}TiO_3$ thin films is addressed, where the texture is needed to generate high strains that rely on electromechanical domain switching in ferroelectrics. The ferroelectric films are integrated with $SrRuO_3$ oxide electrodes, produced by pulsed laser deposition (PLD), onto single crystal MgO and Si substrates using biaxially-textured MgO as buffer layers. The second topic focuses on modeling of compositionally-graded $Ba_xSr_{1-x}TiO_3$ ferroelectric thin films with the specific goal of understanding how the graded structure can achieve a high and temperature-stable dielectric response.

$Pb_xBa_{1-x}TiO_3$ ($0.2 \leq x \leq 1$) thin films were deposited using MOCVD on single crystal MgO as well as amorphous Si_3N_4/Si substrates using biaxially textured MgO buffer templates, grown by ion beam-assisted deposition (IBAD). The ferroelectric films were stoichiometric and highly-oriented, with only (00l) and (h00) orientations evident in XRD scans. Films on biaxially-textured templates had smaller grains (60 nm average) than those deposited on single crystal MgO (300 nm average). Electron backscatter diffraction (EBSD) has been used to study the microtexture on both

types of substrates, and the results were consistent with x-ray pole figures and TEM micrographs that indicated the presence of 90° domain boundaries, twins, in films deposited on single crystal MgO substrates. In contrast, films on biaxially-textured substrates consisted of small single domain grains that were either *c* or *a* oriented. The surface-sensitive EBSD technique was used to measure the tetragonal tilt angle as well as in-plane and out-of-plane texture. High temperature x-ray diffraction (HTXRD) of films with 90° domain walls indicated large changes, as much as 60%, in the *c* and *a* domain fractions with temperature, while such changes were not observed for PBT films on biaxially-textured $MgO/Si_3N_4/Si$ substrates, which lacked 90° domain boundaries.

Conductive oxide $SrRuO_3$ thin films were prepared by PLD, for the purpose of integration with ferroelectrics onto Si-based substrates for CMOS compatibility. The focus was again on achieving a high degree of texture so that $SrRuO_3$ films are used both as electrodes and growth templates for the textured active ferroelectric layers. The $SrRuO_3$ films were deposited on MgO and Si using biaxially textured MgO buffer layers. On both substrates, the films were predominantly $(00l)$ oriented and in-plane textured, as shown by x-ray pole figures. Out-of-plane and in-plane characterizations show that the $SrRuO_3$ films on Si inherit the biaxial texture of the IBAD MgO buffer layer, with full-width at half-max values of 4.3° and 9.7°, respectively. This approach led to the direct synthesis of $PbTiO_3/SrRuO_3/MgO/Si_3N_4/Si$ heterostructures, allowing for direct integration of active ferroelectric layers onto Si-based substrates.

The second topic of this thesis explores the dielectric behavior of functionally-

graded ferroelectric thin films. Homogenous ferroelectric films offer the possibility of engineering a tunable dielectric response for components in frequency-agile RF and microwave devices. However, this approach often leads to an undesired temperature sensitivity. Compositionally-graded ferroelectric films have been explored as a means of redressing this sensitivity, but experimental observations vary depending on geometry and other details. A continuum model is presented to calculate the capacitive response of graded ferroelectric films with realistic electrode geometries by accurately accounting for the polarization distribution and long-range electrostatic interactions. We show that graded c-axis poled $Ba_xSr_{1-x}TiO_3$ (BST) parallel plate capacitors are ineffective, while graded a-axis poled BST co-planar capacitors with interdigitated electrodes are extremely effective in obtaining high and temperature-stable dielectric properties.

Refereed Publications

El-Naggar M.Y., Dayal K., Goodwin D.G., Bhattacharya K., 2006. *Graded Ferroelectric Capacitors with Robust Temperature Characteristics.* To appear in J. Appl. Phys.

Boyd D.A., **El-Naggar M.Y.**, Goodwin D.G., 2006. *In Situ Measurements of Stress with Temperature in Thin Film* $Pb_xBa_{1-x}TiO_3$. To appear in Integr. Ferroelectr.

El-Naggar M.Y., Boyd D.A., Goodwin D.G., 2005. *Characterization of Highly-Oriented Ferroelectric* $Pb_xBa_{1-x}TiO_3$ *Thin Films grown by MOCVD.* 20 (11), J. Mater. Res.

Boyd D.A., **El-Naggar M.Y.**, Goodwin D.G., 2005. *In Situ Measurements of Macroscopic Film Stress during Growth, Cooling, and Thermal Cycling of Thin Film* $PbTiO_3$. 71: 21+, Integr. Ferroelectr.

Brewer R.T., Boyd D.A., **El-Naggar M.Y.**, Boland S.W., Park Y.B., Haile S.M., Goodwin D.G., Atwater H.A., 2005. *Growth of Biaxially Textured* $Ba_xPb_{1-x}TiO_3$ *Ferroelectric Thin Films on Amorphous* Si_3N_4. 97 (3), J. Appl. Phys.

Contents

List of Figures

List of Tables

Chapter 1

Introduction

There has been an upsurge of interest in ferroelectric materials over the past twenty years. The largest motives for the considerable scientific research done in this field have been the development of ferroelectric nonvolatile random access memories (FE-NVRAM) (Scott, 2000) as well as solid-state sensors/actuators. The interest seems to have largely paid off in the memory arena now that ferroelectric RAM is a commercial product[1] and future efforts focus on increasing the density and read/write speeds. In the ferroelectric sensors/actuators arena, commercial development focused on the direct electro-mechanical coupling in the linear regime. That is the coupling between polarization and stress in the direct piezoelectric effect as well as that between strain and electric field in the converse piezoelectric effect. Piezoelectricity was discovered by brothers Pierre and Jacques Curie in 1880 and has been used extensively since then in a wide range of devices: microphones, hydrophones, sound generators, accelerometers, motors, bulk wave filters, and many others. The main attraction has been the relative ease by which the functional behavior is extracted, for example by applying a varying

[1]FE-NVRAM was first implemented in the late 90s in Sony PlayStation 2 and smart cards commercially released in Japan, China, and Brazil

electric field, allowing for direct integration with smart systems. However, the strain and displacement generated by these are typically quite small: ∼0.1% in commercially important piezoelectric ceramics such as those based on the $PbZr_{1-x}Ti_xO_3$ (PZT) solid solution.

To enhance this response, very special compositions are chosen such that the solid solution lies on the morphotropic phase boundary. The morphotropic phase boundary (MPB) delineates the tetragonal and rhombohedral phases, remaining in a near-equilibrium state over a wide range of temperatures below the Curie temperature, T_c. Substantially larger piezoelectric coefficients are achieved in this narrow compositional band of various ferroelectrics. It comes as no surprise, then, that much of the current research in piezoelectrics focuses on finding other morphotropic phase boundaries. For example, Park and Shrout (1997) reported that ultrahigh strains ∼1.7% were achieved near the morphotropic phase boundary of relaxor-type $Pb(Mg_{\frac{1}{3}}Nb_{\frac{2}{3}})O_3$-$PbTiO_3$ (PMN-PT) ferroelectric single crystals.

Such discoveries, based on MPBs, may prove to be technologically relevant for bulk devices, but one must note that this enhanced response is complicated in nature and is likely related to an electric field-induced phase transformation from the rhombohedral to tetragonal state. Furthermore, relying on phase transitions at very special compositions to obtain high strains is not a very forgiving approach, especially as far as miniaturization goes. For smart systems to become increasingly miniaturized on a single platform, we must focus on achieveing high-strains in thin film-based devices, where tight compositional control (as in the MPB case) is not easy to implement

repeatably.

More recently, a different strategy for obtaining large electrostriction in ferroelectrics was suggested by Shu and Bhattacharya (2001). The basic idea capitalized on domain switching giving rise to large strains under certain conditions. For materials like $BaTiO_3$ and $PbTiO_3$, the crystal structure is cubic, and tetragonal [001] polarized, above and below the Curie temperature, T_c, respectively. This is illustrated in Figure 1.1, which features some of the changes associated with the phase transition in $BaTiO_3$ at 120°C. The symmetry breaking below the transition temperature leads to the polarization being aligned with any of the six crystallographically equivalent <100> directions. Ferroelectricity allows for polarization switching between any of these variants via an applied field or mechanical load. The authors suggested a particular electromechanical loading path that relies on a bias stress-state to favor one microstructural variant (domain orientation) combined with an alternating electric field (favoring different polarized variants). This cyclic electromechanical loading results in repeatable switching accompanied by tetragonal re-orientation and, consequently, large strains determined by the c/a lattice parameters of the tetragonal unit cell. That is as high as 1% for $BaTiO_3$ and 6% for $PbTiO_3$. This strategy has been demonstrated experimentally (Burcsu et al., 2000), using $BaTiO_3$ single crystals of (100) orientation. The applied uniaxial compressive stress favored [010] in-plane polarization, while the alternating electric field favored [001] polarization. A threshold applied field caused [010] to [001] switching, and cycling back to zero reverts back to in-plane polarization. Cyclic loading led to repeatable strains up to 1.1%.

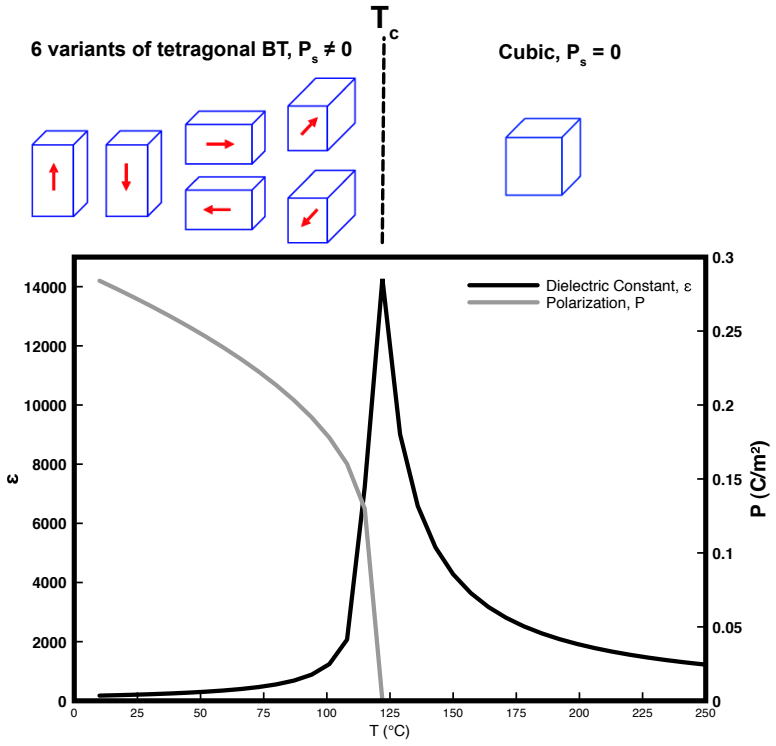

Figure 1.1: The phase transition in $BaTiO_3$. Above $T_c = 120°C$, the material is cubic and the spontaneous polarization, P_s,$= 0$. Upon cooling, the material is ferroelectric, and the crystal structure is tetragonal, with $P_s \neq 0$ along the long axis in any of the 6 possible variants. A tetragonal re-orientation would produce large strains determined by the c/a lattice parameters of the unit cell. The phase transition is accompanied by an anomaly in the dielectric constant, reaching values as high as $\sim 10^4$. P_s and ϵ were computed using the approach outlined in Chapter 5.

One might question how we can extend our recent understanding of ultrahigh electrostriction to materials in thin film form as we turn more and more towards miniaturization and integration. The above approach, for instance, demands that the ferroelectric material be utilized in a highly textured form (as demonstrated in single crystals) to completely cycle between two different polarized states. Furthermore, the electrostrictive behavior may be tuned via compositional control, for example in $Pb_xBa_{1-x}TiO_3$ (PBT), since the c/a ratio and, consequently, the strain varies monotonically with composition.

A large motive for the experimental work presented in this thesis, therefore, is the need for highly-oriented ferroelectric thin films of various compositions. For this purpose, a method is detailed in Chapter 2 to produce highly-textured, composition-controlled, ferroelectric $Pb_xBa_{1-x}TiO_3$ thin films by metalorganic chemical vapor deposition on single crystal MgO and Si_3N_4/Si (using biaxially-textured MgO buffer layers), as well as detailed microstructural characterization.

Progress in the field of ferroelectric research has also been hindered by the problem of polarization fatigue. Briefly, poalrization fatigue is the loss of switchable remnant polarization in a ferroelectric material as the number of bipolar switching cycles increases (Damjanovic, 1998). The expected polarization hysteresis loop in ferroelectrics is a consequence of domain-wall switching. At near-zero fields the polarization increases linearly with the field, as most linear dielectrics do. However, as the field continues to increase, regions of unfavorable polarization begin to align with the field. This is a strongly non-linear regime, and when the majority of domains are aligned with the field, the polarization again increases linearly. Reverting back to zero field does not get rid of the polarization, i.e., a remnant polarization, P_r, remains. The overall polarization can be reverted back to zero by continuing to decrease the field to the coercive field value, E_c. Repeating this cycle forms a hysteresis loop as seen in Figure 1.2. However, bulk and thin film ferroelectrics are susceptible to fatigue, as is illustrated schematically in Figure 1.2.

There have been numerous theoretical and experimental investigations as to the origin of polarization fatigue. Many reports focused on the role of oxygen vacancies by

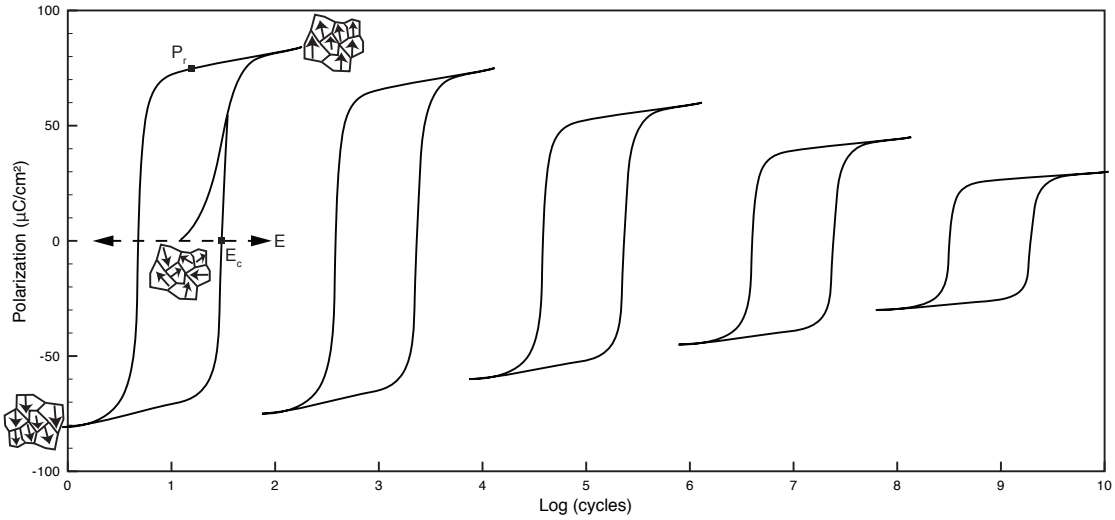

Figure 1.2: Schematic of typically observed polarization fatigue in ferroelectrics. A typical virgin hysteresis loop (left with startup branch) displays big polarization switching where the dipoles align with the electric field in both directions (saturation). However, with repeated cycling, switchable remnant polarization is lost progressively.

observing oxygen vacancy accumulation at the film/electrode interface (Duiker et al., 1990; Scott et al., 1991). These interfacial layers would screen the ferroelectric film and lead to polarization loss. Another mechanism is the possible pinning of domain walls by the accumulating ionic charges in the form of oxygen vacancy defects. The resulting immobile domain walls inhibit domain switching and lead to polarization loss. Other reports focused on domain wall pinning by electron charge trapping (see for example AlShareef et al., 1997). Electronic charge carriers are injected into the films from the electrodes and are attracted to the domain wall regions. If the charges are trapped there, domain walls will be pinned, again reducing the switching and ultimately fatiguing the films.

A very promising development, however, was the discovery that the use of cuprate superconductor electrodes greatly delayed the onset of fatigue (Ramesh et al., 1992),

compared to the traditional elemental metal electrodes. These electrodes are not thermally and chemically very stable, but soon thereafter a variety of conductive metallic oxides led to excellent fatigue behavior in ferroelectric thin film capacitors (for example $SrRuO_3$ electrodes first reported by Eom et al., 1993). Most recently, the coupling between polarization and space-charge distribution was rigorously investigated at Caltech (Xiao et al., 2005), and it was suggested that depletion layers play a critical role in determining charge injection from elemental metallic electrodes (such as Pt) to the ferroelectric. Electrodes with higher work functions are therefore preferred to act as a barrier against charge injection and, ultimately, domain wall pinning. So not only do we need highly-textured ferroelectric thin films as we try to achieve high electrostriction in miniaturized devices, but we must also do so with appropriate electrodes (such as $SrRuO_3$) to tackle the potential fatigue problem.

Another motive for the experimental work presented in this thesis, therefore, is the need to grow highly-oriented oxide thin films that function both as electrodes and texture templates for the active ferroelectric layer. For this purpose I have assembled a pulsed laser deposition (PLD) chamber to produce highly-oriented conductive oxide $SrRuO_3$ thin films on MgO templates. Due to the good lattice match, most results for epitaxy of $SrRuO_3$ are reported on $SrTiO_3$, $LaAlO_3$, or buffered Si substrates (e.g., using yttria stabilized zirconia), but results are rarely reported on MgO (Singh et al., 2002). However, biaxially-textured MgO templates can be deposited directly on Si and amorphous substrates using ion beam-assisted deposition (IBAD) (Brewer et al., 2005) and is therefore an attractive candidate for integrating both ferroelectrics

and $SrRuO_3$ on Si-based substrates. PLD growth of textured $SrRuO_3$ thin films is examined in this thesis, specifically for this reason.

The improved understanding of the electronic properties of ferroelectric thin films and the recent advances in miniaturization have renewed the four-decade-old interest in using ferroelectrics in RF and microwave tunable devices (see for example Didomenico et al., 1962). The desired material properties for microwave applications are primarily high tunability and low dielectric losses, as very well reviewed by Tagantsev et al. (2003). Tunability, n, is the ratio of dielectric permittivity at zero bias to that at some applied electric field, $\frac{\epsilon(0)}{\epsilon(E)}$. In other words, the tunability is the measure of our ability to change the dielectric behavior (capacitance) of a material by applying an electric field. That is an important parameter, for instance in RF and microwave tunable filters, since the change in the resonant frequency depends directly on the change of dielectric permittivity.

Ferroelectrics are highly-tunable materials and can be the basis of a high frequency phase shifter, as pictured in figure 1.3, after DeFlaviis et al. (1997). The idea is quite simple: since some of the microwave field passes through the ferroelectric layer, the phase velocity of the propagating waves can be changed by changing the dielectric permittivity of the ferroelectric layer using an applied bias voltage. The focus has primarily been on using $Ba_xSr_{1-x}TiO_3$ (BST) thin films where the transition temperature and, consequently, the tunability properties can be controlled by changing the composition, x. Recent experimental efforts have focused on using strain (Potrepka et al., 2006) or optimizing the processing conditions and compositional design (Cole

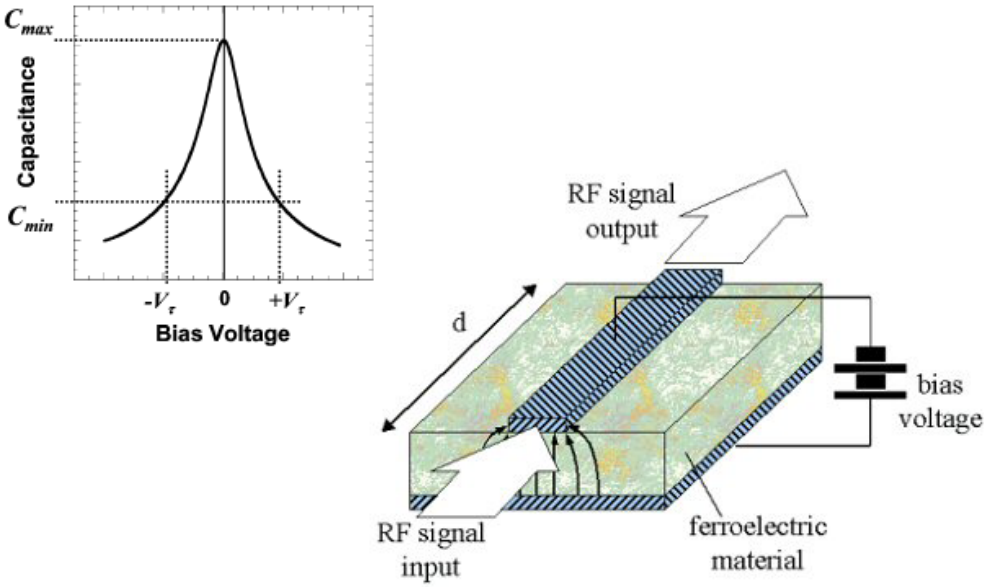

Figure 1.3: BST thin films exhibit excellent tunability characteristics (top left after Chase et al. (2005)) where the capacitance varies greatly with applied bias voltages, especially at temperatures near the phase transition. High tunability enables phase shifter concepts, such as the one pictured here, after DeFlaviis et al. (1997). The phase velocity of the propagating waves can be changed by changing the dielectric permittivity of a ferroelectric strip using an applied bias voltage

.

et al., 2003) to achieve high tunability while lowering dielectric losses. The technology is already promising, as York et al. (Acikel et al. (2002); Serraiocco et al. (2002, 2003); Xu et al. (2005)) have already reported on BST-based tunable circuits and phase shifters with superior tunability characteristics and low losses.

An interesting problem yet remains. Ferroelectrics are indeed highly-tunable, but that is especially true near their phase transition temperatures, where the dielectric constant is quite high. High tunability and high dielectric constants usually go hand in hand (Tagantsev et al., 2003). So, one might engineer the composition of a BST thin film to shift the phase transition to, say, room temperature, but the phase

transition is where the dielectric constant depends very strongly on temperature! Thus, while this method achieves high tunability near room temperature as is desired, the properties are still very temperature-dependent. This means that for conventional ferroelectrics, the resonant frequency of the filter may drift strongly depending on ambient conditions (Zhu et al., 2002a). A separate, but equally, important challenge thus emerges: the need for a low temperature dependence of the dielectric permittivity over the operating temperature range (Tagantsev et al., 2003).

Compositionally-graded $Ba_xSr_{1-x}TiO_3$ thin films have been investigated precisely for this purpose. The idea is that by changing the composition, x, in the growth direction, the heterogeneous structure would result in a diffuse phase transition and a high dielectric constant over a wide range of temperatures, corresponding to different Curie temperatures for the different 'layers.' The diffuse phase transition would redress the temperature sensitivity, while the high dielectric response would reduce the necessary size of the microwave components (Vanderah, 2002), since the length of the electromagnetic waves in the dielectric medium is inversely proportional to the square root of the dielectric constant.

Recent experimental efforts have investigated the growth of graded films and the effect of compositional grading as well as different capacitor geometries on the dielectric response (Slowak et al., 1999; Zhu et al., 2002b; Lu et al., 2003; Zhu et al., 2005), but the results vary somewhat from one research report to the next, primarily for different capacitor geometries. For example, Slowak et al. (1999) achieved more temperature-stable capacitors by using co-planar electrodes on graded BST thin films,

rather than the traditional parallel electrode-plate configuration. The same difference is observed by comparing Lu et al. (2003) and Zhu et al. (2002b).

This motivates Chapter 5 of this thesis, where we address the graded thin film problem using a continuum model that takes into account the spatial variation in properties and the long-range electrostatic interactions. The built-in electric potential, polarization gradient, and electrode charges are computed both in the presence and absence of externally-applied electrical fields, and consequently we deduce the dielectric behavior at various temperatures for different compositional gradings. We seek an understanding of the combinatorial behavior of ferroelectric heterostructures and provide results that are hopefully useful as design tools for the emerging functionally graded devices (FGDs).

This thesis is divided into 6 chapters. Chapter 2 simply introduces some basic background on ferroelectricity and on the synthesis methods chosen to fabricate the ferroelectric thin films (metalorganic chemical vapor deposition, MOCVD) and conductive oxide electrodes (pulsed laser deposition, PLD). In addition, we examine some of the diagnostics implemented during the processing of ferroelectric $Pb_xBa_{1-x}TiO_3$ thin films, namely coherent gradient sensing (CGS) for curvature/stress measurements. The Devonshire-Ginzburg-Landau phenomenological model of ferroelectrics is discussed briefly, and we note how it can be extended to compositional inhomogeneity and electrostatics to tackle the graded film problem in Chapter 5.

Chapter 3 details the MOCVD process used to synthesize $Pb_xBa_{1-x}TiO_3$ thin films and maintain closed-loop control of the film stoichiometry by ultraviolet spec-

troscopic control of the organometallic precursors. The films are characterized in detail for epitaxy both on single crystal MgO and biaxially-textured MgO/Si produced by ion beam-assisted deposition (IBAD). Scanning electron microscopy (SEM) and transmission electron microscopy (TEM) give us insight into the microstructure. X-ray diffraction (XRD) is used to examine the crystallinity and lattice parameter variation with composition, while high-temperature XRD allows us to observe the domain switching process with temperature and consequently allows us to compare with CGS results. Detailed texture is examined by x-ray pole figures and electron backscatter diffraction (EBSD), where we correlate the presence of domain wall boundaries to the grain size using both growth templates. Finally, we summarize our efforts to integrate the ferroelectric films with Si-based devices for electro-mechanical testing, such as bridges, cantilevers and membranes.

Chapter 4 features the PLD process used to deposit conductive $SrRuO_3$ electrodes. It includes details on the custom PLD chamber built for this purpose as well as the experimental conditions needed to produce high-quality electrodes with biaxial texture. Further characterization includes scanning electron microscopy, x-ray diffraction, x-ray pole figures, rocking curves, and reflection high energy electron diffraction (RHEED). This approach led to the direct synthesis of PBT/$SrRuO_3$/IBAD MgO/Si heterostructures, allowing for direct integration of active ferroelectric layers onto Si-based substrates.

Chapter 5 addresses the graded film problem, discussed above, using a continuum Devonshire-Ginzburg-Landau type model that takes into account the heterogeneous

nature of graded thin films and the long range electrostatic interactions. Specifically, we will illustrate how the parallel capacitors approach (graded thin film with co-planar electrodes) results in a diffuse phase transition with low temperature dependence of the dielectric constant by achieving larger polarization gradients and smaller built-in, or depolarizing, fields. That is desirable in order for the dielectric behavior of tunable RF and microwave devices to not drift on hot and cold days.

Chapter 6 concludes this thesis. We reflect on the work presented in the preceding chapters and note the new directions and worthy future work that naturally develops as a result of this thesis.

Chapter 2

Background

2.1 The Phenomenon of Ferroelectricity

Materials belonging to 10 noncentrosymmetric crystallographic point groups[1] possess a unique polar axis, allowing them to exhibit an electric dipole moment in the absence of an external electric field. The polarization associated with the spontaneous dipole is known as the spontaneous polarization, P_s. These materials are called polar, or pyroelectric. Ferroelectrics are polar materials in which the direction of the spontaneous polarization can be switched by an external electric field. All ferroelectrics are necessarily piezoelectric, but the opposite is not true. Piezoelectric materials can be polarized by application of mechanical stress. Therefore, in the direct piezoelectric effect, the charge density, D_i, induced by applying a stress, X_{jk}, is given by:

$$D_i = d_{ijk} X_{jk}. \tag{2.1}$$

Here, d_{ijk} is the tensor of piezoelectric coefficients. In the converse piezoelectric

[1] These point groups are: 1, 2, m, 2mm, 4, 4mm, 3, 3m, 6, and 6mm

effect, a strain, x_{ij}, can develop due to an applied electric field, E_k:

$$x_{ij} = d^t_{ijk} E_k. \tag{2.2}$$

This linear piezoelectric coupling has many applications in sensors and actuators when the mechanical and electrical loading is modest. In ferroelectrics, however, severe loading leads to non-linear responses since uniformly polarized regions (domains) can be switched, leading to irreversible polarization and strain. A major consequence of switching is the occurrence of the ferroelectric hysteresis loop, as pictured schematically in Figure 1.2. In the beginning of the start-up branch in that figure, the polarization increases linearly with the electric field, as any linear dielectric would. As the field gets strong enough, domains switch to align dipoles, entering a non-linear regime. Reverting back to zero field does not get rid of the polarization, i.e., a remnant polarization, P_r, remains. The overall polarization can be reverted back to zero by continuing to decrease the field to the coercive field value, E_c. Repeating this cycle forms a hysteresis loop.

The major properties of ferroelectric thin films stem from their domain microstructure. For this reason, it is beneficial to review the possible domain states and domain boundaries in the ferroelectric state. We specifically review these concepts as they apply to prototypical ferroelectric perovskites such as $PbTiO_3$ and $BaTiO_3$, since many of the interesting ferroelectrics have a perovskite structure. Perovskite crystals have the general formula ABO_3 and can be viewed as BO_6 octahedra surrounded by A cations. These materials transform from a paraelectric cubic state above the

Curie temperature, T_c, to a ferroelectric tetragonal structure as illustrated in Figure 2.1. The spontaneous polarization lies along the c-axis of the tetragonal unit cell and is directly related to the shift of the O and Ti ions relative to the Ba or Pb. Due to the symmetry of the material, there are now six equivalent directions along which the polarization may be aligned. If there were no specific boundary conditions imposed on such a ferroelectric sample, the polarization may arise with equal probability along any of these 6 equivalent directions. Regions of uniform polarization in the crystal are called domains, and in the case of $PbTiO_3$ and $BaTiO_3$, domains may be separated by 90° or 180° domain walls. The intricate domain patterns observed in ferroelectric crystals form to minimize the electrostatic energy and elastic energy associated with the mechanical constraints imposed on the material as it undergoes the cubic-tetragonal phase transition (Damjanovic, 1998).

The most convenient potential function to describe the energy of ferroelectric materials is the elastic Gibbs free energy, G, expressed as a function of temperature, stress, and polarization (Fatuzzo and Merz, 1967). At zero stress, G can be expanded in powers of the polarization, as is done by Devonshire (1949, 1951, 1954). The coefficients are generally functions of temperature. It can be shown that if in the ferroelectric phase the spontaneous polarization lies along a specific direction and the electric field is strictly applied along this direction, then G can be written as

$$G = \frac{\alpha}{2}p^2 + \frac{\gamma}{4}p^4 + \frac{\delta}{6}p^6, \tag{2.3}$$

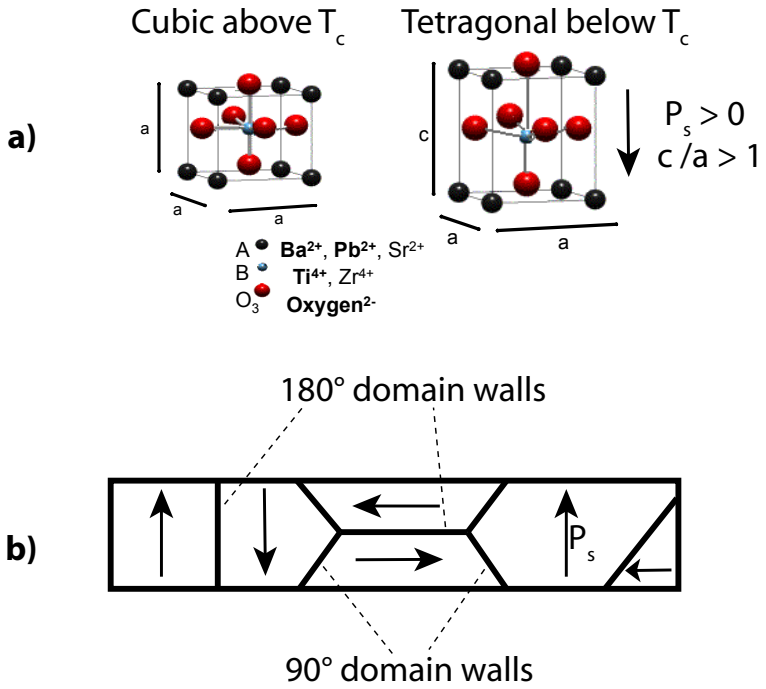

Figure 2.1: Paraelectric-ferroelectric phase transition in perovskites. (a) The spontaneous polarization observed is associated with the distortion of the BO_6 octahedra relative to the A cations, in the tetragonal phase below T_c. (b) The polarization may arise with equal probability along any of these 6 equivalent directions, separated by 90° or 180° domain walls

and the electric field is the result of differentiating G with respect to p

$$E = \frac{\partial G}{\partial p} = \alpha p + \gamma p^3 + \delta p^5, \tag{2.4}$$

where α, δ, and γ are coefficients obtained by fitting the properties of the crystal. For example, α can be related to the dielectric susceptibility, χ, by differentiating equation (2.4) and setting $p = 0$ to obtain $\chi = \frac{p}{E} = \frac{1}{\alpha}$. The dielectric behavior in this setting is governed by the commonly observed Curie-Weiss law, i.e., the dielectric constant falls

with temperature above the Curie temperature, T_c such that $\epsilon = \frac{C}{T-T_0}$ for $T > T_c$, where C is the curie constant, and T_0 is near but not necessarily coincident with T_c. Devonshire's theory therefore assumes that α can be approximated as a linear function of temperature near T_c:

$$\alpha = \frac{4\pi}{C}(T - T_0). \tag{2.5}$$

A simple measurement of the dielectric behavior above T_c, therefore, determines α. The other two coefficients, γ and δ, require knowing the spontaneous polarization and dielectric constant dependence on temperature below T_c, as is detailed in Fatuzzo and Merz (1967). These coefficients are known or calculated for many materials and are summarized in Table 5.1 of Chapter 5 for $BaTiO_3$, $PbTiO_3$, and $SrTiO_3$. Figure 2.2 illustrates the energy landscape for $BaTiO_3$ using the coefficients from Table 5.1 at different temperatures. At room temperature, only the polar ferroelectric phase is stable, and the energy minima correspond to the two opposite values of the experimentally-observed spontaneous polarization in $BaTiO_3$ $\sim$0.25 C/m^2. At a temperature between the Curie-Weiss temperature and Curie temperature ($T_0 = 110°C < T < T_c = 120°C$), a third minimum appears at zero polarization indicating that the non-polar paraelectric phase is metastable, while the ferroelectric phase is still stable. At temperatures above T_c, the paraelectric phase is stable, and the ferroelectric phase can only be induced by applying an electric field. Heating to higher temperatues results in a purely non-polar phase.

The thermodynamic theory outlined above using a free energy such as equation

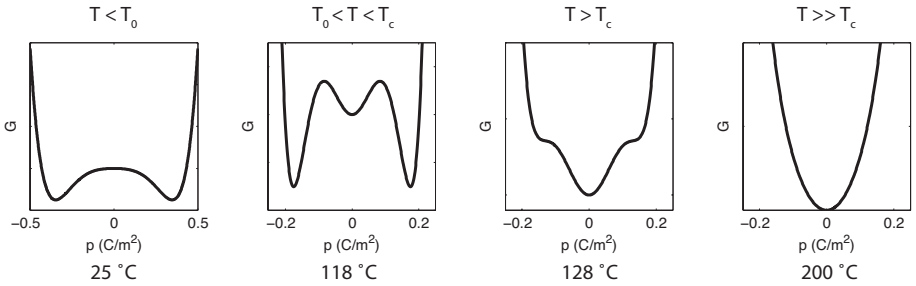

Figure 2.2: An illustration of the energy landscape of $BaTiO_3$ at different temperatures.

(2.3) is commonly referred to as the Devonshire-Ginzburg-Landau (DGL) phenomenological theory. Many of the macroscopic ferroelectric properties, such as polarization and dielectric dependence on temperature, field, and pressure, are well interpreted using this model. This approach, however, does not describe the microscopic mechanisms giving rise to ferroelectricity (Fatuzzo and Merz, 1967), and as outlined above is only valid for a single crystal material in the monodomain state, although there are many efforts to average single-crystal properties over all possible orientations to deduce the polycrystalline behavior (Damjanovic, 1998).

In Chapter 5 we use the DGL formalism to describe the dielectric behavior of compositionally graded ferroelectric thin films by making the expansion coefficients spatially dependent and linearly interpolating between the known coefficients of $BaTiO_3$ and $SrTiO_3$ for intermediate compositions.

2.2 Chemical Vapor Deposition

Chemical vapor deposition (CVD) is a film growth technique where a heated substrate is exposed to volatile precursors that react or decompose on the substrate

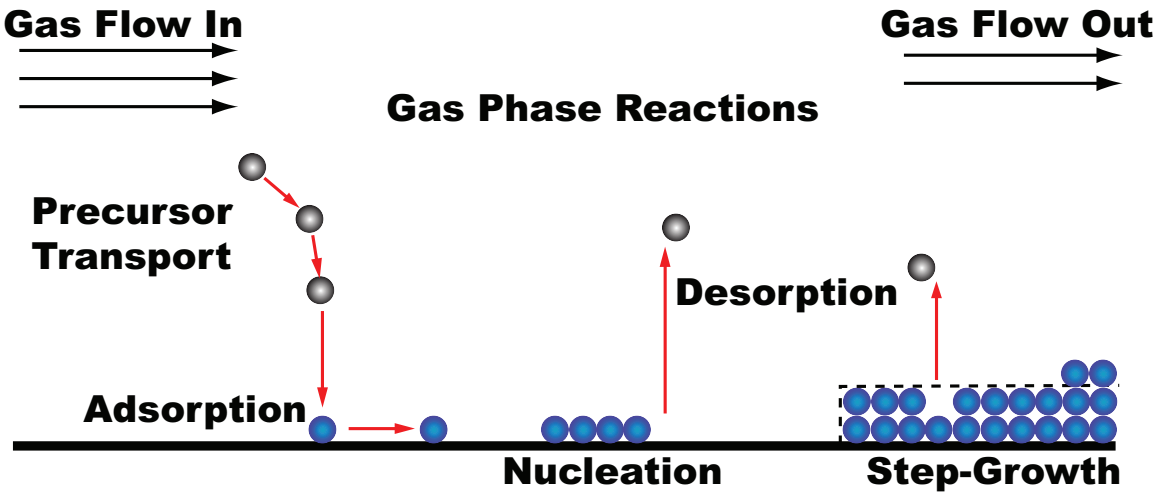

Figure 2.3: A schematic to illustrate the many processes involved in a typical CVD enviornment

surface, resulting in the desired thin film stoichiometry. CVD is a complex process that involves many steps (all research topics in their own rights) such as gas phase reactions, diffusion, surface adsorption, desorption, surface reactions, and crystal growth. Nonetheless, CVD is regarded as one of the most cost-effective means of high-throughput, high-quality thin film deposition of semiconductor and oxide layers in device production. In addition to high growth rates, CVD can provide uniform coverage of non-planar shapes. This is a great practical advantage over many other growth methods since it allows incorporation of new materials, into MEMS or micro-electronic devices for instance, during back-end processing of traditional silicon wafers, complete with interconnects and complex topology.

Part of this thesis details the deposition of $Pb_xBa_{1-x}TiO_3$ thin films by metalorganic chemical vapor deposition (MOCVD), a variant of CVD that uses organometallic compounds as source materials. The MOCVD reactor used in this work is a warm-wall custom-built vertical stagnation flow reactor previously developed at the

California Institute of Technology with National Science Foundation (NSF) and Defense Advanced Research Projects Agency (DARPA) support for the program *Virtual Integrated Processing of YBCO Thin Films*. It is designed for uniformity and features full optical access, both angled and glancing, for various diagnostics. Details on this facility can be found in (Tripathi, 2001).

As will be detailed in Chapter 3, our facility features an advanced precursor gas handling system that allows for closed loop control of gas phase stoichiometry during growth. This approach requires characterizing the ultraviolet absorption spectra of these precursors. The Ba precursor has been previously characterized in this same facility (Tripathi, 2001), while the Pb and Ti precursors are newly characterized in this work, and the results are presented in the next chapter.

Several modifications have been made to the facility, including the gas handling system and data acquisition (DAQ) system to accommodate the newly characterized Ti and Pb precursors. A new sapphire sample holder replaces the original silicon carbide design. This eliminated silicon contamination previously detected in YBCO thin films and also reduced sample (substrate) temperature offset from the heater itself to only about 100 °C (Hammond, 2003). The inconel can (enclosure) surrounding the heater has been redesigned and proved to be an improvement over the old design that was susceptible to mechanical cracking at elevated temperatures. In addition, the entire facility has been relocated from Steele laboratory (California Institute of Technology) to newly renovated space at Thomas laboratory (California Institute of Technology), which provided an opportunity to completely disassemble, clean, and

rebuild the reactor.

In summary, our MOCVD process proceeds as follows. The solid precursors sublimate in the temperature controlled "bubblers" under reduced pressure and then are passed through optical cells, kept at 250 °C, where the UV absorption spectra are collected and used for feedback control of the gas phase relative stoichiometry of Pb, Ba, and Ti. The precursors are then mixed with 2 SLM O_2 and passed through a showerhead onto the heated substrate in vertical stagnation-flow fashion. Figure 3.1 is a highly-simplified schematic of the entire process.

2.3 Coherent Gradient Sensing

The film-on-substrate structure inevitably gives rise to mechanical stress as an issue facing a wide range of thin film applications such as micro-electronics, integrated optical devices, and micro-mechanical devices. The stress can be due to a variety of reasons, including lattice mismatch between film and substrate materials and different coefficients of thermal expansion upon cooling from growth temperatures, to name two of many possible mechanisms. Both these mechanisms for stress accumulation are present in the heterstructures considered in this thesis, namely ferroelectric $Pb_xBa_{1-x}TiO_3$ on MgO. The situation in ferroelectrics is even more interesting than most other materials. This is because $Pb_xBa_{1-x}TiO_3$ undergoes a cubic-to-tetragonal phase transition at T_c (490 °C and 120 °C for $PbTiO_3$ and $BaTiO_3$, respectively) upon cooling from the deposition temperature to room temperature. Once in the tetragonal ferroelectric phase, the film is allowed to form domains, regions of uniform polariza-

tion and crystallographic texture, to minimize the energy of the crystal, including the mechanical energy.

According to most theoretical treatments of this topic, the resultant domain structure in ferroelectric thin films acts to relieve the lattice and thermal mismatch between film and substrate as well as the transformation strain. The approaches taken are mostly variants of the Devonshire-Ginzburg-Landau (DGL) formalism that predict the domain structure in terms of energy-minimizing domain volume fractions (Speck and Pompe, 1994; Koukhar et al., 2001; Alpay and Roytburd, 1998). On the other hand, there has not been an experimental verification of these findings, primarily due to the difficulty of measuring stress *in situ* during thin film deposition and subsequent cooling. The most popular experimental methods include x-ray diffraction techniques (for example, Cullity (1978) and Vreeland et al. (1989)) or laser scanning techniques (Flinn et al., 1987), which are point-wise techniques and therefore maybe difficult to implement on the wafer scale during film growth. There are other full-field techniques based on optical interferometry and shadow moiré imaging, but these are typically vibration sensitive. Moreover, these techniques measure surface topography, requiring double differentiation to obtain curvature, thus introducing significant error into the desired stress value.

A new interferometric technique, coherent gradient sensing (CGS), was developed at Caltech to study dynamic fracture and static stresses in solids and thin films (Rosakis et al., 1998). CGS is a diffraction-based, real-time imaging technique, where a collimated beam is reflected from a sample surface with a wavefront $S(x_1, x_2)$ that

contains information about the sample surface. CGS interferograms measure the slope of the wavefront by beam-shearing, i.e., splitting and displacing a wavefront with itself laterally by a small amount, ω. Shearing is achieved by passing the wavefront through a pair of transmission diffraction gratings, as is illustrated in Figure 2.4. The resulting first order wavefronts with phases $S(x_1, x_2)$ and $S(x_1, x_2+\omega)$ are combined to form an interferogram on the screen. It can be shown (Rosakis et al., 1998) that the condition for constructive interference of the wavefront with its sheared version is

$$\frac{\partial S(x_1, x_2)}{\partial x_\alpha} = \frac{n^{(\alpha)} p}{\Delta}, \quad n^{(\alpha)} = 0, \pm 1, \pm 2, ..., \tag{2.6}$$

where $n^{(\alpha)}$ represents the interferogram fringes observed by shearing along the x_α direction, p is the pitch of the gratings, and Δ is the grating separation. Furthermore Rosakis et al. (1998) show that this result can be related to the sample surface $f(x_1, x_2)$, for small surface deflections, by

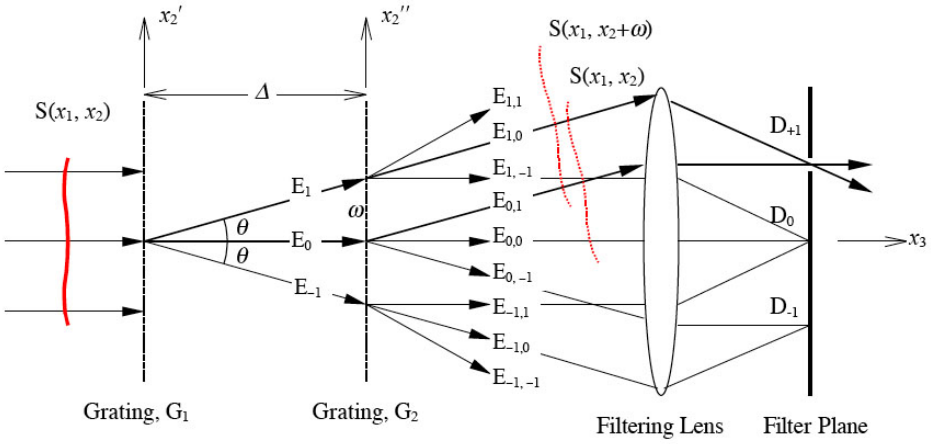

Figure 2.4: The optical bath of coherent gradient sensing after reflection from the sample surface, after Rosakis et al. (1998)

$$\frac{\partial f(x_1,x_2)}{\partial x_\alpha} = \frac{1}{2}\frac{\partial S(x_1,x_2)}{\partial x_\alpha} = \frac{n^{(\alpha)}p}{2\Delta}. \tag{2.7}$$

Using the definition of the surface, any curvature tensor component is given by $\kappa_{\alpha\beta}(x_1,x_2) \approx \frac{\partial^2 f(x_1,x_2)}{\partial x_\alpha \partial x_\beta}$, and we can finally relate the curvature to the spatial derivative of the first order interferogram fringes by the following relation:

$$\begin{aligned} \kappa_{\alpha\beta}(x_1,x_2) &\approx \frac{p}{2\Delta}\frac{\partial n^{(\alpha)}(x_1,x_2)}{\partial x_\beta}, \\ n^\alpha &= \{0,\pm1,\pm2,\ldots\}, \\ \alpha,\beta &\in \{1,2\}. \end{aligned} \tag{2.8}$$

The curvature is therefore directly deduced from the CGS interferograms as the density of fringes and can be related to stress through Stoney's equation. A detailed derivation of the CGS equations can be found elsewhere (Rosakis et al., 1998).

2.4 Pulsed Laser Deposition

From an experimental standpoint, pulsed laser deposition (PLD) is probably the simplest of all thin film growth techniques. Figure 2.5 illustrates a very basic PLD set-up. A high power laser is focused inside a vacuum chamber to strike a target of the desired stoichiometry. Material is vaporized from the target and deposited as a thin film on a substrate facing the target.

While the basic set-up is simple, the physical phenomenon of laser-target interaction is quite complex. When the laser pulse is absorbed by the target, the energy is

first converted to electronic excitation and then into thermal, chemical, and mechanical energy resulting in evaporation, ablation, plasma formation and even exfoliation (Chrisey and Hubler, 2004). The ejected evaporants expand into the surrounding vacuum in the form of a plume containing many energetic species including atoms, molecules, electrons, ions, clusters, particulates, and molten globules.

Pulsed laser deposition offers many advantages besides its simple implementation: fast response, strong film adhesion due to energetic bombardment, and good stoichiometry control through congruent evaporation. There are some draw-backs, including the presence of micron-sized particles in the deposited films and narrow forward angular distribution that restricts the deposition to smaller areas. There are

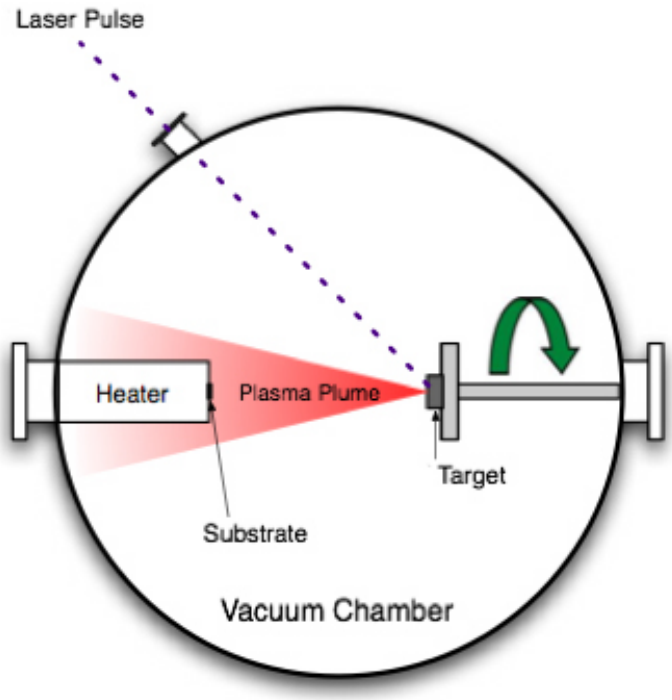

Figure 2.5: Schematic of a basic set-up for pulsed laser deposition.

some work-arounds to these disadvantages. For example, background gas can be used to slow down the particulates, and laser rastering can be done for large area scale-ups. In any case, these draw-backs do not limit the great usefulness of PLD as a rapid research and development tool for new materials.

While Figure 2.5 illustrates a functional deposition set-up, practical PLD chambers often have many extra components. Optical components are used to direct and focus the high-power laser. The deposition may be performed in reactive or inert gas atmosphere, requiring various controlled-flow ports. In addition, the substrate heater is an important element, as epitaxial growth temperatures often reach 1200 °C, and temperature uniformity is necessary to produce thin films of uniform thickness. These and other considerations will be detailed in Chapter 4, which describes the newly assembled general-purpose PLD system, mainly used in this study for epitaxy of $SrRuO_3$ electrodes.

Chapter 3

Metalorganic Chemical Vapor Deposition Of $Pb_xBa_{1-x}TiO_3$

3.1 Introduction

High frequency response and work output per unit volume are two important figures of merit for micro-actuator materials (Krulevitch et al., 1996). Taking this into account, ferroelectrics are candidate materials since actuation can be achieved by directly applying electric fields. As a ferroelectric, the solid solution system $Pb_xBa_{1-x}TiO_3$ (PBT) is [001] polarized at room temperature (tetragonal) and is cubic above the Curie temperature, T_c. The polarization direction may lie along any of the six equivalent $< 100 >$ directions, and this direction of polarization can be switched by applied electric fields or mechanical loads. The switching is accompanied by a reorientation of the tetragonal unit cell and can lead to a strain corresponding to $c/a - 1$, where c/a is the ratio of lattice parameters. In principle, this strain is about 1% for $BaTiO_3$ (BT) and 6.3% for $PbTiO_3$ (PT) (Shirane et al., 1950a). Furthermore, the mobility of 90° domain walls is expected to be a function of composition since the Curie temperature varies monotonically with composition, from 120 °C for BT to 490 °C for PT. The

ability to tune the composition of the ferroelectric thin film, and consequently the strain and response time, may allow flexibility in material design.

To achieve the high strains associated with the c/a ratio, PBT must be utilized in single crystal or highly textured thin film form in order to be completely cycled between two different polarized states (Bhattacharya et al., 1999; Bhattacharya and James, 1999). MOCVD has been shown to be an excellent technique for depositing PT on various substrates (Chen et al., 1995; Kim and Yom, 1999; Sun et al., 1997, 1996; Yoon et al., 1996; Yu et al., 1995), including on MgO (Gao et al., 1993; Okada et al., 1989; Dekeijser et al., 1995). BT has also been successfully deposited on MgO using MOCVD (Nakazawa et al., 1991; Zhang et al., 1994). Despite this, little work has been done on MOCVD of the PBT system. Results available in the literature for MOCVD PBT on Pt/Si (Schafer et al., 2000) indicated ferroelectric behavior only for $x > 0.8$ and strongly distorted c/a ratios (< 1 for $x < 0.8$), where the distortions were attributed to film stress.

In this chapter we report the successful deposition of highly-oriented ferroelectric PBT ($0.2 \leq x \leq 1$) thin films on both commercially-obtained single crystal MgO (used as received) substrates as well as amorphous Si_3N_4/Si using 20 nm IBAD (ion beam-assisted deposition) MgO followed by 20 nm homoepitaxial MgO as a templating layer. Details on the IBAD MgO process can be found in (Brewer et al., 2005). MgO is used as a substrate because the lattice parameter (4.213 Å) is reasonably well-matched to the lattice parameters of tetragonal BT ($c = 4.038$ Å, $a = 3.994$ Å) and PT ($c = 4.151$ Å, $a = 3.905$ Å). Furthermore, it has been demonstrated (Brewer et al., 2005; Wang

Pb precursor temperature	135 °C
Ba precursor temperature	236 °C
Ti precursor temperature	130 °C
Total carrier gas flow rate	3 SLM
O_2 flow rate	2 SLM
Reactor Pressure	15 Torr
Substrate Temperature	650 °C

Table 3.1: Typical growth conditions for MOCVD of PBT films on MgO.

et al., 1997) that IBAD MgO on amorphous Si_3N_4 develops narrow biaxial texture and is therefore suitable as a buffer layer to integrate PBT with Si-based substrates.

A detailed characterization of the microstructure is presented using a variety of techniques for PBT on both types of substrates, including microstructural changes (domain switching) with temperature and the associated changes in mechanical stress. There is evidence that the ferroelectric and fatigue properties of thin films depend on crystallite orientation (Chateigner et al., 1998; Kim et al., 1994; Mansour and Vest, 1992). Detailed texture analysis is, consequently, a crucial method in the characterization of ferroelectric-based electronic and MEMS devices. We use electron backscatter diffraction (EBSD) to confirm the presence of 90° domain walls and to study the crystallographic texture in PBT thin films in addition to x-ray pole figures.

3.2 Experimental

3.2.1 Deposition

The MOCVD reactor used in this study is a custom-built, warm-wall stagnation flow reactor with a vertical showerhead (Tripathi, 2001) and modified as discussed in Chap-

ter 2. The barium, lead, and titanium precursors used are $Ba(tmhd)_2$, $Pb(tmhd)_2$, and $Ti(OPri)_2(tmhd)_2$, where OPri is di-isopropoxy and tmhd is 2,2,6,6-tetramethyl-3,5-heptanedione or $[(CH_3)_3CC(O)CHC(O)C(CH_3)_3]$, a popular organic ligand used with large metal ions to make volatile CVD precursor compounds. All three precursors are commercially available.[1] These entirely organic ligands can be fully oxidized in the CVD chamber during growth, resulting only in carbon dioxide and water vapor (Dahmen and Gerfin, 1993). The reactor features a precursor delivery system that allows for closed loop control of gas phase stoichiometry during deposition to produce PBT films of varying compositions. The precursors are kept in bubblers inside separate ovens to sublimate at their specific temperatures. Table 3.1 lists typical experimental settings for the precursors and growth conditions. Figure 3.1 is a simplified schematic of the process, while Figure 3.2 is an annotated picture of the facility.

The stoichiometry control is accomplished using an ultraviolet-based control loop, where the UV signals are used to determine the gas-phase composition during growth. UV-based precursor control has been demonstrated in the literature for YBCO superconducting thin films (Tripathi, 2001; Desisto and Rappoli, 1998). These precursors typically have distinct absorption features in the ultraviolet spectrum. For example, the Ba precursor has an absorption feature at 290 nm, as previously characterized in this facility (Tripathi, 2001) for YBCO deposition. The Pb and Ti precursors were more recently characterized as part of this study to deposit PBT films, and the results are presented in Figure 3.3.

[1] Inorgtech, Ltd. Suffolk, United Kingdom, recently acquired by the Epichem Group

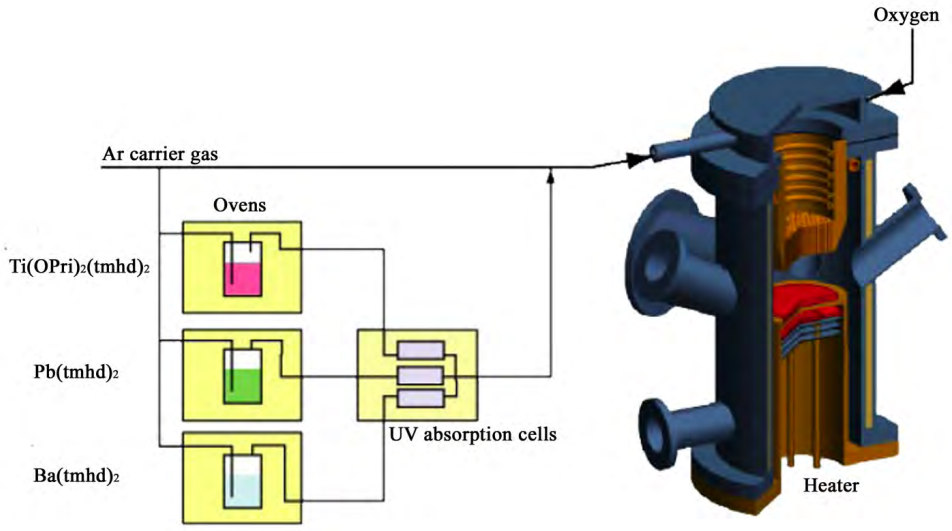

Figure 3.1: Schematic for MOCVD deposition process of $Pb_xBa_{1-x}TiO_3$ thin films featuring an ultraviolet-based control system for gas phase stoichiometry

The control wavelengths chosen correspond to the absorption features in the spectra and are 290 nm, 300 nm, and 330 nm for the Ba, Pb, and Ti precursors, respectively. The solid precursors sublimate in the temperature controlled bubblers under the reduced pressure and are then passed through separate optical cells kept at 250 °C. At each cell, the UV signal strength indicates the concentration of the specific precursor. Active control in the feedback loop is accomplished by changing the carrier gas flow rate (3 SLM argon total) through the individual bubblers. The total precursor flow rate is typically kept at 75 μmoles/minute. The precursors are then combined and subsequently mixed with 2 SLM O_2 and passed through a showerhead onto the heated substrate in the vertical stagnation-flow reactor. A typical growth rate resulting from this procedure is 3-4 nm/min of PBT.

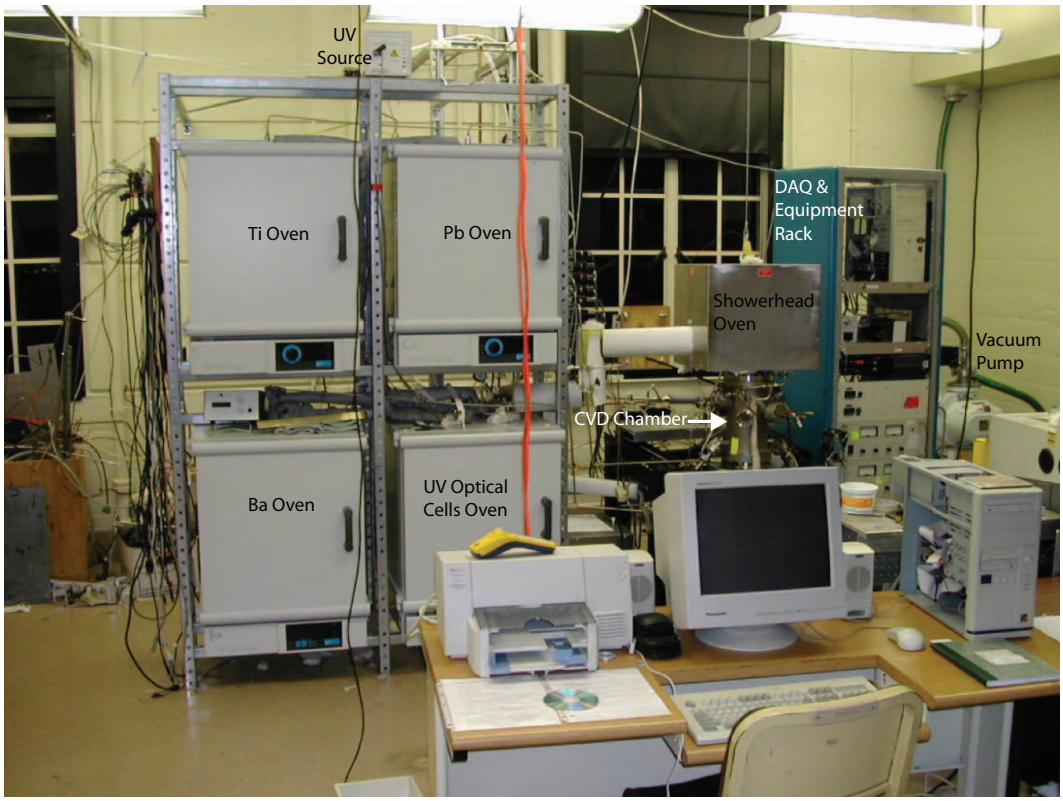

Figure 3.2: Photograph of the CVD facility in 108B Thomas aboratory (California Institute of Technology).

3.2.2 Diagnostics and Characterization

Our CVD reactor is equipped with an *in situ* coherent gradient sensing (CGS) interferometer as shown in Figure 3.4 (Boyd et al., 2005). The incident laser beam, which is filtered and collimated, is directed by a mirror to the sample. Upon reflection from the sample, the beam is directed through a pair of transmission gratings, and the first diffraction order is passed to the frame grabber.

The CGS technique is discussed in Chapter 2. In our CGS interferometer, an 18 mWatt HeNe laser (632 nm) was collimated to a 50 mm diameter beam, and the angle of incidence, relative to the sample normal, was 60°. The pitch of the diffraction gratings was 3.37 lines/mm, and the grating spacing was 81.25 mm. The gratings

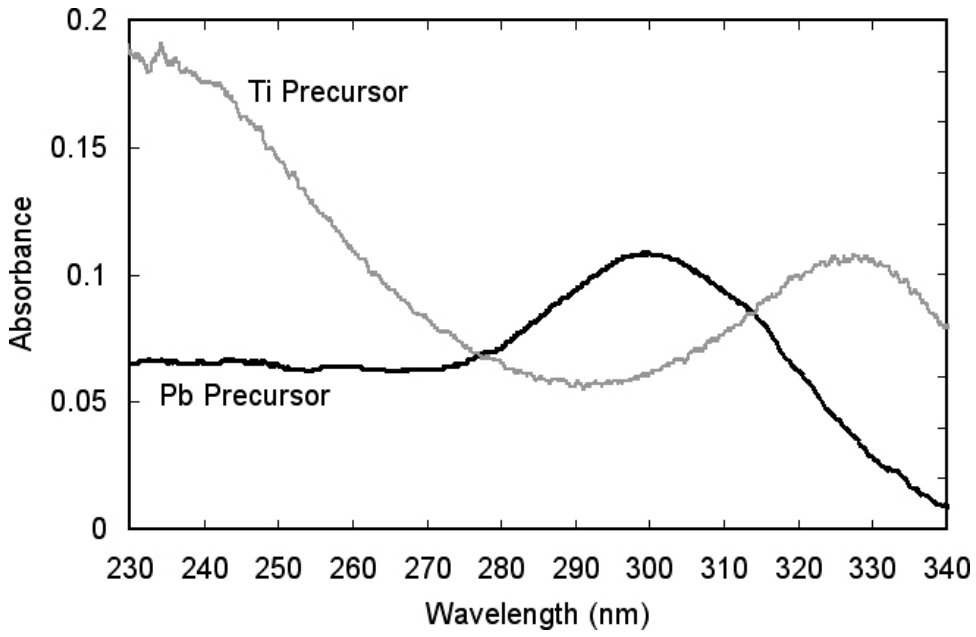

Figure 3.3: Ultraviolet spectra of Pb and Ti precursors. The absorption features at 300 nm and 330 nm chosen for control purposes of Pb and Ti precursors, respectively

were housed in a closed box to reduce the effects of air currents. The interferometer was referenced to an optically flat mirror, and in these experiments fringes were added to the reference by slightly de-focusing the incident beam. Only a single direction of shearing was measured. Curvature can be measured directly from the first order CGS interferograms as the fringe density using Equation (2.8). We use CGS to measure the curvature during processing of a $PbTiO_3$ film prepared by CVD. For films that are thin compared to the substrate thickness, the film stress, σ_f, can be related to the measured curvature, κ, directly using Stoney's equation (Stoney, 1909):

$$\sigma_f = \frac{1}{6}\frac{E_s}{(1-\upsilon_s)}\frac{h_s^2}{h_f}\kappa \ . \tag{3.1}$$

The variables h_f and h_s are the film and substrate thicknesses, respectively. E_S is

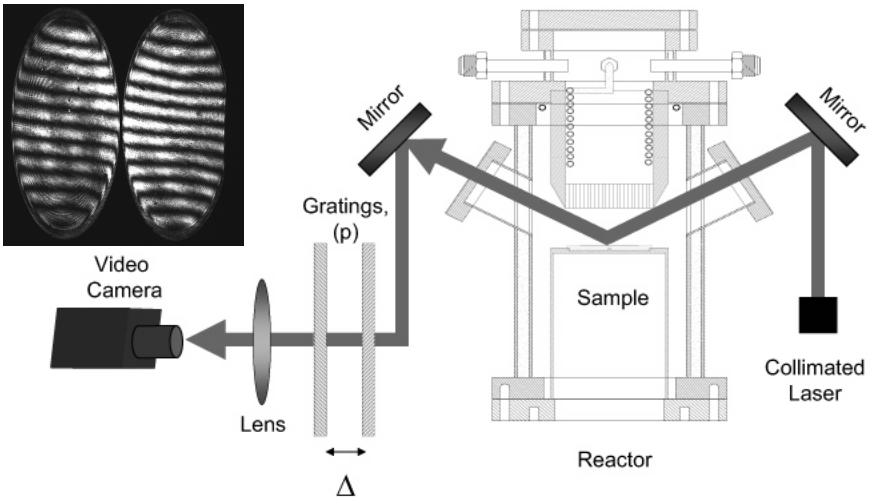

Figure 3.4: A schematic of the CGS optical arrangement around the MOCVD reactor. The density of interference fringes can be analyzed to deduce curvature from CGS interferograms.

the Young's modulus of the substrate, and υ_s is the Poisson's ratio of the substrate.

Phase modulation was implemented in these experiments to increase the sensitivity of CGS as well as determine the sign of the curvature (Boyd et al., 2006). This technique involves moving one of the gratings in the direction of shearing by small steps and measuring the corresponding fringe displacements. The fringes are stepped in four increments of 90°, and the magnitude and the direction of the fringe displacements of interferograms are measured and converted to a phase map. Using a method known as phase-unwrapping, the phase map is transformed to a map of the optical path difference (OPD), which for this type of interferometer represents the wavefront slope (Malacara et al., 1998). Zernike polynomials, which are commonly used to de-

scribe wavefront abberations, are fit to the OPD. For this sample, which had uniform curvature, the first order Zernike polynomial sufficed to determine the average fringe density. For our experiment, the sets of four interferograms were captured and stored continuously during growth and with a 15 second delay between sets during cooling and thermal cycling. The collection time for each set was approximately 15 seconds, and the phase-unwrapping, which is computationally intensive, took place after the CVD processing.

In addition to *in situ* stress monitoring through CGS, the PBT thin films were examined using a wide assortment of analytical tools. The microstructure, surface morphology, and chemical composition of the PBT thin films were studied using a scanning electron microscope (LEO 1550 VP Field Emission SEM) equipped with an energy dispersive spectrometer (EDS). Quantitative analyses of stoichiometry were performed using an electron microprobe analyzer (Jeol JXA-733 EMPA) with sampling volumes of a few cubic microns, corresponding to a weight of a few picograms.

The crystallinity and phase purity were examined using $\theta - 2\theta$ XRD scans (Philips X'Pert PRO MPD diffractometer) indicating the orientation of the deposited thin films, while scans conducted at higher temperatures were used to investigate domain switching and produced quantitative information regarding the abundance of specific domains in the films. Scans were typically collected from $2\theta = 10^\circ$ to $2\theta = 80^\circ$.

Detailed domain characterization was accomplished by pole figure techniques (Philips X'Pert equipped with a texture cradle), and the results were compared to electron backscatter diffraction (EBSD) data. In recent years, EBSD has emerged

as a powerful characterization tool for probing the microtexture of materials. The combination of high surface sensitivity, high spatial resolution ($\sim$ 50 nm in a field emission SEM), and large spatial extent (using computer controlled stages) cannot be matched using traditional texture techniques (Schwartz et al., 2000).

In this study we applied EBSD to study the texture of the ferroelectric thin films. Only samples with high Pb content ($x \geq 0.8$) were analyzed using this technique, since the increased tetragonal distortion makes it easier to distinguish between c and a domains during the automated indexing. The domain fractions and tetragonal tilt angles measured by EBSD, specifically on Pb-rich films with $c/a \geq 1.05$, produced results consistent with x-ray pole figure analysis. The tilt angle between c and a domains, δ, accompanying the tetragonal distortion is especially useful for detecting domain boundaries. For $c/a \geq 1.05, \delta \geq 2.8°$, while the minimum measurable dispersion in orientation, using EBSD, is 1° (Schwartz et al., 2000). Square regions of a few microns on each side were typically analyzed using grid points 50 nm apart for a total of a few thousand patterns from each sample.

3.3 Results and Discussion

3.3.1 Orientation

Only ($h00$) and ($00l$) PBT peaks were observed in $\theta - 2\theta$ XRD spectra, indicating that the c and a axes of the tetragonal phase are either in or out of the plane of the substrate exclusively. Figure 3.5 compares the $\theta - 2\theta$ spectra of two PBT films

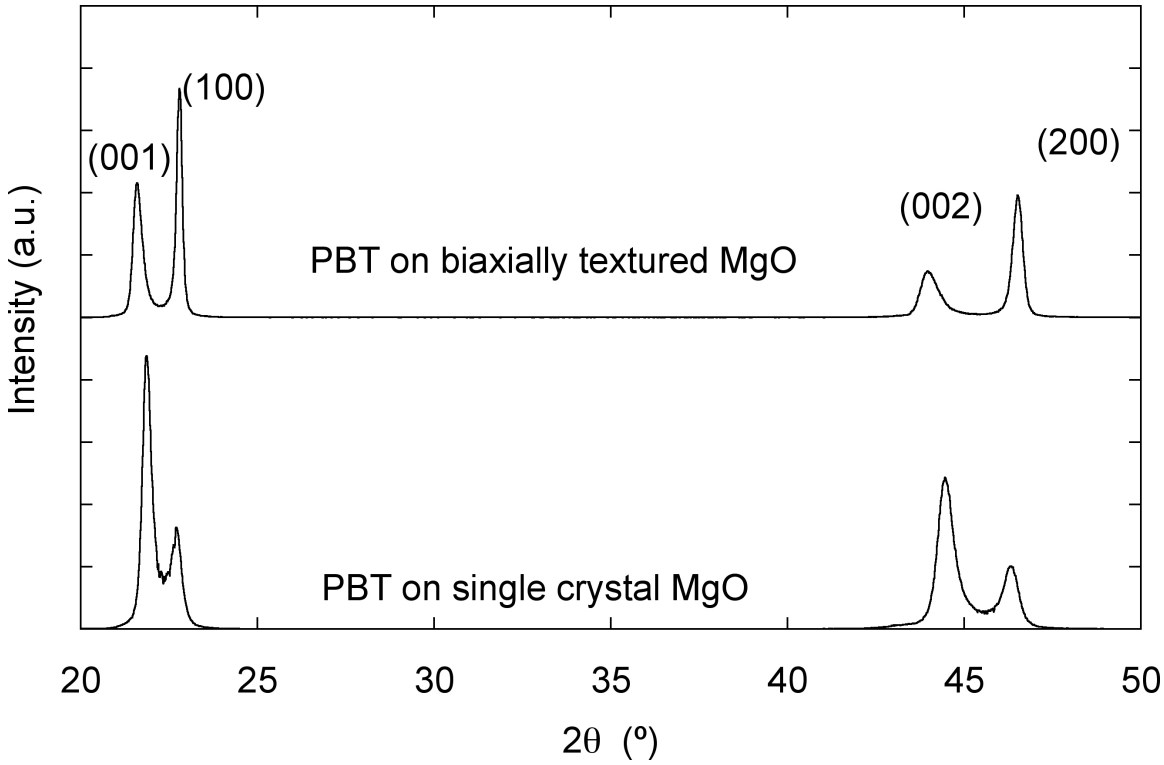

Figure 3.5: XRD comparison of PBT on single crystal and biaxially textured MgO buffer layers on Si.

(x = 0.8, 0.5 μm thick). The film grown on single crystal MgO is predominantly c-axis (out-of-plane) oriented, while PBT on the biaxially textured MgO/Si_3N_4/Si substrate is mostly a-axis oriented. The difference is attributed to the low thermal expansion coefficient of the Si substrate compared to MgO single crystal substrates ($\alpha_{Si} = 2.6 \times 10^{-6}$/K (Hull, 1999), $\alpha_{MgO} = 14.8 \times 10^{-6}$/K (Touloukian et al., 1977), while $\alpha_{PT} = 12.6 \times 10^{-6}$/K and $\alpha_{BT} = 9.8 \times 10^{-6}$/K (Jaffe et al., 1971)). At the high growth temperature, PBT is cubic. As the film cools below the Curie temperature, PBT transforms to the ferroelectric tetragonal phase and experiences compressive stress on single crystal MgO (promoting c-axis orientation), while PBT on biaxially textured MgO/Si_3N_4/Si experiences tensile stress (promoting a-axis formation).

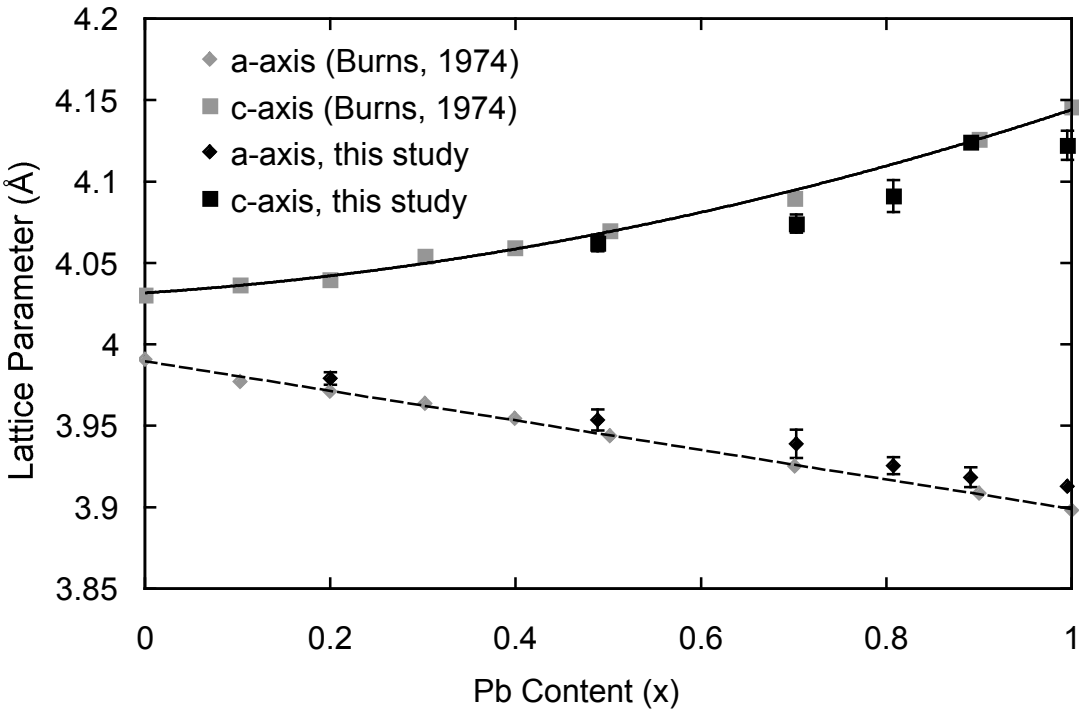

Figure 3.6: Variation of PBT thin film lattice parameters with composition.

The PBT films of various compositions were deposited on MgO, and the variation of lattice parameters, determined from normal $\theta - 2\theta$ scans, with Pb content (x) is consistent with the published results (Burns, 1974) on bulk powder as shown in Figure 3.6. The Pb content was measured using electron microprobe analysis (EMPA). For thin films, the tetragonality ratio, c/a, was found to be slightly less than what is expected for the stress-free PBT powder.

3.3.2 Imaging

Cross-sectional SEM (Figure 3.7) revealed crack-free cross-sections with uniform thicknesses as well as clean interfaces. Surface images (Figure 3.8) showed features, 200-400

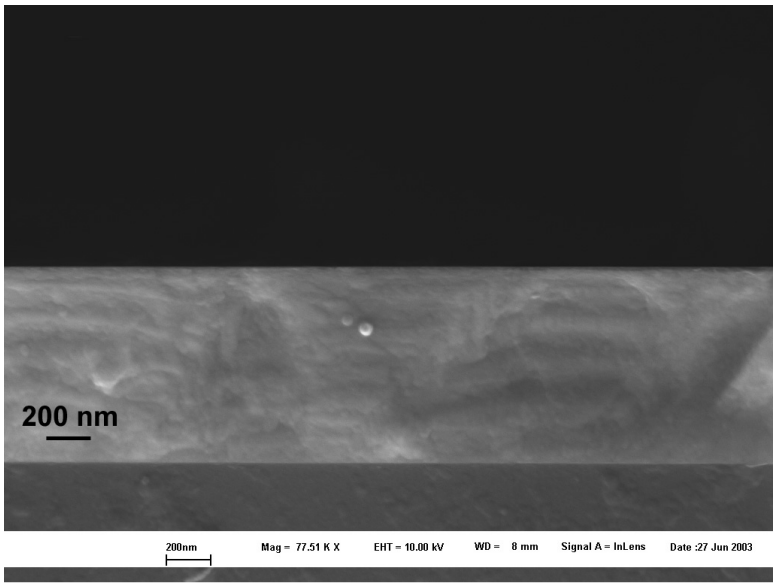

Figure 3.7: Cross sectional SEM image of PBT film on single crystal MgO.

nm in size, for PBT films on single crystal MgO, while films deposited on biaxially textured MgO templates had smaller grain sizes of 40-90 nm. No impurities were detected using EDS. The small PBT grain size on the biaxially textured templates is most likely due to the reduced size of the MgO grains, which is characteristic of the IBAD process.

3.3.3 Domain Characterization

The tetragonal distortion in PBT ($c/a \neq 1$) causes a tilt angle, δ, between the (100) plane of the a domains and the (001) plane of the c domains, as illustrated in Figure 3.9. As a result, it is not possible to get a complete picture of domain orientation in PBT using normal x-ray $\theta - 2\theta$ scans alone. X-ray pole figures are necessary for a comprehensive understanding of the domain orientation (De Veirman et al., 1994).

For the PBT thin films examined in this study, the c domains were observed to be

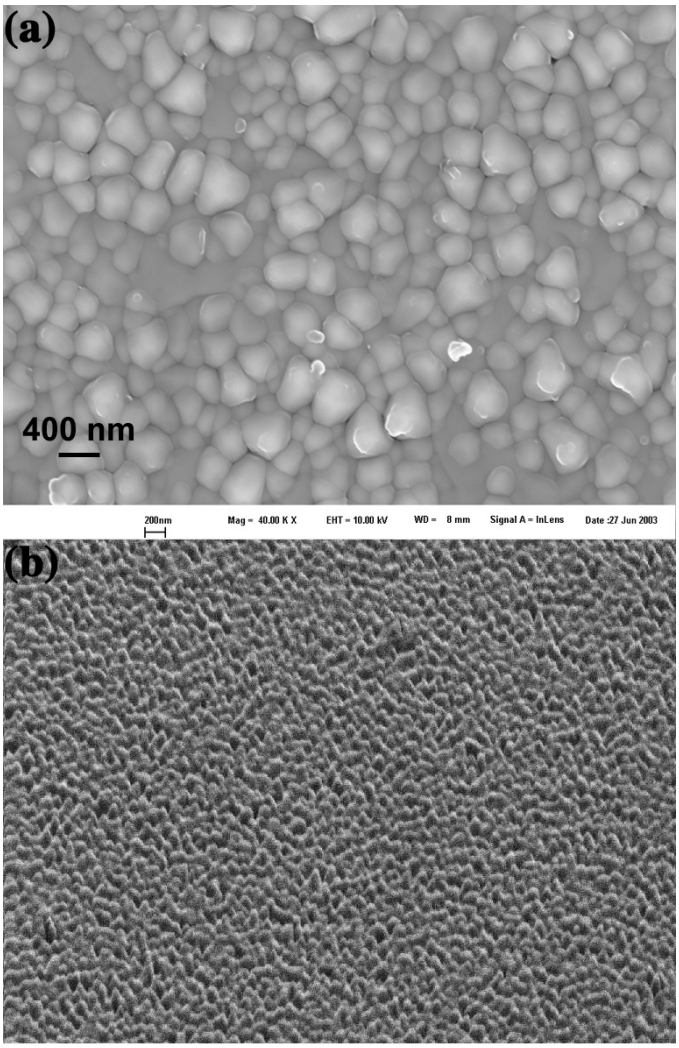

Figure 3.8: Surface secondary electron images from PBT films ($x = 0.95$) on (a) single crystal MgO and (b) biaxially textured MgO templates/Si_3N_4/Si.

oriented normal to the sample's surface, while the a domains were tilted by the angle δ in four equivalent directions away from the substrate normal, giving rise to four variants. A sample (100) pole figure (Figure 3.10) for PT on single crystal MgO, is four-fold split, indicating the presence of these four variants. The four-fold splitting, observed here for various compositions of PBT on single crystal MgO, is the direct signature of 90° domain walls in the films.

In principle, the tilt of the a domains would lead to $\theta - 2\theta$ normal scans underes-

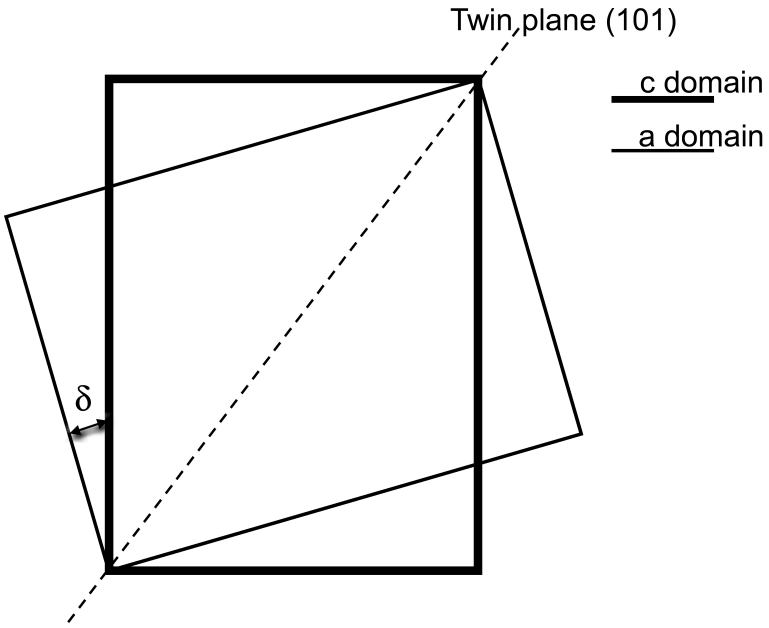

Figure 3.9: Misorientation angle of c and a domains separated by (101) twin plane (exaggerated). The misorientation can lie in any of 4 directions (1 shown) due to the unit cell symmetry.

timating the abundance of a domains when calculating the domain fractions from the integrated intensities of diffraction peaks (Hsu and Raj, 1995). In this study, domain volume fractions for a variety of PBT compositions and film thicknesses were calculated using $\theta - 2\theta$ scans (using integrated intensities from the first order diffraction peaks) and pole figures (using full volume integration of (001) and (100) poles) at room temperature. The normal scans were found to underestimate the a domain volume fraction, but only slightly. For instance, direct comparison of domain fractions from pole figure volume integration and $\theta - 2\theta$ scans, at room temperature, differed only by 3% for a 400 nm, $x = 0.8$ PBT film and only 5% for a 250 nm PT film (composition $x = 1$, where the tilt angle is maximum). As the temperature increases, the tetragonality ratio, c/a (confirmed experimentally using the $\theta - 2\theta$ scans), as well

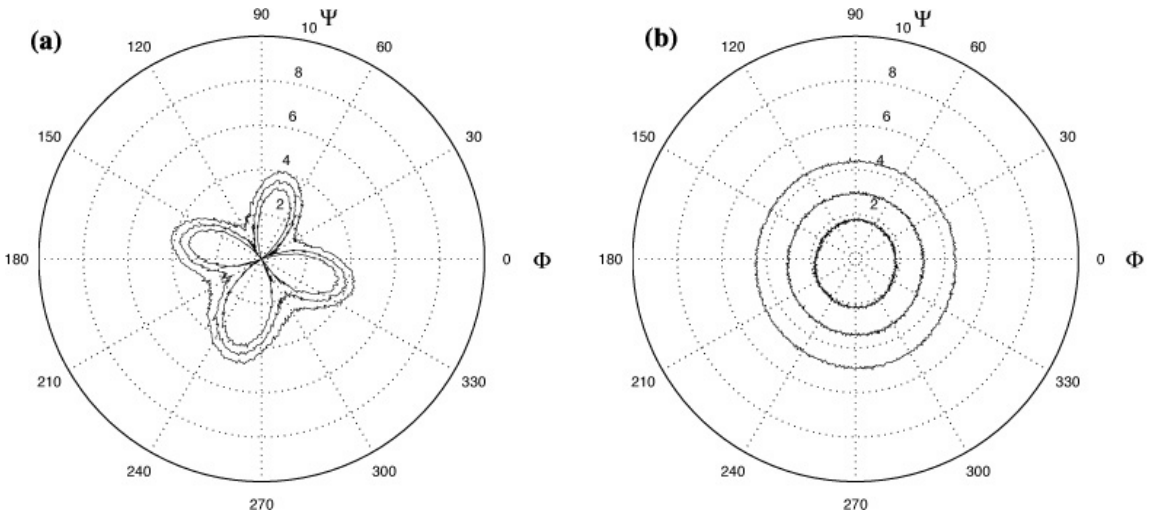

Figure 3.10: Simplified (100) pole figures of PT thin films. Four-fold splitting is observed for PT on single crystal MgO (a), indicating the presence of 90° domain walls. No twin boundaires observed for PT on IBAD MgO/Si_3N_4/Si (b).

as the tilt angle, δ, decrease. This further improved the domain fraction results from the $\theta - 2\theta$ scans. For this reason, $\theta - 2\theta$ scans will be used below to estimate the extent of domain switching at higher temperatures.

Pole figures, both (001) and (100), were also collected for films deposited on biaxially textured IBAD MgO substrates. These data exhibited no such pole splitting, suggesting the absence of twin boundaries (Figure 3.10). The presence of 90° domain walls only for films grown on single crystal MgO is consistent with results obtained using cross-sectional transmission electron microscopy (XTEM) on similarly prepared films (Brewer, 2004). In XTEM images (Figure 3.11) of a PBT film on single crystal MgO, a regularly spaced domain structure is observed, where a domains appear as wedges oriented at about 45° the normal in the predominantly c-axis film. No such structure was observed for a PBT film on the biaxially textured MgO/Si_3N_4/Si template grown in the same batch, under the same processing conditions (Brewer

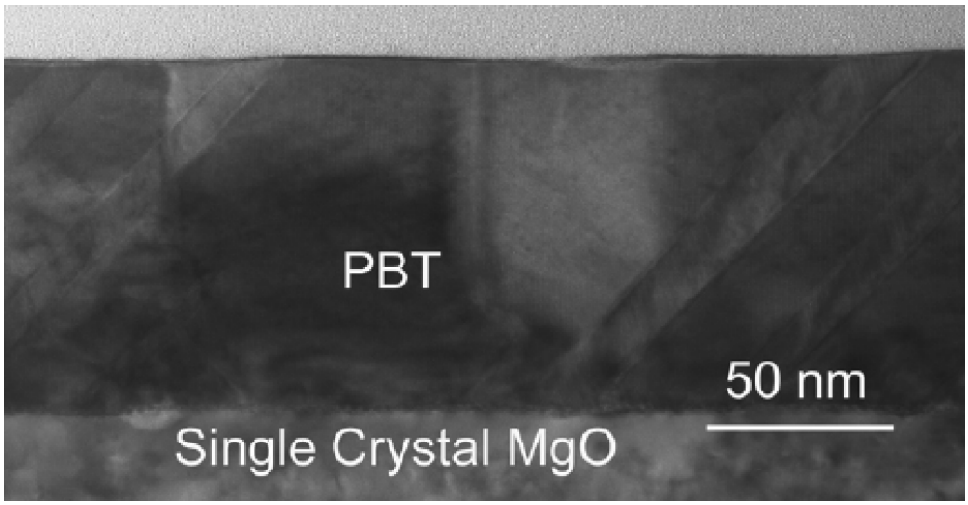

Figure 3.11: XTEM image of the domain structure observed for MODCV PBT film on single crystal MgO consistent with pole figures (from Brewer (2004)).

et al., 2005).

Plan view TEM indicated that the grain size for PBT on biaxially textured MgO (60 nm average) was indeed smaller than that for PBT on single crystal MgO. We propose that this reduced grain size is the primary reason for absence of the 90° domain walls. It has been observed that a domain-structure transition, from multi-domain to single-domain grains, occurs for small grain sizes (∼150 nm) (Ren et al., 1996), resulting in whole *c* or *a* oriented grains. This is consistent with the absence of domain boundaries (from pole figures and XTEM) for the films on biaxially textured substrates, where the grain size is well below this limit.

3.3.4 Microtexture

Inverse pole figures (IPFs) were calculated from EBSD data, as a convenient texture representation for the thin film geometry, where single axis textures can be displayed (normal to or in-plane of substrate for instance). IPFs were consistent with XRD

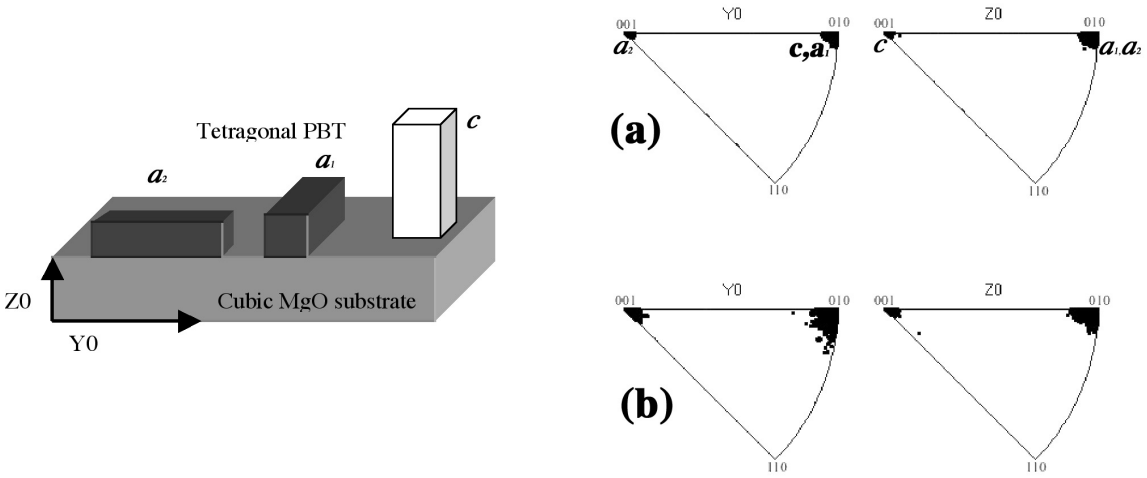

Figure 3.12: Inverse Pole Figures for 500 nm PBT thin films ($x = 0.9$) on (a) single crystal MgO and (b) biaxially textured IBAD MgO. The Y0 and Z0 axis are aligned with the MgO $< 001 >$, as illustrated above. c and a domains are illustrated and labeled on the appropriate IPF.

results, indicating that the vast majority of sample patterns are either (001) or (100) oriented for PBT on both types of substrates (Figure 3.12 for 500 nm PBT films, $x = 0.9$). Furthermore, the in-plane (Y0-IPF along MgO 001 in the plane of substrate) and out-of-plane (Z0-IPF along surface normal) textures had a smaller mosaic spread for samples on single crystal MgO compared to biaxially textured MgO templates, as is expected.

The c vs. a domain fractions can also be estimated using EBSD from the normal axis IPF by simply counting the number of data points that cluster around the 001 and 010 poles. It must be noted, however, that the penetration depth of EBSD is only 30-60 nm, compared to a few microns using XRD. The domain fractions obtained from EBSD, therefore, will represent the near-surface domain structure except for very thin films. Domain fractions obtained using EBSD were within 5-10% of XRD data for PBT films less than 100 nm in thickness. For thicker films ($\sim$ 500 nm) we

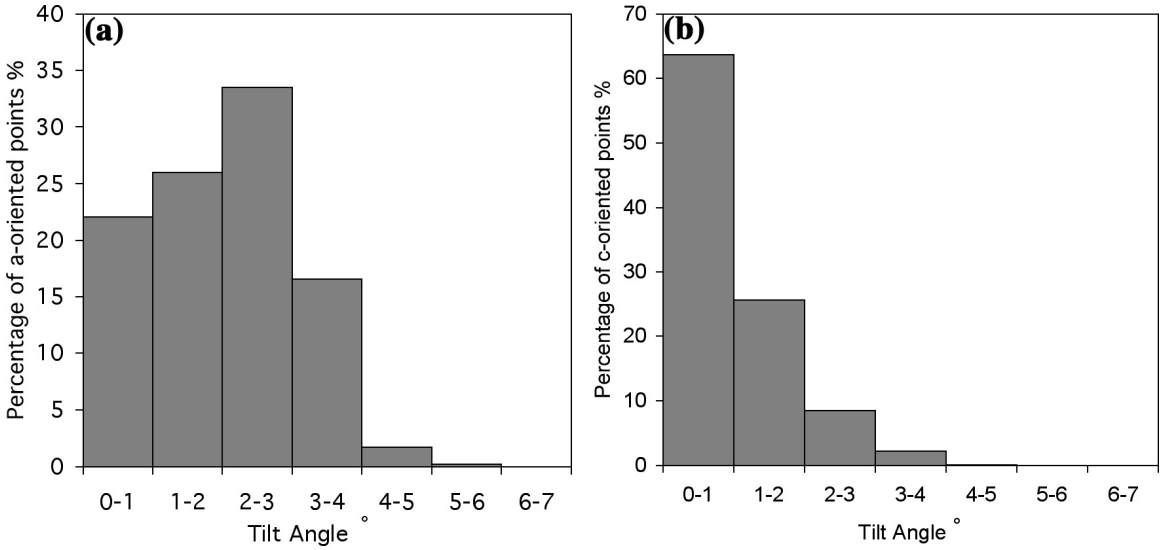

Figure 3.13: EBSD confirms the tilt of a domains away from surface normal by the angle δ (a), while c domains exhibit a standard distribution (b). Results for 500 nm PBT film ($x = 0.9$) on single crystal MgO. The tilt is consistent with x-ray pole figures and is the direct signature of ferroelectric 90° domain boundaries.

observed differences as large as 30%, where the EBSD data typically overestimated the abundance of the minority domain orientation.

The EBSD data were also consistent with the observation of the tetragonal tilt angle, where a domains (for PBT on single crystal MgO) were tilted from the surface normal by δ (see Figure 3.9). The orientation data, gathered from the a-oriented sample points, showed the majority of a domains were tilted 2° to 3° away from the surface normal (Figure 3.13), compared to a standard distribution for the c domains. This spike agrees well with the expected tilt angle value for this film, where $c/a = 1.051$, and $\delta = 2\arctan(\mathrm{c/a}) - 90° = 2.85°$. No such spikes were found for PBT films on biaxially textured MgO, further confirming the absence of 90° domain boundaries in these films due to the reduced grain size.

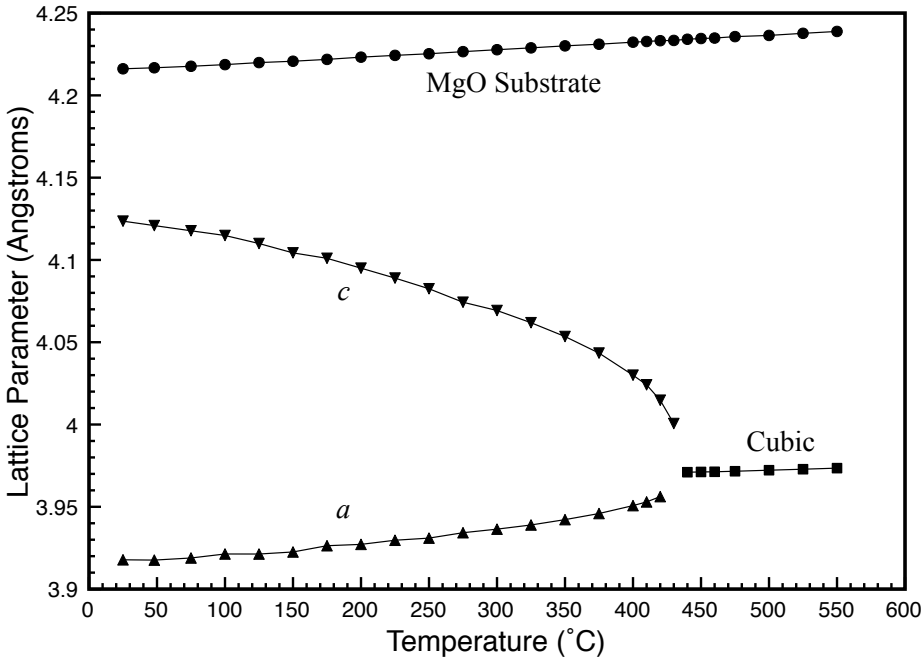

Figure 3.14: Variation of lattice parameters for 500 nm PBT film ($x = 0.9$) on single crystal MgO

3.3.5 Phase Transition

High temperature $\theta - 2\theta$ XRD scans of various PBT thin films indicated that the c lattice parameter decreases with temperature while the a lattice parameter increases, as first observed by Shirane et al. (1950b) on bulk PT. This trend is evident between room temperature and the Curie temperature, T_c. At T_c the films transition to the cubic phase, the lattice parameter of which increases linearly with temperature. Figure 3.14 presents these results for a 500 nm PBT film ($x = 0.9$) along with the lattice parameters of the underlying single crystal MgO substrate.

The transition is rather abrupt, so these scans can be used fairly accurately to determine T_c for various compositions, especially for compositions with higher Pb concentration ($x \geq 0.5$). At lower Pb concentrations and near the phase transition,

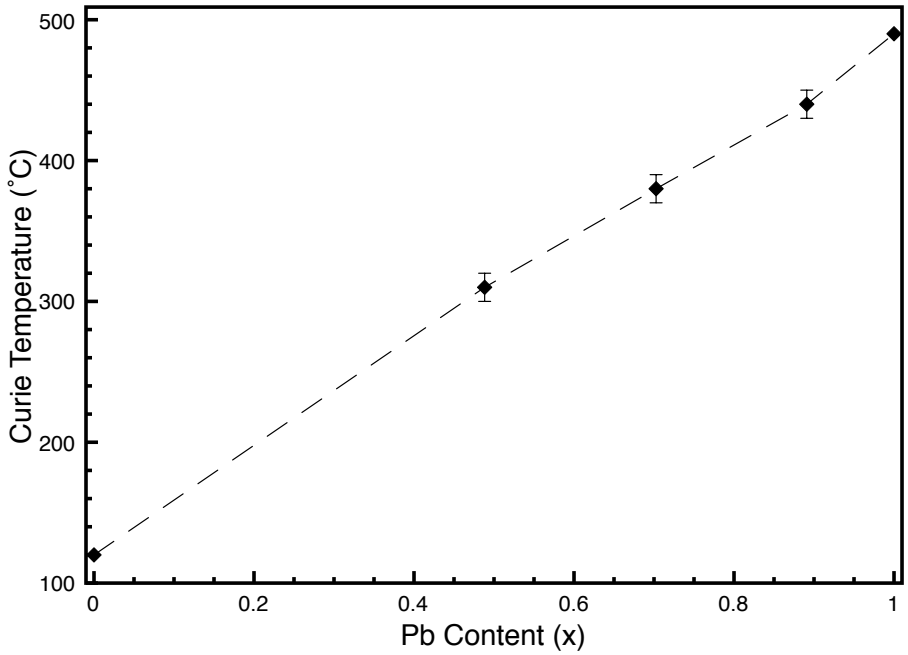

Figure 3.15: Curie temperature of three different PBT thin film compositions vary near-linearly between the transition temperatures of $BaTiO_3$ ($x = 0$) and $PbTiO_3$ ($x = 1$)

it becomes somewhat difficult to reliably distinguish between the near overlapping peaks. Figure 3.15 presents T_c for three PBT thin films of different compositions. The known bulk T_c of both $BaTiO_3$ and $PbTiO_3$ are included on the plot to indicate that T_c varies near-linearly between the end compositions.

3.3.6 Domain Switching

There is experimental and theoretical evidence (Speck and Pompe, 1994; Speck et al., 1994; Kwak et al., 1994; Speck et al., 1995; Foster et al., 1996; Pertsev and Zembilgotov, 1995, 1996; Alpay and Roytburd, 1998) that the domain structure forms as a strain-accommodating mechanism when the system cools through the Curie tem-

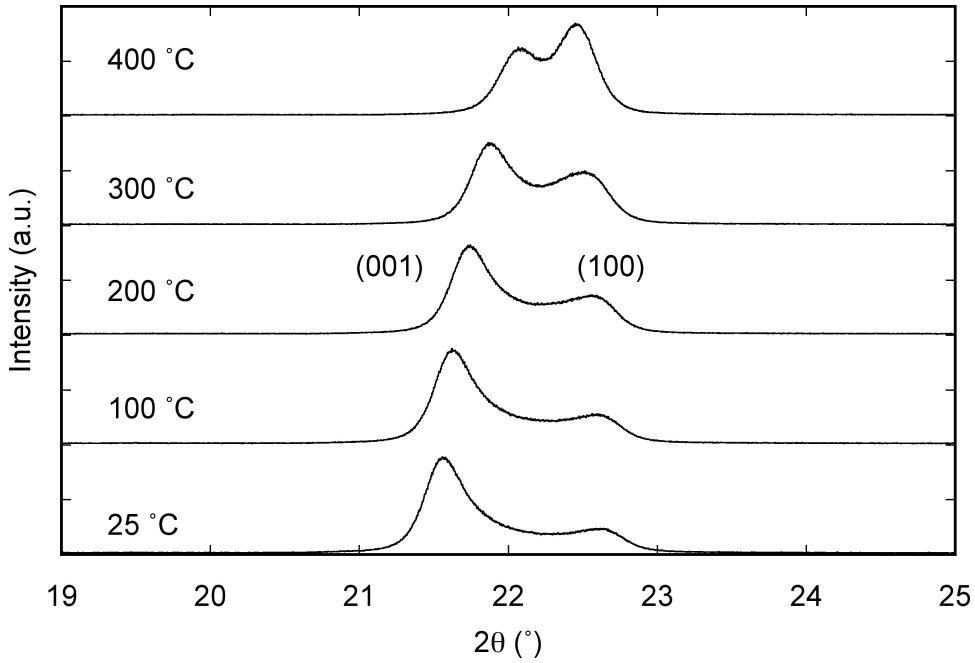

Figure 3.16: Successive HTXRD scans of a 240 nm PT thin film on single crystal MgO with increasing temperature (bottom to top). A domain transition occurs from predominantly c-axis oriented film to mostly a-axis oriented film at higher temperatures.

perature following growth. The net effect is to minimize the total energy of the heterostructure, using the degree of freedom that the tetragonal phase offers in the form of domain switching. In terms of the coherent temperature-dependent stability map (Speck and Pompe, 1994), the films fabricated in this study occupy the mixed a/c portion of the map. This is predicted and experimentally observed for PT on MgO using an effective substrate lattice parameter, b^*, to take into account the misfit dislocations at the film/substrate interface formed during growth (Speck et al., 1994; Foster et al., 1996).

High temperature x-ray diffraction (HTXRD) scans for PBT on single crystal MgO did indeed show a substantial change in c and a domain volume fractions as a

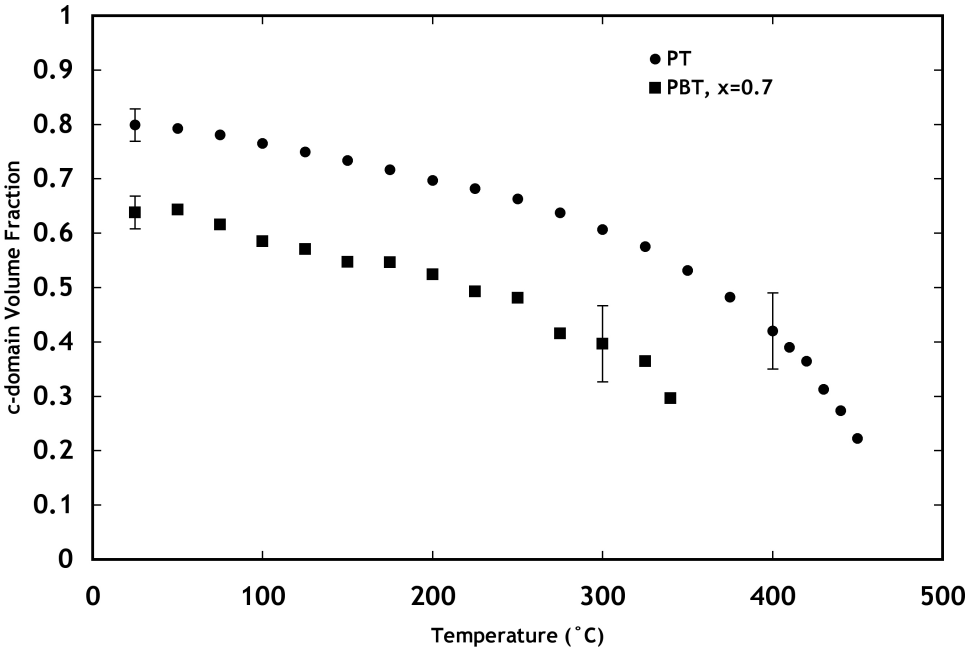

Figure 3.17: Change of c domain fraction with temperature for a 240 nm PT thin film and a 450 nm PBT ($x = 0.7$) film on single crystal MgO.

function of temperature until the phase transition point, as evidenced by the change of intensity of (001) and (100) diffraction peaks. Figure 3.16 features a series of $\theta - 2\theta$ scans of the first order diffraction peaks from a 240 nm PT thin film on single crystal MgO. The spectra are consistent with work predicting and experimentally verifying the change of domain fractions for PT on MgO (Pertsev and Zembilgotov, 1995, 1996), and we here expand the range of compositions for which domain switching with temperature is verified.

A variety of compositions (x $\sim$ 0.5-1) have been tested, and all displayed domain changes similar to the PT/MgO system featured in Figure 3.16. The volume fractions were extracted from the $\theta - 2\theta$ scans by fitting Pseudo-Voigt profile functions (the weighted mean between a Lorentzian and a Gaussian function) to the first order diffraction peaks (001 and 100) to extract better data and deconvolve overlapping

peaks. A standard non-linear least squares refinement procedure was used to arrive at the final fit for each temperature (Levenberg-Marquardt method). Results are shown in Figure 3.17 for PT as well as a PBT film ($x = 0.7$) on single crystal MgO. Results are not included for temperatures nearing the respective Curie temperatures, as it was difficult to reliably deconvolve the (001) and (100) peaks near the transition points.

The results presented here agree with theoretical work (Alpay and Roytburd, 1998) suggesting that for a fully relaxed PT film deposited by MOCVD under similar conditions, the c domain fraction is ~ 0.81 at room temperature (0.8 in Figure 3.17). Furthermore, the reduction in c domain fraction is consistent with the calculations by the same authors.

No such coherent domain switching was observed for the PT thin films deposited on IBAD $MgO/Si_3N_4/Si$. These results, coupled with the absence of 90° domain walls (discussed above) for this type of substrate (due to reduced grain size), suggest that 90° domain boundaries may be critical for the process of domain switching as a strain relief mechanism. Instead, the whole *c* or *a* oriented grains appear to be pinned to the substrate in this specific heterostructure.

3.3.7 Stress in $Pb_xBa_{1-x}TiO_3$ Thin Films by Coherent Gradient Sensing

The domain switching observed in the preceding section has consistently been described in the literature as a strain relaxation mechanism (Speck and Pompe, 1994;

Speck et al., 1994; Kwak et al., 1994; Speck et al., 1995; Foster et al., 1996; Pertsev and Zembilgotov, 1995, 1996; Alpay and Roytburd, 1998) capable of fully relaxing the elastic stress accumulated due to thermal mismatch between film and substrate. Experimental observations, on the other hand, indicate residual strains for $PbTiO_3$ films on MgO (Foster et al., 1995), despite domain switching. Our direct measurement of curvature (and consequently mechanical stress) by CGS (Boyd et al., 2005, 2006) is therefore a valuable tool to study the stress relaxation behavior and correlate it to the domain switching mechanism observed by HTXRD.

Results are presented here for three different $Pb_xBa_{1-x}TiO_3$ films of $x = 1.0$, 0.5, and 0.2 on single crystal MgO. Curvature measurements are taken between room temperature and the growth temperature T_g, 650 °C as outlined in the experimental section above, and the film thicknesses are estimated from CS-SEM as 220 nm, 640 nm, and 430 nm for the three films, respectively.

We begin by examining the raw successive curvature measurements during growth and subsequent cooling of the $x = 1$ film, presented in Figure 3.18. The values in these plots were not averaged. The increased noise at higher temperatures and to some extent during cooling is attributed to convection currents from the reactor body. We observed a trade-off between the grating separation, which determines the sensitivity and thermal noise. The average RMS value using a 10 point adjacent averaging of the measured average curvature during growth is 0.00025 m^{-1}, and this decreases to better than 0.00002m^{-1} at room temperature. The heating and cooling rates were kept low in an effort to maintain equilibrium between the sample and the heater.

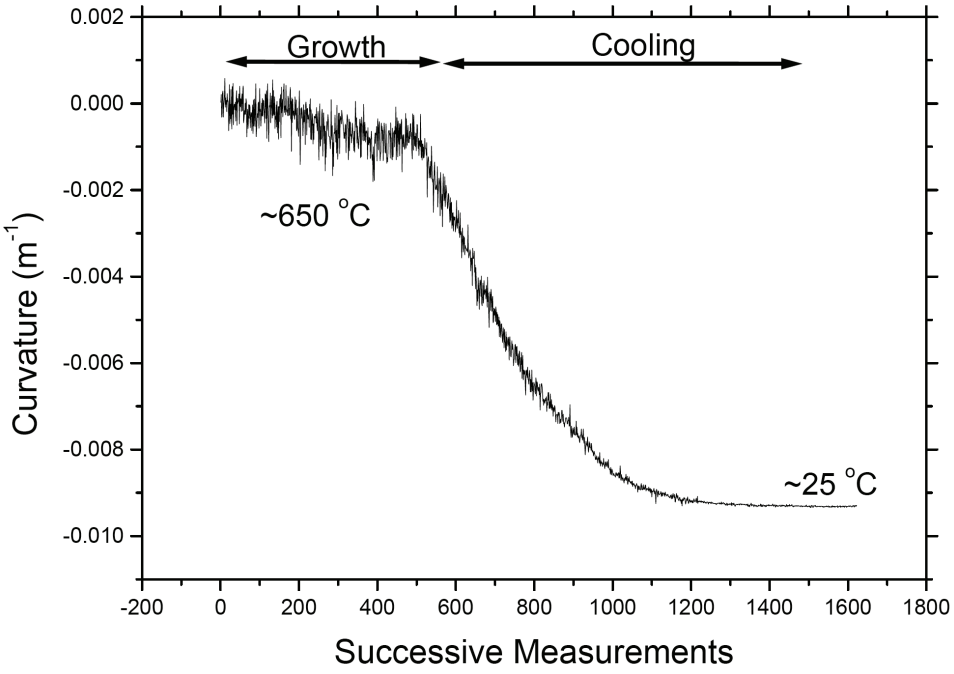

Figure 3.18: Successive, *in situ* curvature measurements during deposition and cooling of 220 nm $PbTiO_3$ thin film on (001) MgO (Boyd et al., 2005). The growth temperature is 650 °C.

Heating the film from room temperature to 650 C took three hours. However, the cooling to room temperature takes place in about five hours due to the large thermal mass of the reactor walls.

Examining Figure 3.18, a compressive stress evolves during growth (negative curvature). This stress can be calculated using Equation (3.1) and is found to be be -110 MPa. The compressive stress continued to accumulate during cooling to room temperature.

The raw curvature data (such as Figure 3.18) have been collected for the three films of different compositions. The sample temperatures during successive CGS measurements are estimated from fourier transform infrared (FTIR) reflectance measurements calibrated against thermocouple measurements inside the heater block (Hammond,

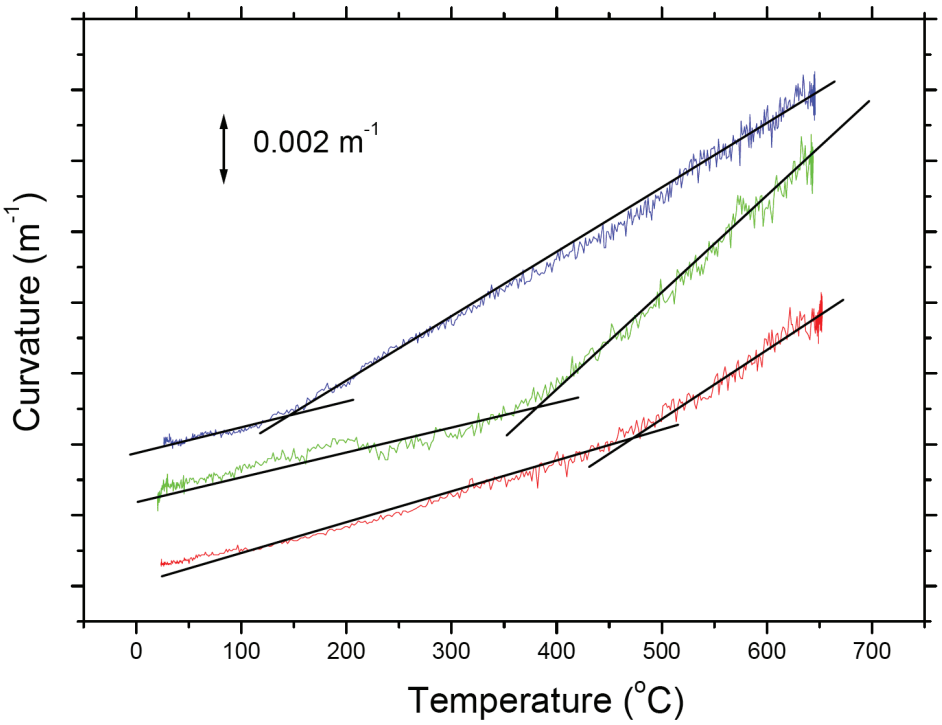

Figure 3.19: *In situ* measurements of wafer curvature taken with increasing temperature from room temperature to T_g for PBT films of compositions $x = 1.0$, 0.5, and 0.2 (bottom to top) on single crystal MgO (Boyd et al., 2006). The data are offset for clarity.

2003). The result is Figure 3.19, allowing us to examine the stress behavior with temperature to look for evidence of stress relaxation.

Figure 3.19 indicates that as the films cool from T_g, the curvature increases in magnitude (more negative) at nearly constant rates. Near $T_c(x)$, this rate decreases as the films approach room temperature. Shown along with the plots of wafer curvature are linear fits to both regions for each composition. The temperature obtained from the intersection of each pair of lines was found to be 468, 350, and 154 °C. For comparison, the $T_c(x)$ observed from HTXRD (Figure 3.15) are 490 and 310 °C for the $x = 1$ and 0.5 films, respectively. There are inherent difficulties in measuring the sample temperature in a warm-wall reactor design, so it is possible that the offset

in this comparison is due to thermal lag and/or measurement error in the growth reactor.

Significant domain switching has been observed for all $Pb_xBa_{1-x}TiO_3$ films grown here (Figure 3.17), and the curvature results (Figure 3.19) indicate that the rate of stress accumulation does decrease below $T_c(x)$, as is expected, but the relaxation is not complete. Theories predicting complete relaxation invariably assume a single crystal film on single crystal substrate, i.e., a perfect heteroepitaxial system. The $Pb_xBa_{1-x}TiO_3$ films on MgO grown here do not qualify as perfect heteroepitaxial systems, despite the high degree of texture. It is possible that the ability to relieve interfacial and growth stresses in these films is limited by the presence of grains.

3.3.8 Functional Characterization

The ferroelectric thin films detailed above have been functionally characterized to investigate their active behavior by various groups at Caltech as part of the Army Research Office-administered project *Engineering Microstructural Complexity in Ferroelectric Devices*.

The hysteresis loops and polarization state of the samples have been investigated using dynamic contact mode electrostatic force microscopy (DC-EFM) and piezo-response force microscopy (PFM) by the Atwater group (Applied Physics at the California Institute of Technology). Figure 3.20 presents hysteresis loops using DC-EFM (after Brewer et al., 2005) that compare an MOCVD-deposited $Pb_xBa_{1-x}TiO_3$ thin film on biaxially textured IBAD $MgO/Si_3N_4/Si$ to films deposited via sol-gel

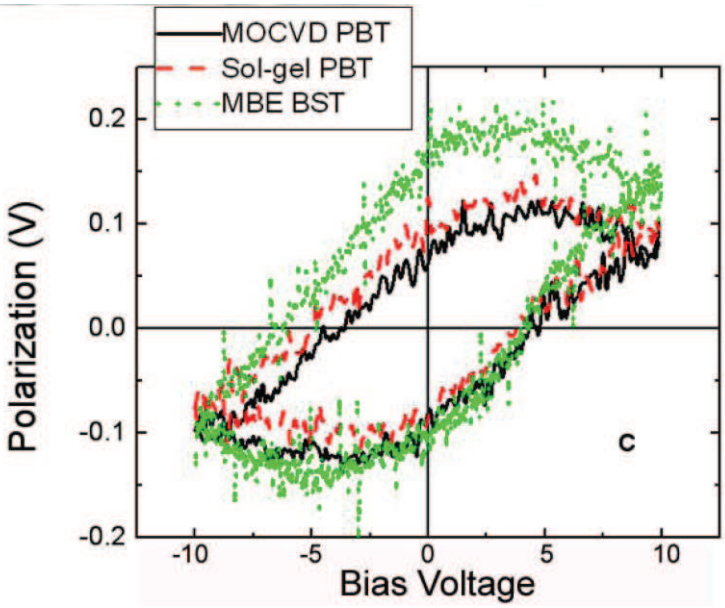

Figure 3.20: Hysteresis loops generated via DC-EFM comparing MOCVD-deposited ferroelectric thin films to those deposited by other techniques. From Brewer et al. (2005).

processing and molecular beam epitaxy. The loops are generated using a conductive AFM tip by applying an AC field over a sample surface biased with respect to the tip. The tip's deflection is sensitive to the local charge density from the local polarization. These loops confirm the functional nature of the films described in this chapter, and the ferroelectric response has been observed on all probed locations on the films' surfaces. The in-plane and out-of-plane polarization states were examined using PFM for MOCVD-deposited polycrystalline $PbTiO_3$ samples on Au/SiO2/Si, and the local piezoelectric coefficient, d_{33} around the sampling tip, was found to be 43.19 pm/V (Ruglovsky et al., 2006).

Mechanical and electromechanical behavior was studied using a custom-built concentrated-loading tool on test structures (cantilevers, bridges, and free-standing membranes)

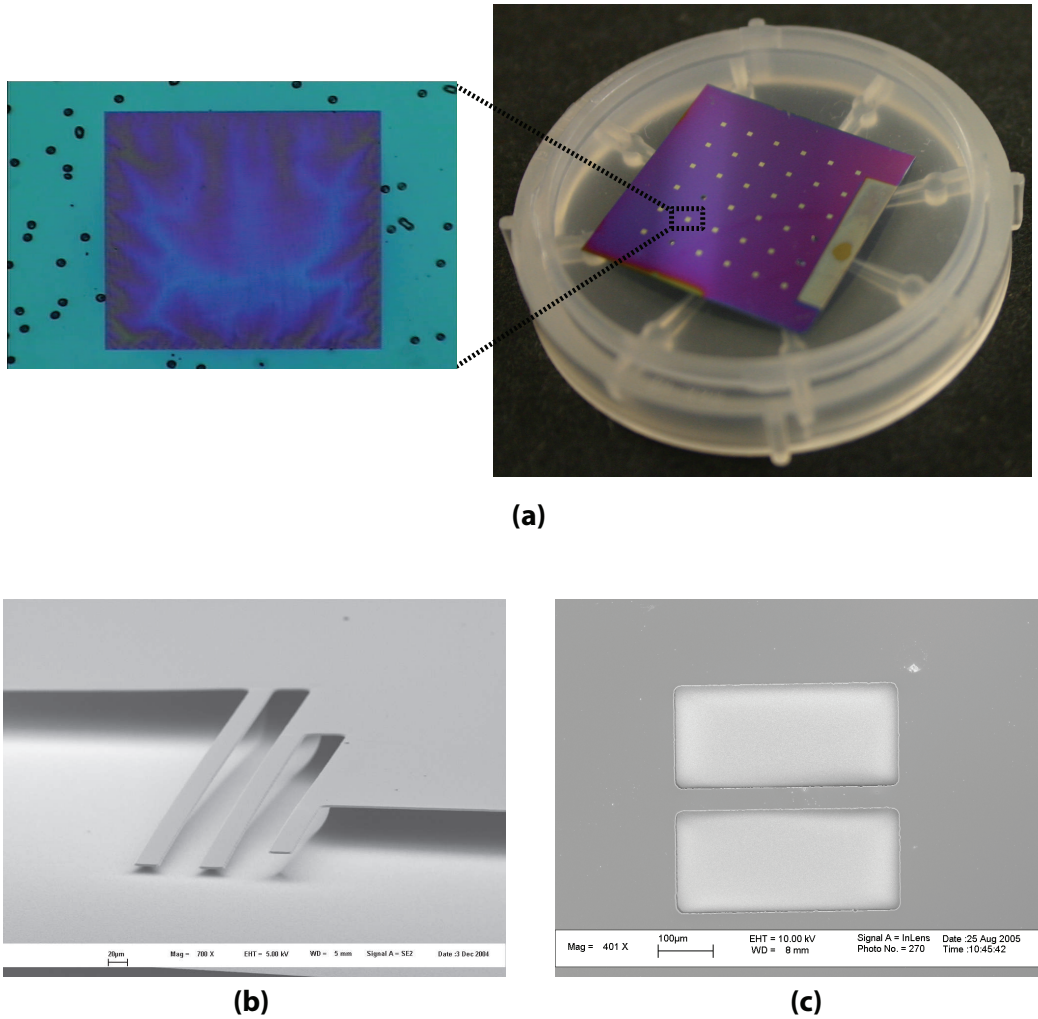

Figure 3.21: Various testing structures for electromechanical characterization including (a) a wafer array of released $PbTiO_3/MgO/Si_3N_4$ membranes (polarized microscope image of single membrane in inset), surface micro-machined (b) cantilevers, and (c) bridges. Cantilevers and bridges micro-machined by Ruglovsky et al. (2006).

and a pressure bulge device (free-standing membranes) in Ravichandran laboratory (Aeronautics) at the California Institute of Technology. This required the preparation of released micro-cantilevers, micro-bridges, and membranes with an MOCVD-deposited ferroelectric active layer. The cantilevers and bridges were micro-machined by isotropic XeF_2 Si-selective etch of SiO_2-masked Si wafers, resulting in 2 μm thick SiO_2 released structures (Figure 3.21). Electrodes were subsequently deposited by thermal evaporation of Au or pulsed laser deposition of $SrRuO_3$ conductive oxide (using IBAD MgO as a texture template). Finally, the active $PbTiO_3$ layer is deposited on top of the resulting heterostructure, and the stress-strain response and piezoelectric switching is studied using the concentrated-loading tool described in Zhang (2005). These experiments are in progress as this thesis is being prepared, and preliminary data were presented in Ruglovsky et al. (2006). Active thin film membranes were prepared by depositing IBAD MgO and $Pb_xBa_{1-x}TiO_3$ directly on commercially obtained TEM window wafers (Structure Probe, Inc.), i.e., an array of 50-200 nm Si_3N_4 released membranes. Figure 3.21 contains optical microscope and SEM pictures of the cantilevers, bridges, and membranes. These membranes (0.5 mm squares) were also examined using the concentrated-loading device as well as a pressure bulge test (Zhang, 2005).

3.4 Conclusion

$Pb_xBa_{1-x}TiO_3$ ferroelectric thin films were successfully deposited on both single crystal MgO and biaxially textured $MgO/Si_3N_4/Si$ substrates using MOCVD. A system-

atic comparison using SEM, XTEM, XRD, and XRD pole figures indicated the absence of 90° twin boundaries for PBT on the biaxially textured MgO, and we attribute this result to the reduced grain size on this type of substrate when compared to larger PBT grains, containing twin boundaries, on single crystal substrates.

Changes in domain fractions were observed in films containing 90° domain boundaries, as a function of temperature, using HTXRD. These results are consistent with theoretical work suggesting that the domain switching acts as a strain-relief mechanism to reduce the overall energy of the heterostructure upon transition to the tetragonal phase. The stress was measured *in situ* during deposition and subsequent thermal cycling for PBT films on single crystal MgO substrates, and the results indicate that the rate of stress accumulation does decrease below the Curie temperature, but the stress relaxation is not complete. No such changes were observed for films lacking twin boundaries on biaxially textured MgO templates.

We also utilized EBSD as a tool to study the texture of the ferroelectric thin films by presenting texture data in the form of in-plane and normal axis IPFs that are consistent with the XRD results. Orientation data from EBSD further confirmed the presence of 90° domain boundaries for PBT on single crystal MgO, evidenced by measuring the tetragonal tilt angle. The combination of superior resolution and large spatial extent makes EBSD a powerful tool to probe the near-surface domain microstructure and full texture information of ferroelectric thin films and microstructures directly in the SEM.

Chapter 4

Pulsed Laser Deposition of $SrRuO_3$ Electrodes on MgO

4.1 Introduction

Considerable attention has been dedicated to $SrRuO_3$ thin films in the past fifteen years as a result of their useful electrical, magnetic, and optical properties. $SrRuO_3$ is a conductive oxide, paramagnetic at room temperature and ferromagnetic below 160 K, (Longo et al., 1968) with a high remnant magnetization and magento-optical constant, making it a candidate for various electronic and optical devices. For example, being a suitable epitaxial template for many perovskite materials, it has been used as a buffer for highly-oriented YBCO superconducting thin films and as a normal-metal layer in high-temperature superconductor Josephson junctions (Antognazza et al., 1993). More relevant to this thesis, ferroelectric thin film capacitors with $SrRuO_3$ electrodes result in superior leakage and fatigue characteristics as demonstrated by Eom et al. (1993). This makes it a promising electrode, both for memory applications and the high strain thin film micro-actuators discussed in the previous chapter.

$SrRuO_3$ has an orthorhombic distorted-perovskite structure (a=5.57Å, b=5.53Å,

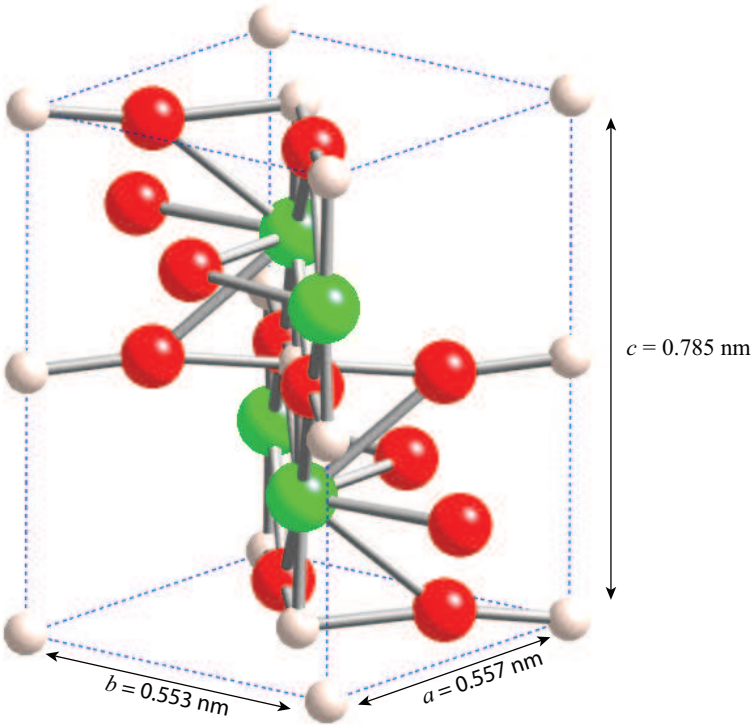

Figure 4.1: Orthorhombic crystal structure of $SrRuO_3$. Oxygen, ruthenium and, strontium atoms are represented in red, white, and green, respectively.

and c=7.85Å). However it can also be treated as a pseudo-cubic structure with $d_{(110)}$ = 3.93Å(Eom et al., 1992). The crystal structure is illustrated in Figure 4.1. The pseudo-cubic structure provides the relevant lattice parameter for matching with the tetragonal ferroelectrics discussed in this thesis ($BaTiO_3$: $c = 4.038\mathring{A}$ and $a = 3.994\mathring{A}$. $PbTiO_3$: $c = 4.151\mathring{A}$ and $a = 3.905\mathring{A}$). Lattice matching results in textured ferroelectric thin films (as is demonstrated for $Pb_xBa_{1-x}TiO_3$ on MgO in Chapter 3) that can potentially be used for high-strain switching.

In short, textured $SrRuO_3$ thin films have a unique combination of properties when integrated with ferroelectrics; they are both texture templates and electrodes that lead to high-strain fatigue-free ferroelectric performance.

Most of the results for epitaxy of $SrRuO_3$ are reported on $SrTiO_3$ (see, for exam-

ple, Chen et al., 1997; Jiang et al., 1998) and $LaAlO_3$ (Jia et al., 1997) substrates due to the superb lattice match (a_{SrTiO_3}=3.905Å, a_{LaAlO_3}=3.838Å), including detailed microstructural and texture characterization. Fewer results are reported on the low-cost MgO (a=4.213Å) substrates as noted in Singh et al. (2002) due to the larger lattice mismatch. Previous detailed microstructural studies of $SrRuO_3$ on MgO stem from the work of Jia et al. (2002, 2003), who demonstrated that YBCO/$SrRuO_3$/IBAD MgO heterostructures produced superior YBCO superconducting properties.

We use MgO as a bottom template for epitaxy of $SrRuO_3$ and ferroelectric films because it has been shown to develop narrow biaxial texture on amorphous Si_3N_4 and Si-based substrates via IBAD (Brewer et al., 2005; Wang et al., 1997) and is therefore a promising layer for integration of $SrRuO_3$ and ferroelectric films with CMOS-processing. This motivates the work presented in this chapter dealing with the deposition of textured $SrRuO_3$ thin-film electrodes on MgO and Si-based substrates, the latter using IBAD MgO buffer layers. This enables the synthesis of fatigue-free and textured ferroelectric layer/$SrRuO_3$/IBAD MgO/Si heterostructures for high-strain applications.

A new pulsed laser deposition (PLD) chamber for the deposition of oxide electrodes, as well as the experimental conditions required to achieve highly-oriented $SrRuO_3$ films on single crystal MgO and amorphous Si-based substrates buffered by IBAD MgO, are described below. We then present a detailed study of the microstructure and full texture before finally demonstrating the viability of these films as electrodes and texture templates for highly oriented ferroelectric thin films.

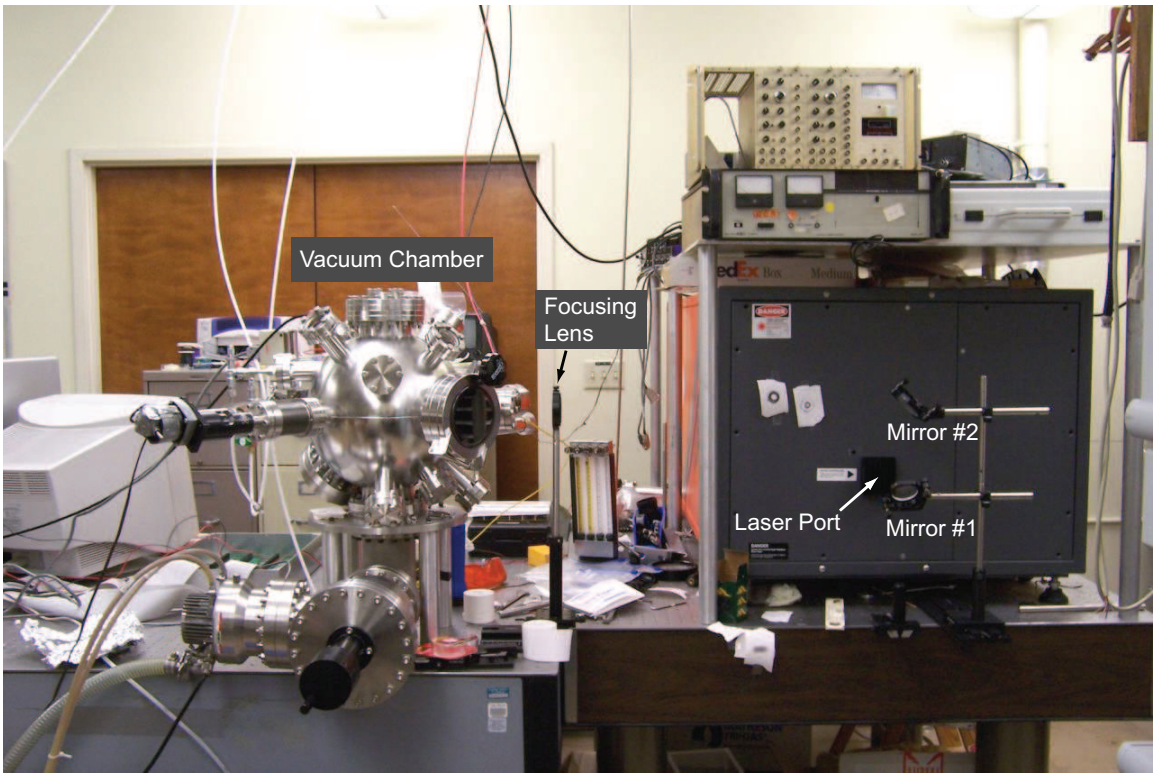

Figure 4.2: Pulsed Laser Deposition System.

4.2 Pulsed Laser Deposition System

Figure 4.2 is an annotated picture of a custom PLD system used to deposit $SrRuO_3$ thin films. The high-power laser is a Lambda-Physik excimer laser (model Lextra 200) used with a KrF gas fill to generate 248 nm wavelength pulses up to 10 Hz in frequency with a nominal pulse length of 34 ns. The beam energy is adjustable up to 1 Joule/pulse maximum ouput distributed over a 2 cm $\times$ 1cm rectangular beam profile.

The output beam is guided using two UV-grade dielectric-coated fused silica mirrors at 45° incidence (CVI Laser model KRF-2037-45), the first of which raises the beam vertically to the correct level, while the second turns the beam horizontally at

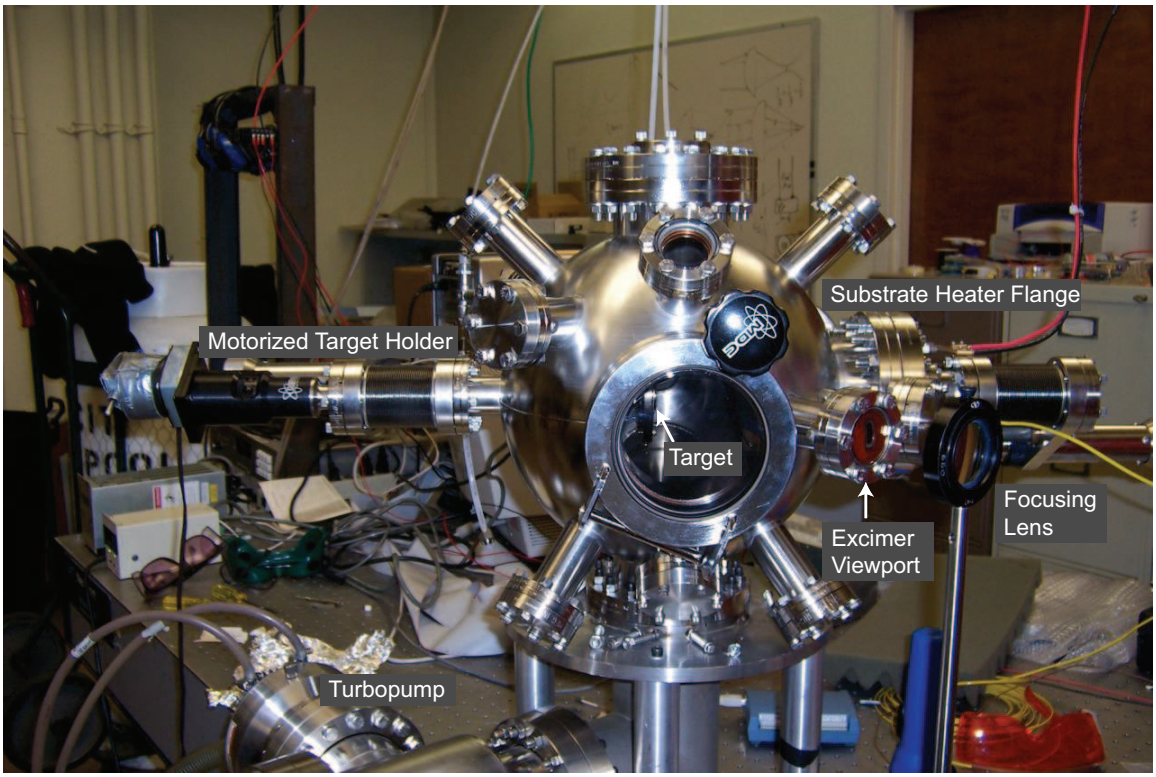

Figure 4.3: Vacuum chamber of the PLD system. A focusing lens focuses the excimer beam ahead of entry through the chamber's laser window onto the target inside the chamber. The target is on a motorized rotary holder and faces the substrate heater on the opposite side of the chamber. The turbopump is also in view.

a right angle, re-directing it towards a fused silica focusing lens ahead of the vacuum chamber's optical viewport. Both mirrors are mounted on a linear translating stage for easy alignment with the vacuum chamber, which is a standard 12 inch diameter spherical vacuum chamber from Huntington Mechanical Laboratories, with many ports for diagnostics, gas flow, and pumping (Figure 4.3). The chamber is pumped by a Varian 200 turbopump, which is in turn backed by a Varian DS-102 rotary-vane pump charged with a Krytox inert pump oil for oxygen compatibility. Base pressure in the chamber is 5×10^{-7} Torr, as measured by an ion gauge, but deposition of $SrRuO_3$ is typically done in 100-250 mTorr of O_2 pressure, corresponding to tens of

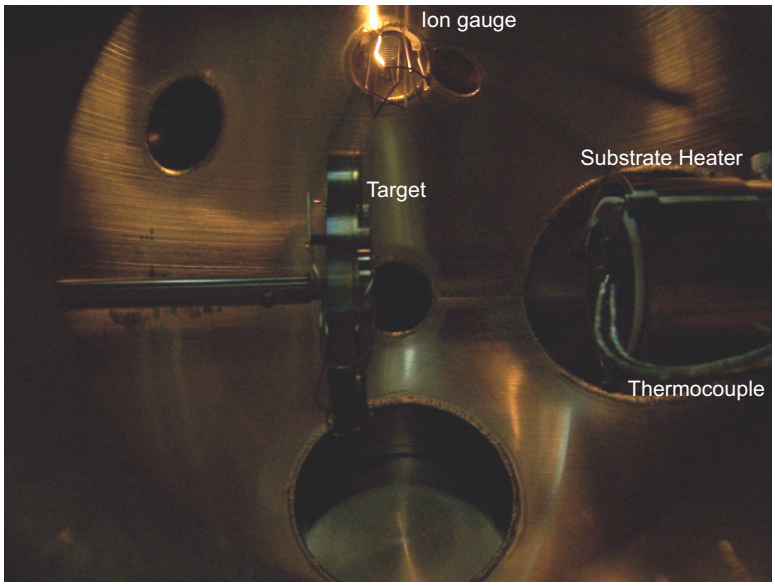

Figure 4.4: A view inside of the PLD vacuum chamber showing the $SrRuO_3$ target facing the substrate heater.

cubic centimeters per minute of O_2 flow. Rough vacuum is measured by a Varian WV100-2 wide range diaphragm transducer gauge.

The focusing lens has a focal length of approximately 30 cm (CVI Laser model PLCX-50.8-154.5-UV-248), and the excimer window is a fused silica viewport with over 90% transmission at 248 nm (Insulator Seal model 9722005). The focused beam strikes the $SrRuO_3$ target, which is mounted on a rotary motorized feed-through inside the vacuum chamber as can be seen in Figure 4.3 through the chamber's glass loading door. The rotating $SrRuO_3$ target faces the substrate heater in the chamber, as is shown in Figure 4.4, which is an inside view of the vacuum chamber, so the ejected plume from the target's surface is directly transferred to the substrate mounted on the heater.

The substrate heater is a 2 inch diameter modified HeatWave Labs design (model 101275 button heater inside a modified model 101446 assembly) capable of achieving

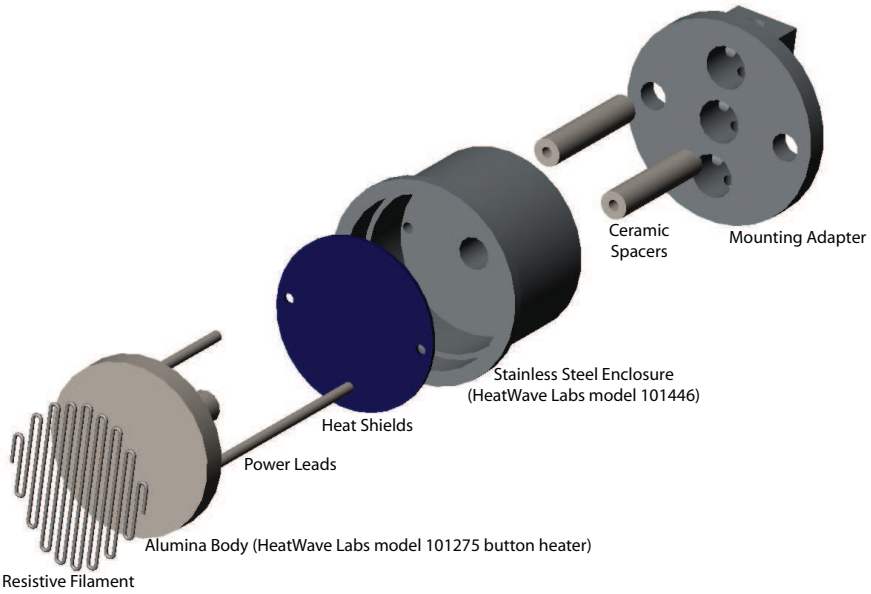

Figure 4.5: Design of the PLD substrate heater and mounting adapter. See Figure 4.6 for a picture of the final assembly.

a sample temperature of 1200 °C (using 12V/20A) in a UHV/oxidizing environment. The heating element is a precious metal resistive filament 0.04 inches diameter inside an Al_2O_3 heater block, surrounded by a stainless steel enclosure with heat shields. A type K thermocouple is attached to one of the sample clips on the heater block's surface for continual monitoring of operating temperature. The schematic design is featured in Figure 4.5, while Figure 4.6 is a picture of the final assembly on the mounting flange prior to use in the vacuum chamber. The power is supplied to this heater from an HP 6268B power supply, rated for 50V/35A and instrumented for external control of output voltage using a PC. The heater's current is measured using a DC current sensor (American Aerospace Controls model 952-50-B). Figure 4.7 is a picture of the glowing heater assembly during operation while power is being supplied to the resistive filament.

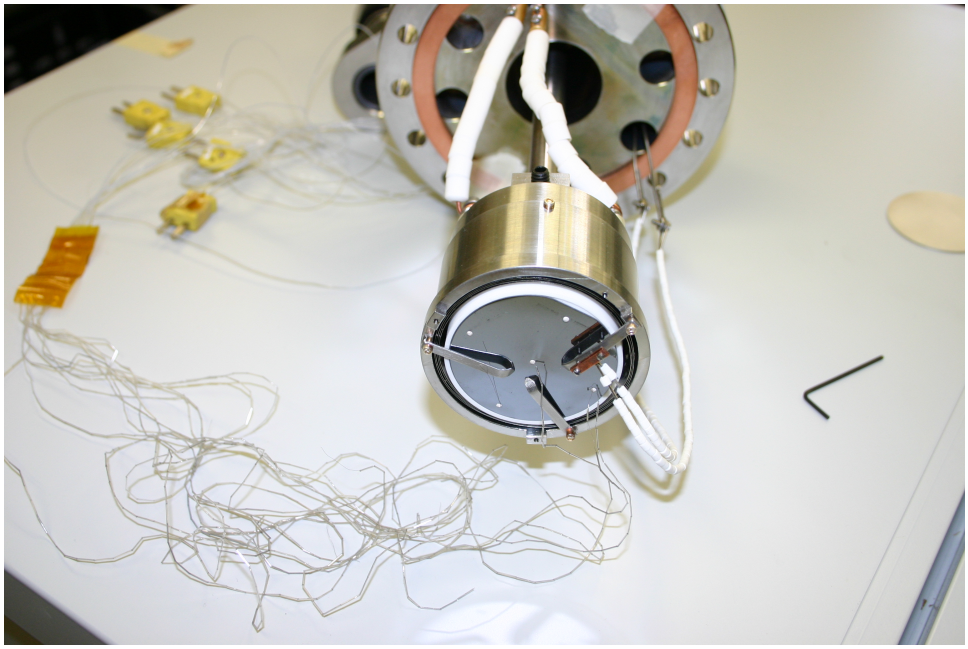

Figure 4.6: A picture of the final substrate heater prior to use in the vacuum chamber. A calibration silicon wafer with many bonded thermocouples is mounted on the heater face. A permanent type K thermocouple can be seen attached to one of the wafer clips. Two power leads, surrounded by ceramic fish spine beads, carry the power from the external power supply to the heater through the vacuum flange.

Figure 4.7: The substrate heater of the PLD system during operation.

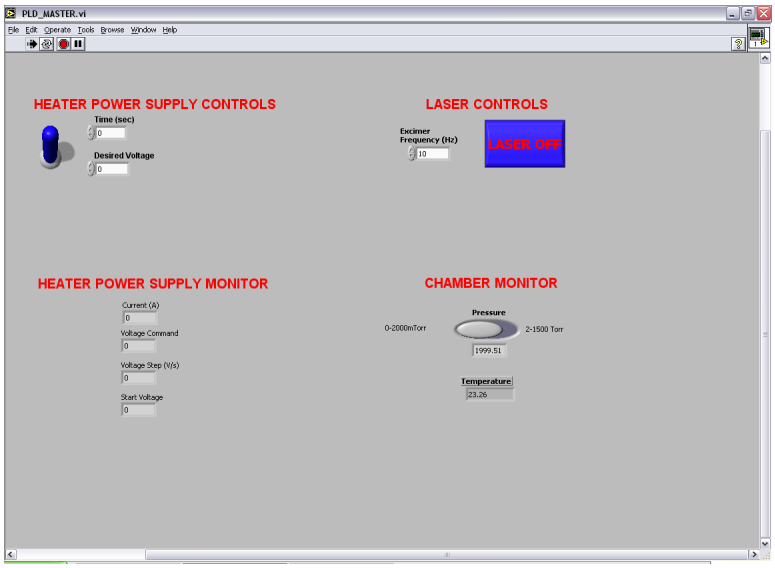

Figure 4.8: LabVIEW interface to the PLD system.

The entire PLD apparatus is controlled using a PC equipped with a LabVIEW program, an A/D board (Measurement Computing PCI-DAS1602/12), a D/A board (Measurement Computing PCI-DDA08/12), and a thermocouple measurement board (Measurement Computing USB-TC). The program interfacing with these DAQ boards (Figure 4.8) allows for direct monitoring of chamber pressure, sample temperature, and heater power in addition to direct control of the heater's power supply, ramp rate, and cool-down. It also allows for remote control of the excimer laser, including the operating frequency.

4.3 Experimental

The films described in this chapter were deposited using one of two experimental set-ups under the same experimental conditions. One is a recently-acquired commercial Neocera PLD system in Watson laboratory (California Institute of Technology), and

Target	Stoichiometric $SrRuO_3$
Substrate-target distance	9-10 cm
Substrate temperature	~650 °C
Pressure	100-250 mTorr O_2
Laser	KrF excimer, 248 nm
Laser fluence	5-10 J/cm^2
Laser frequency	10 Hz

Table 4.1: Deposition conditions for PLD of $SrRuO_3$ on MgO and MgO/Si.

the other is a new custom facility assembled as part of this thesis and described above.

The vacuum chamber was evacuated to base pressure prior to deposition. Films were then deposited in an oxygen pressure (100-250 mTorr) on the heated substrates (~650 °C). Two types of substrates were used: commercially obtained single crystal MgO (used as received) substrates as well as amorphous Si_3N_4/Si using 20 nm IBAD (ion beam-assisted deposition) MgO followed by 20 nm homoepitaxial MgO as a templating layer. Details on the IBAD MgO process can be found in (Brewer et al., 2005). The target was commercially-obtained stoichiometric $SrRuO_3$ (SCI Engineered Materials, Inc). The growth conditions are summarized in Table 4.1. Figure 4.9 is a picture of the plume ejected from the $SrRuO_3$ target during deposition under these conditions.

4.4 Results and Discussion

The thickness was found to be about 160 nm (from 18000 pulses), as measured by scanning a surface profilometer between a film's surface and a masked area. The

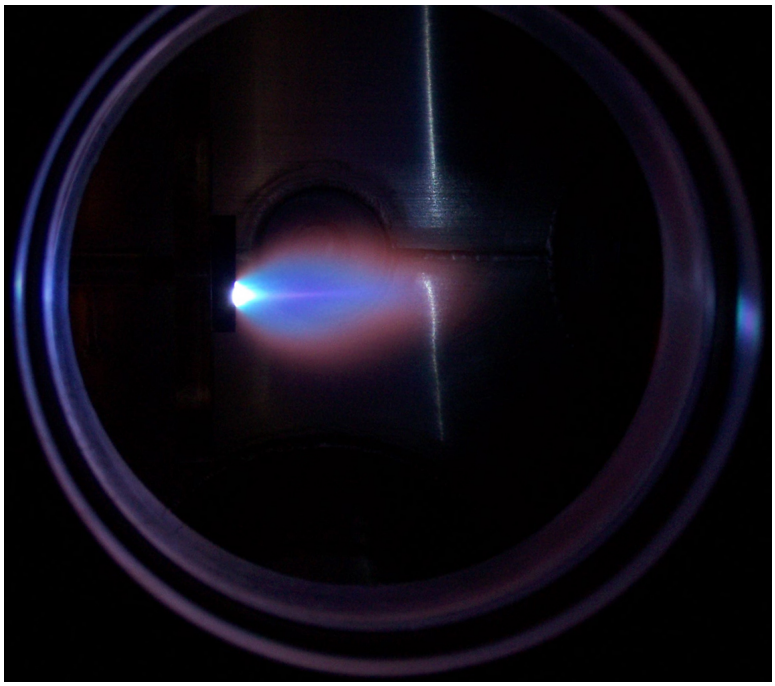

Figure 4.9: Picture of the plume ejected from a $SrRuO_3$ during pulsed laser deposition.

films' surfaces were found to be smooth and transparent, and SEM imaging revealed surface features of ∼150 nm and ∼65 nm average for $SrRuO_3$ on single crystal MgO and biaxially textured MgO/Si, respectively. Figure 4.10 compares representative surfaces of the $SrRuO_3$ films on the two substrates. We attribute the reduced grain size on the Si substrate to the characteristically small grains of the IBAD MgO templating layer. Four-probe resistivity measurements on optimized samples revealed a resistance of ∼1.5 mΩ-cm, which is about 5 times larger than the expected bulk value. The literature suggests that the resistivity of $SrRuO_3$ thin films varies strongly with the deposition temperature. For example, Zakharov et al. (1999) report the lowest resistance from a deposition temperature of 775 °C, while films deposited at lower and higher temperatures had higher resistivities by a few-fold. That is consistent with the resistivity obtained here from samples deposited at ∼650 °C.

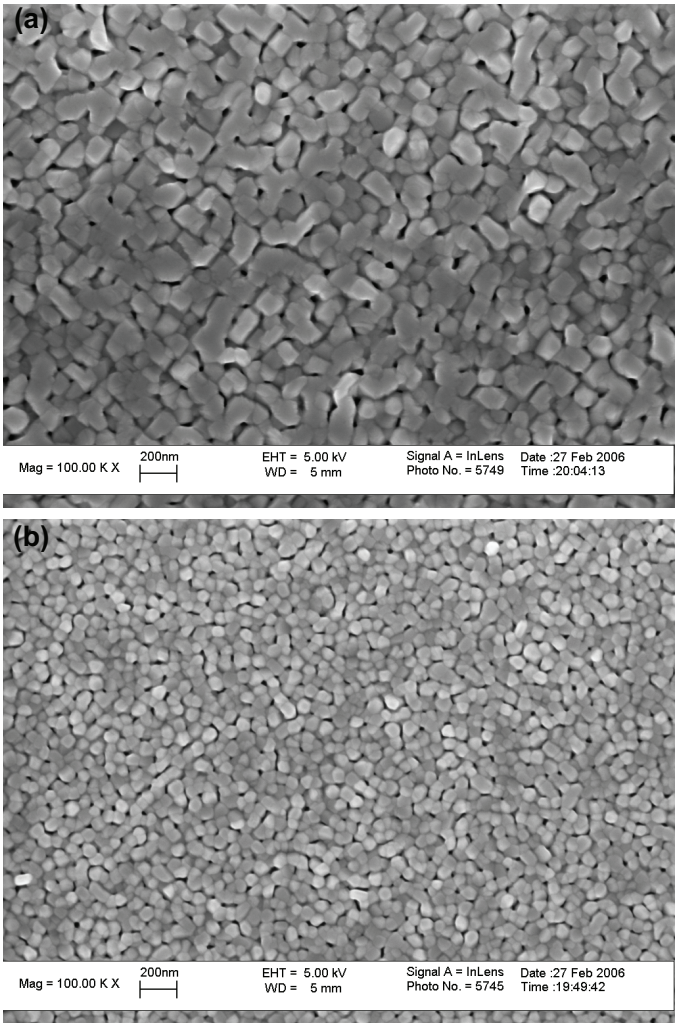

Figure 4.10: Surface SEM images from $SrRuO_3$ on (a) single crystal MgO and (b) biaxially textured MgO templates/Si_3N_4/Si.

4.4.1 Orientation

One of the difficulties in indexing $SrRuO_3$ peaks from $\theta - 2\theta$ XRD spectra alone is the degeneracy or near-degeneracy of many of the peaks for this specific structure. Figure 4.11 is a calculated $\theta - 2\theta$ spectrum of random powder $SrRuO_3$ using ICSD (inorganic crystal structure database) code 50341 (Kennedy and Hunter, 1998), indicating the degeneracy of all three $SrRuO_3$ orientations observed in Figure 4.12, which is a scan of a PLD-deposited $SrRuO_3$ thin film on single crystal MgO (100). The three degenerate

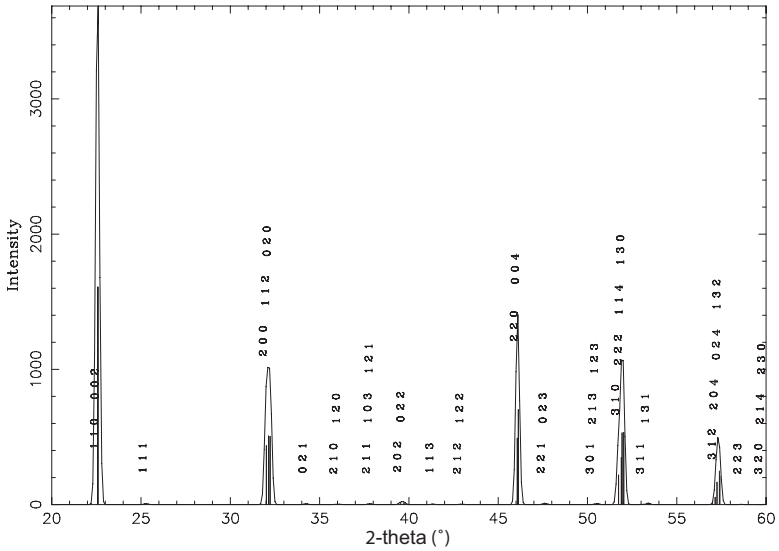

Figure 4.11: Powder diffraction scan of $SrRuO_3$ using structure data from ICSD 50341

peaks are namely the most intense 110/002 (or 220/004 second order) pair as well as the more minor 200/020/112 and 312/024/204 peaks.

The final indexing of these peaks as 002 (004 for second order), 112, and 024 in Figure 4.12 is the result of a more careful analysis that took into account the intensity of different orders of diffraction and the texture distribution of the deposited films using x-ray pole figures, in Section 4.4.2 below, that allows for analyzing the angular relationship between these crystallites on the pole figure. This is an important step in the characterization of $SrRuO_3$ electrodes since the texture of this layer affects the texture and, consequently, the properties of the ferroelectric active layer. The final result is that the $SrRuO_3$ film in Figure 4.12 is predominantly $(00l)$ out-of-plane oriented, and the accompanying RHEED image confirms the crystalline nature of the film.

$SrRuO_3$ was also deposited on Si using biaxially textured buffer layers of IBAD

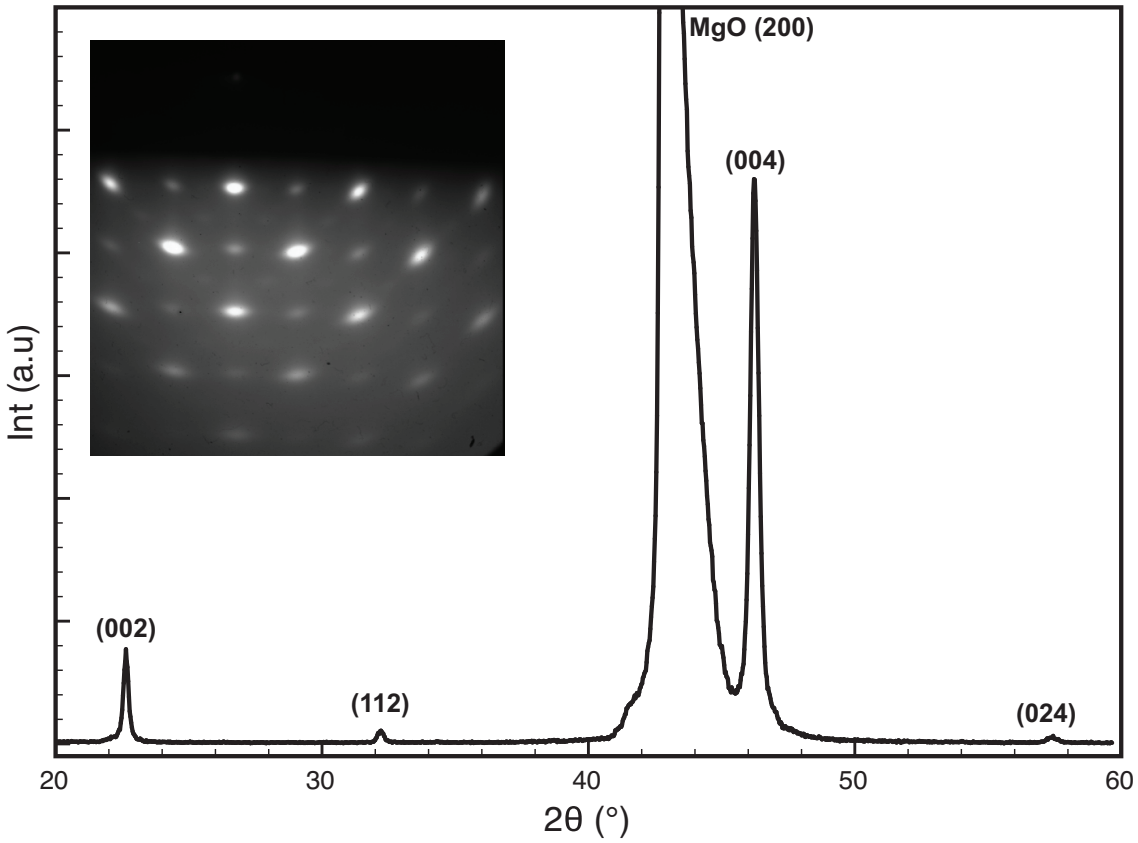

Figure 4.12: $\theta - 2\theta$ XRD scan of $SrRuO_3$ thin film on single crystal MgO indicates the film is predominantly $(00l)$ oriented. The inset RHEED pattern attests to the film's high degree of crystallinity.

MgO. The XRD and RHEED scans on films grown at a lower temperature ($T_g = 510$ °C) show a more polycrystalline structure, while similar scans for films of $T_g = 650$ °C show a single $(00l)$ orientation. These results are shown in Figure 4.13. Specifically, the (200)/(112)/(020) peak all but disappears as the growth temperature increases, and the RHEED pattern changes from ring-like to distinct spots. From these results, coupled with rocking curve scans (below), we conclude that $SrRuO_3$ inherits the biaxial texture from the MgO buffer layer on Si.

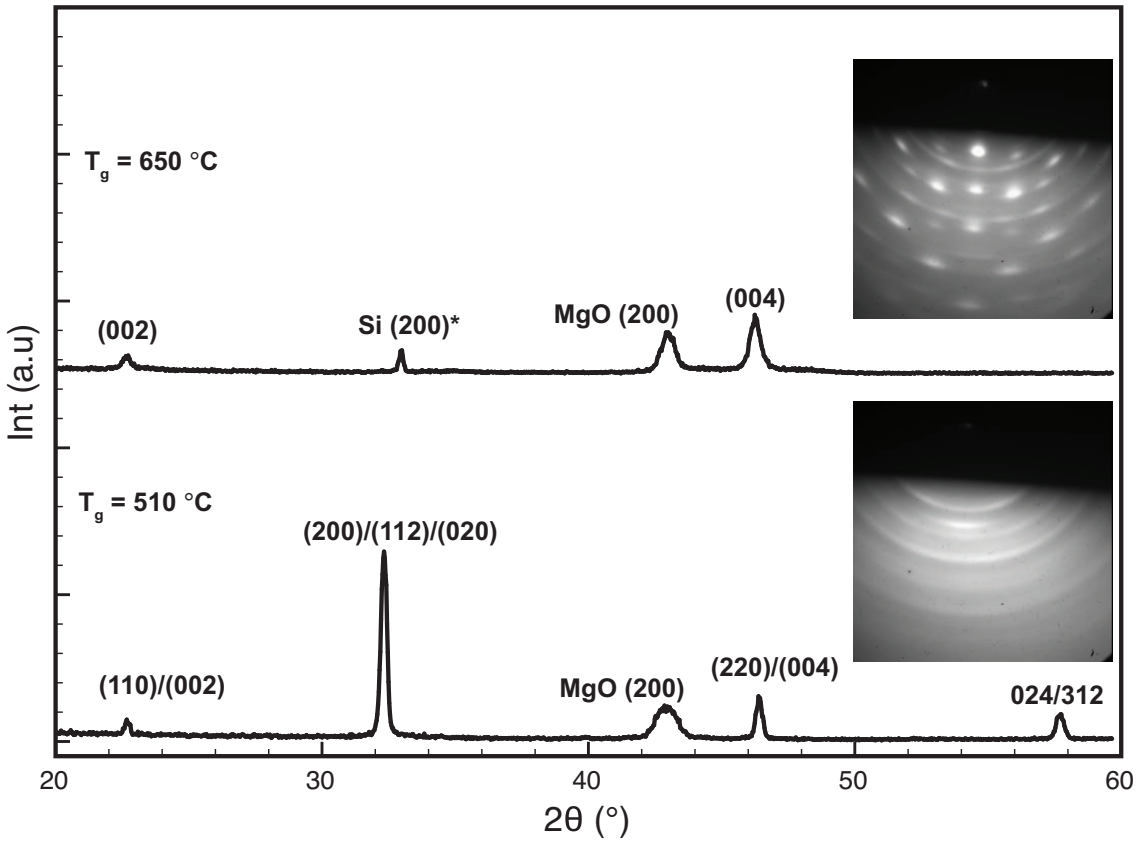

Figure 4.13: $\theta - 2\theta$ XRD scans of $SrRuO_3$ thin film on Si using biaxially textured buffer layers of IBAD MgO. The increase in growth temperature allows for the deposition of highly-oriented $(00l)$ films. The RHEED insets confirm this result as the pattern transforms from polycrystalline rings to distinct spots. While the (200) reflection is forbidden in silicon due to a zero structure factor, it can arise due to multiple-beam scattering, as observed and explained in (Tischler et al., 1988).

4.4.2 Texture

We here examine the full texture of the deposited films by diffracting from planes that are away from the axis defined by the wafer's surface normal to confirm the epitaxial quality of $SrRuO_3$ on MgO. Figure 4.14 is a pole figure of a $SrRuO_3$ film on single crystal MgO with 2θ set to 32.2° (200/020/112 bragg condition). The four largest peaks at 45° away from the the (112) central pole correspond to the majority $(00l)$ grains. The fourfold symmetry is indicative of good in-plane texture. A small central

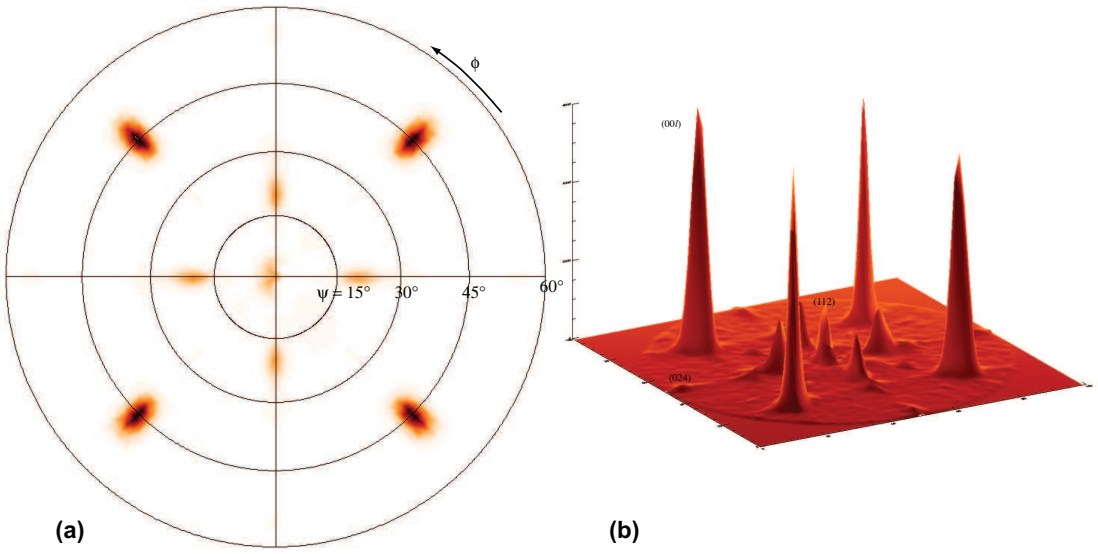

Figure 4.14: (a) An x-ray pole figure scan of $SrRuO_3$ on single crystal MgO indicating in-plane texture. The four largest peaks at 45° away from the center correspond to the majority (00l) grains. (b) is a surface representation of the same plot illustrating the relative intensities and identifying grains by their $\theta - 2\theta$ labels (Figure 4.12).

peak and other minor peaks represent the less prevalent crystallites with non-(00l) orientation observed in the $\theta - 2\theta$ scan (Figure 4.12). Less of the sample is exposed to the x-rays at higher ψ angles, and some of the non-(00l) grains are from the generally more intense (200/020) diffraction instead of (112). Therefore, this pole figure over-represents the non-(00l) grains; the film is primarily (00l) out-of-plane oriented and has strong in-plane texture.

We now turn our attention to quantitative texture characterization of $SrRuO_3$ on Si using biaxially textured MgO buffer layers. These films are exclusively (00l) oriented when deposited at higher temperatures, as as can be seen in Figure 4.13. The out-of-plane texture is examined via an ω rocking curve and the in-plane texture via a ϕ scan at ψ of 45°, which is equivalent to a circumferential slice of the pole

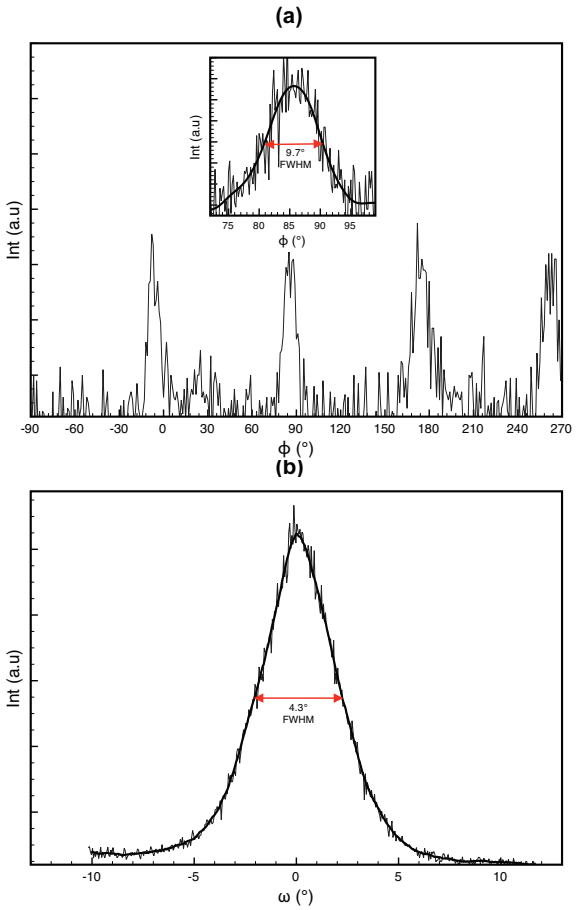

Figure 4.15: (a) ϕ scan of $SrRuO_3$/MgO/Si (2θ=32.2° and $\psi = 45°$) with four peaks indicating in-plane texture and a finer scan of single peak revealing the FWHM of 9.7° (b) Rocking curve for out-of-plane texture of $SrRuO_3$/MgO/Si using the (004) plane revealing a FWHM of 4.3°.

figure that goes through the four most intense diffraction spots. These results and the obtained full-width at half-maximum (FWHM) values are presented in Figure 4.15 as quantitative indicators of out-of-plane and in-plane textures. For the in-plane characterization, a lower intensity but highly monochromatic CuK_α beam is used in a high resolution thin film diffractometer (Philips MRD). A crude scan (large steps in ϕ) is first done to confirm the location of the four diffraction spots (starting ϕ is arbitrary), followed by a finer scan (0.2° step) on one of the peaks (inset) to measure the FWHM. The FWHM values of the ω and ϕ rocking scans are 4.3° and 9.7°,

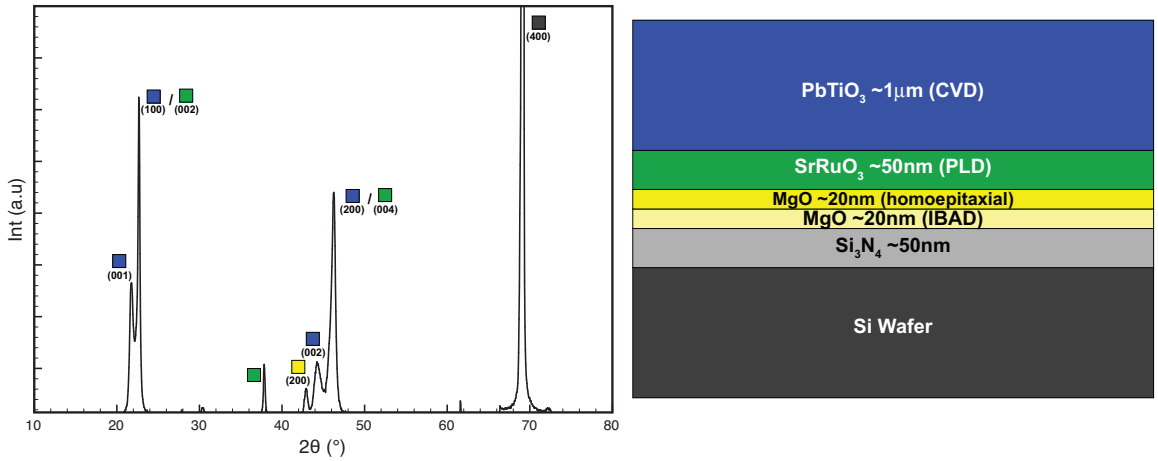

Figure 4.16: $\theta - 2\theta$ scan of a $PbTiO_3/SrRuO_3/MgO/Si_3N_4/Si$ system. $PbTiO_3$, $SrRuO_3$, and MgO deposited by MOCVD, PLD, and IBAD, respectively, on a Si_3N_4/Si wafer demonstrating the ability to integrate highly-oriented ferroelectrics with silicon directly complete with oxide electrodes for fatigue-free behavior.

respectively.

From the $\theta - 2\theta$ XRD results and pole locations in the x-ray pole figure scans relative to the MgO cubic lattice, it is possible to conclude that the predominant epitaxial relationship of $SrRuO_3$ on MgO is $(001)_{SRO}\|(001)_{MgO}$ and $<110>_{SRO}\|<100>_{MgO}$. This is consistent with cube-on-cube epitaxy, where the $SrRuO_3$ structure is treated as pseudo-cubic.

4.5 A Textured Ferroelectric/$SrRuO_3$/MgO/Si_3N_4/Si System

From the results presented in the current and preceding chapters, we conclude that both $Pb_xBa_{1-x}TiO_3$ and $SrRuO_3$ inherit the biaxial texture of IBAD MgO buffer layers. This allows for the integration of highly-oriented ferroelectrics with silicon di-

rectly, complete with oxide electrodes for fatigue-free behavior. Figure 4.16 illustrates this unique heterostructure and contains a $\theta - 2\theta$ XRD scan containing information on the orientation of all the layers. The $PbTiO_3$ functional layer, $SrRuO_3$ electrode, and MgO biaxial template in this sample are deposited by MOCVD, PLD (courtesy of Dan Potrepka, Army Research Lab), and IBAD, respectively, on a Si_3N_4/Si wafer.

4.6 Conclusion

Conductive oxide $SrRuO_3$ thin films were prepared by pulsed laser deposition (PLD) for the purpose of integration with ferroelectrics onto Si-based substrates for CMOS compatibility. The focus was on achieving a high degree of texture so that $SrRuO_3$ films are used both as electrodes and growth templates for the textured active ferroelectric layers.

The $SrRuO_3$ films were deposited on MgO single crystals and Si (using biaxially textured MgO buffer layers). On both substrates, the films were predominantly $(00l)$ oriented and in-plane textured as shown by x-ray pole figures. Out-of-plane ω and in-plane ϕ scans show that the $SrRuO_3$ films on Si substrates inherit the biaxial texture of the IBAD MgO buffer layer, with full-width at half-maximum values of 4.3° and 9.7°, respectively. This approach led to the direct synthesis of a $PbTiO_3/SrRuO_3/MgO/Si_3N_4/Si$ heterostructure, allowing for direct integration of active ferroelectric layers onto Si-based substrates, complete with oxide electrodes for fatigue-free performance.

Chapter 5

Compositionally-Graded Ferroelectrics

5.1 Introduction

Ferroelectric thin films, especially those made of $Ba_xSr_{1-x}TiO_3$ (BST), have recently emerged as candidate materials for tunable components in frequency-agile RF and microwave devices that benefit from their high dielectric constants and related high tunability (Potrepka et al., 2006; Cole et al., 2003; Acikel et al., 2002; Serraiocco et al., 2002, 2003; Xu et al., 2005). However, the dielectric behavior of these materials depends very strongly on temperature near the Curie temperature, T_c. This means that, for conventional ferroelectrics, the dielectric properties of the tunable devices may drift strongly depending on ambient conditions. In tunable filters, for instance, this would be unacceptable since the resonant frequency varies directly with changes in the dielectric constant (Zhu et al., 2002b).

Currently, only few materials satisfy the stringent requirements of low losses and temperature-stability for dielectric resonators and filters in cellular base stations and hand held devices. These materials are in the low to medium dielectric constant

range (Vanderah, 2002). A high dielectric would aid in miniaturizing the microwave components (length of waves is inversely proportional to frequency and root of the dielectric constant).

In short, ferroelectrics are both highly tunable and possess high dielectric constants, but an equally important challenge emerges: the need for a low temperature dependence of the dielectric constant over the operating temperature range (Tagantsev et al., 2003) instead of sharp peaks at the phase transition.

Compositionally graded $Ba_xSr_{1-x}TiO_3$ thin films have been investigated as a means of overcoming this temperature instability. The Curie temperature spans a broad range depending on composition. Therefore, the idea is that the heterogeneous structure would result in a diffuse phase transition and a high dielectric constant over a wide range of temperatures, corresponding to different Curie temperatures for the different regions. Recent experimental efforts have established the promise of this approach (Zhu et al., 2002b; Lu et al., 2003; Zhu et al., 2005; Slowak et al., 1999), and modeling efforts have followed in this direction (Ban et al., 2003; Zhong et al., 2005). The models solve for the polarization of one-dimensional systems and subsequently (separately) compute the effective dielectric behavior by summing capacitances. However, experimental results also show the importance of capacitor geometry (Slowak et al., 1999). The placement of the electrodes and the compositional grading give rise to a complex coupling between the polarization and the electrostatic fields. Therefore, there is a need to extend this to more complex systems by taking into account the electrostatic fields, polarization distribution, and geometry in an integrated manner.

This motivates us to address the graded thin film problem using a continuum model that takes into account the spatial variation in properties and the long-range electrostatic interactions. We present an integrated model that allows us to compute the built-in electric potential, polarization gradient, and electrode charges both in the presence and absence of externally applied electrical field. This approach enables the direct calculation of the temperature-dependent dielectric behavior for different compositional gradings and device geometries. We seek an understanding of the combinatorial behavior of ferroelectric heterostructures and provide results that are useful as design tools for the emerging functionally graded devices.

5.2 Model

We start by considering the continuum energy of a ferroelectric crystal (Shu and Bhattacharya, 2001) occupying a region Ω in space:

$$E = \int_{\Omega} (U(\nabla \mathbf{p}) + W(\mathbf{p}, \mathbf{x}, T)) d\Omega + \frac{\epsilon_o}{2} \int_{\mathbb{R}^3} |\nabla \phi|^2 dV \tag{5.1}$$

Here, U is the energy density associated with the presence of a polarization gradient, and we take it to be of the form $U(\nabla \mathbf{p}) = \frac{a_0}{2} |\nabla \mathbf{p}|^2$. The constant a_0 is related to the physical dimension across which polarization changes take place and is set to 10^{-9} $\mathrm{Vm^3C^{-1}}$, corresponding to a few nanometers (Xiao, 2004). W is the Devonshire-Ginzburg-Landau (DGL) energy density expanded in powers of the polarization, $\mathbf{p}$, the coefficients being functions of temperature and composition, i.e., position in a

graded film:

$$W = \frac{a_1(x_2,T)}{2}(p_1^2+p_2^2)+\frac{a_2(x_2,T)}{2}(p_1^4+p_2^4)+\frac{a_3(x_2,T)}{2}p_1^2p_2^2+\frac{a_4(x_2,T)}{2}(p_1^6+p_2^6) + \frac{a_5(x_2,T)}{4}p_1^4p_2^4, \tag{5.2}$$

where x_2 is along the thickness direction of the film and p_1 and p_2 are the two components of polarization. The last term in equation (5.1) is the electrostatic energy associated with the electric field, $\mathbf{E} = -\nabla\phi$, and can be obtained by solving Gauss's equation:

$$\nabla.(\mathbf{p} - \epsilon_o\nabla\phi) = 0 \text{ in } \mathbb{R}^3, \tag{5.3}$$

with voltage specified at the electrodes and decaying at infinity in the surrounding medium. By taking the first variation of the energy to be zero (Zhang and Bhattacharya, 2005):

$$\nabla\cdot\left(\frac{\partial U}{\partial(\nabla\mathbf{p})}\right)-\frac{\partial W}{\partial\mathbf{p}}-\nabla\phi = 0 \quad \text{in } \Omega \quad \text{with} \quad \nabla\mathbf{p}\cdot\mathbf{n} = 0 \text{ on } \partial\Omega. \tag{5.4}$$

Equations (5.3) and (5.4) represent the equilibrium equations of our system. and we need to solve them simultaneously for a given geometry and composition distribution.

Of special interest is the effect of capacitor geometry, since experiments suggest different dielectric behaviors with temperature for the parallel plate and interdigitated electrode configurations (Slowak et al., 1999). Here we consider two geometries illustrated schematically in Figure 5.1. The first is a film graded along the entire thickness of the film and completely shielded by two parallel plate electrodes (PE).

Coefficient	$BaTiO_3$	$SrTiO_3$	$PbTiO_3$
a_1	$6.6 \times 10^5(T - 110)$	$1.41 \times 10^6(T + 253)$	$9.04 \times 10^5(T - 479)$
a_2	$1.44 \times 10^7(T - 175)$	8.4×10^9	-3.116×10^8
a_3	3.94×10^9	3.94×10^9	3.94×10^9
a_4	3.96×10^{10}	3.96×10^{10}	1.584×10^9
a_5	2.39×10^{14}	2.39×10^{14}	2.39×10^{14}

Table 5.1: DGL coefficients for $BaTiO_3$, $SrTiO_3$, and $PbTiO_3$ used in this report from (Zhang and Bhattacharya, 2005; Pertsev et al., 1998; Ban et al., 2003; Rossetti et al., 1998). All coefficients given in SI units and temperature in °C.

The second is a graded film with interdigitated electrodes (IDE), and the compositional grading occurs in the region where the electric field penetrates into the film. In both cases, PE and IDE, we look for solutions with the polarization aligned with the applied nominal applied field and use the same range of compositions.

For the PE configuration in one dimension, W from equation (5.2) becomes:

$$W = \frac{a_1(x_2, T)}{2} p_2^2(x_2) + \frac{a_2(x_2, T)}{4} p_2^4(x_2) + \frac{a_4(x_2, T)}{6} p_2^6(x_2), \tag{5.5}$$

and equations (5.3) and (5.4) are applied in one dimension to become:

$$\begin{aligned} &a_o \frac{d^2 p_2}{dx_2^2} - a_1(x_2, T) p_2(x_2) - a_2(x_2, T) p_2^3(x_2) - a_4(x_2, T) p_2^5(x_2) - \frac{d\phi}{dx_2} = 0, \\ &\text{with } \frac{dp_2}{dx_2}(0) = 0 \text{ and } \frac{dp_2}{dx_2}(t) = 0 \end{aligned} \tag{5.6}$$

and

$$\frac{dp_2}{dx_2} - \epsilon_o \frac{d^2\phi}{dx_2^2} = 0 \text{ with } \phi(0) = 0 \text{ and } \phi(t) = \phi_t, \tag{5.7}$$

where t is the thickness of the film. The bottom electrode is kept grounded, while a

potential ϕ_t is imposed on the top plate.

For the IDE configuration, the ferroelectric is not completely shielded, allowing electric field to be generated outside the device. Under these conditions, the electrostatics must be solved over *all of space*. Equations (5.3) and (5.4) are applied in two dimensions with a boundary element technique that enables us to address realistic device geometries (Dayal, 2006).

The heterogeneity of the ferroelectric is taken into account by making a_1, a_2, and a_4 spatially-dependent in the equations above. Table 5.1 lists the coefficients for $BaTiO_3$, $SrTiO_3$, and $PbTiO_3$. We linearly interpolate for the intermediate compositions ($0 \leq x \leq 1$) in the graded structure, while a_3 and a_5 are chosen to retain a reasonable energy barrier for polarization switching (Zhang and Bhattacharya, 2005).

The procedure outlined here allows us to calculate the polarization and electric field at any point. To calculate the dielectric behavior, one can compute the charge induced on the ferroelectric/metal boundary. For the PE geometry:

$$\sigma_0 = \left(p_2 - \epsilon_o \frac{d\phi}{dx_2} \right)_{x_2=0}, \sigma_t = \left(\epsilon_o \frac{d\phi}{dx_2} - p_2 \right)_{x_2=t}. \tag{5.8}$$

The difference in free charge, $\Delta\sigma$, between zero and small applied field, ϕ_t, is used to compute the capacitance at a specific temperature. The capacitance is similarly calculated for the IDE geometry, at the specific locations of the co-planar electrodes.

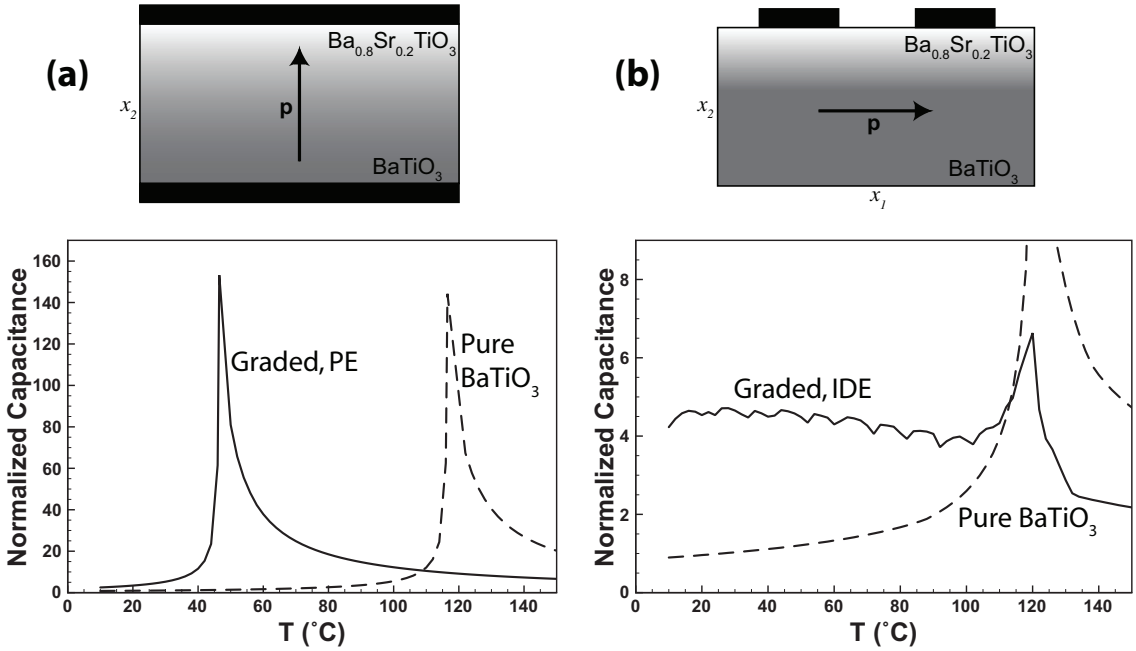

Figure 5.1: The dielectric response vs. temperature for two cases of 200nm graded $BaTiO_3$-$Ba_{0.8}Sr_{0.2}TiO_3$ capacitors: (a) parallel electrodes (PE) and (b) interdigitated electrodes (IDE). The desired stability is achieved for a wide range of operating temperatures in the IDE geometry with an a-axis film. Moreover, the capacitance is enhanced by a factor of ~ 5 compared to the already-high capacitance of pure $BaTiO_3$.

5.3 Results and Discussion

We now examine the results for a 200nm pure $BaTiO_3$ film (as a test of the procedure and for reference) as well as a 200nm graded BST thin film. The endpoints of compositional grading are $BaTiO_3$ at the bottom and $Ba_{0.8}Sr_{0.2}TiO_3$ at the top. In the PE geometry, the grading extends linearly from one electrode to the other, while in the IDE configuration, this linear grading occupies the top third of the film, which is the extent of significant field penetration under the chosen electrode/grading geometry. The temperature dependence of the capacitance is presented in Figure 5.1 for both configurations of graded films. The calculated capacitance is normalized by the

room temperature capacitance of $BaTiO_3$ due to the ambiguity of defining a common intensive quantity such as dielectric constant to compare both geometries. Therefore, we choose to normalize the results such that the room temperature normalized capacitance of pure $BaTiO_3$ is unity at room temperature for both cases.

In both configurations, the method produces the expected transition temperature and dielectric peak for pure $BaTiO_3$ at 120°C. The graded film behavior, however, differs for the PE and IDE geometries. The PE-graded film merely experiences a temperature shift of the dielectric peak, such that the transition occurs between the Curie temperatures of the two extreme compositions. In other words, the parallel plate geometry in combination with a *c*-axis film does not lead to a broadening of the phase transition, but the film behaves like a conventional ferroelectric, with a T_c intermediate between those of the composition end-points. That is not the case for the IDE graded film, where the capacitance displays a high and flat response over a wide temperature range. The compositional grading with the IDE geometry results in the desired broad transition. Small irregularities can be seen in the dielectric response due to the approximation of a linear grading as a series of step changes in composition. This physically corresponds to a multilayer ferroelectric film. These small suppressed transitions are physical and have been found experimentally (Lu et al., 2003).

This result emphasizes the influence of the geometry on the dielectric behavior, specifically for a system where the electrostatics plays a major role. To examine this effect in detail, we now study the computed polarization and electric potential for both geometries under zero applied field and room temperature. The field in the

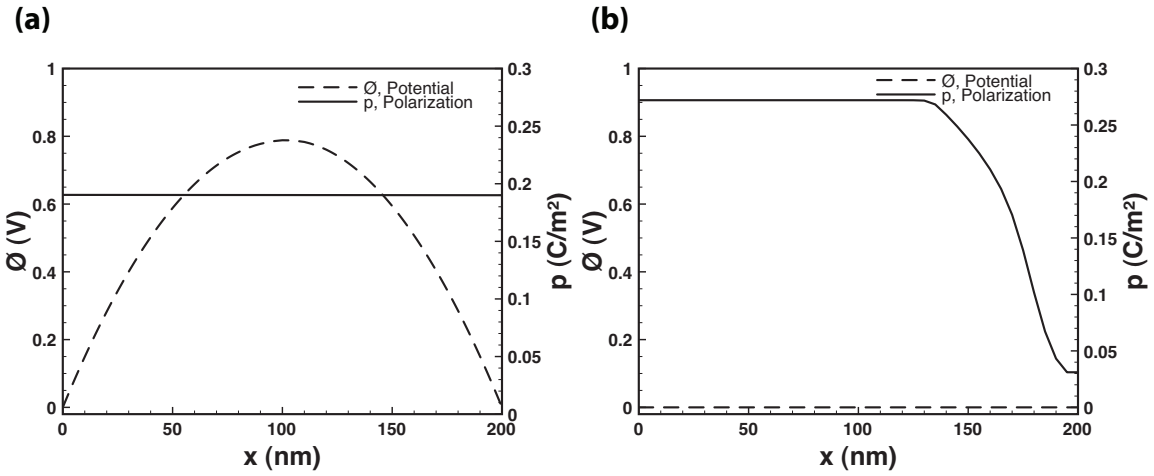

Figure 5.2: Calculated room temperature spontaneous polarization and built-in potential for a) 200nm graded $BaTiO_3$-$Ba_{0.8}Sr_{0.2}TiO_3$ thin film, used in the PE geometry, and b) a 200nm graded $BaTiO_3$-$Ba_{0.8}Sr_{0.2}TiO_3$ film, used in the IDE geometry. In the PE geometry, the compositional grading does not lead to a polarization gradient due to the strong electrostatic interactions manifested by the large built-in potential, or depolarizing field. A polarization gradient is achieved in the IDE capacitor corresponding to multilayer parallel capacitances with weak interactions between the different layers.

film is an inherently built-in one and is commonly referred to in the literature as the depolarizing field. The computed polarization and potential profiles are displayed in Figure 5.2 for the BST graded films of both geometries. In the PE geometry, Figure 5.2(a), the polarization decreases, but very slightly along the x_2 direction. The compositional gradient does not lead to the polarization gradient expected from the bulk spontaneous polarization of compositions between pure $Ba_{0.8}Sr_{0.2}TiO_3$ and $BaTiO_3$ due to the electrostatic interactions. The slight polarization change is accompanied by a large built-in field. This graded structure behaves in effect as a single ferroelectric system instead of an aggregate of different ferroelectric layers. These results directly affect the dielectric properties of the film, making it behave like a homogeneous ferroelectric, as is evidenced by Figure 5.1 above.

The behavior of the graded BST film in the IDE geometry stands in sharp contrast to the PE case, Figure 5.2(b). Specifically, the polarization displays a large gradient in the top third of the film, where the grading is present and there is negligible depolarizing field. The result is a broad phase transition with temperature, as is shown in Figure 5.1 and desired for tunable filter applications.

The influence of the geometry can also be understood as the difference between series capacitances (PE configuration) and parallel capacitances (IDE configuration). In the IDE parallel capacitances case, a large part of the applied field is *across* the compositionally-graded layers, as evidenced by the potential contours in Figure 5.3. In this geometry, the field is entirely due to the applied potential on the left surface electrode, unlike the PE case where a large built-in potential develops.

It is worth noting that the parallel plate configuration can be easily converted to a parallel capacitance geometry by changing the grading direction of the film, i.e., changing the composition along the *surface* of the film, although that may be more difficult to grow experimentally. Another way to take advantage of the parallel plate configuration while maintaining a compositional gradient along the thickness of the film would be through the use of an *a*-axis film. Using the latter arrangement would reduce the electrostatic interactions of the different layers, allow for polarization gradients through a smaller depolarizing field, and reduce temperature sensitivity. In fact, flat dielectric profiles with temperature have been achieved using compositionally-graded *a*-axis films with parallel electrodes (Zhai et al., 2006). However, this approach has the disadvantage of being prone to switching to a *c*-axis film

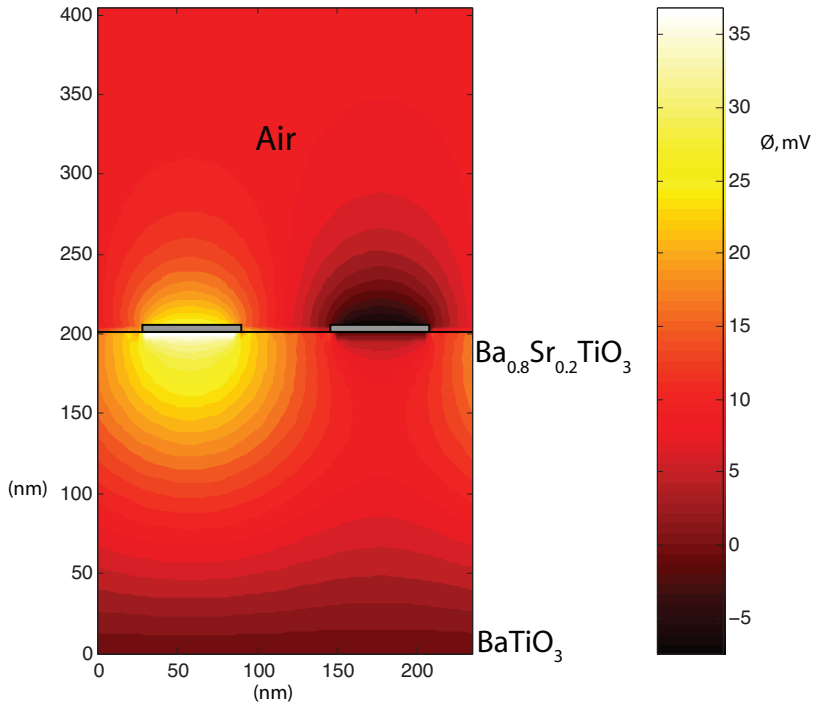

Figure 5.3: A contour of the calculated room temperature potential, due to an applied field on the left electrode of a 200nm graded $BaTiO_3$-$Ba_{0.8}Sr_{0.2}TiO_3$ film, used in the IDE geometry.

at larger bias voltages, which would be undesired. Therefore, it is possible to conclude that the compositionally graded a-axis film with co-planar electrodes provides the best combination of stability with respect to bias and temperature insensitivity (Figure 5.5).

In the results detailed above for modestly graded BST in the PE geometry, we confirmed that the one-dimensional analysis (equations (5.6) and (5.7)) was adequate to capture the dielectric behavior by comparing with two-dimensional calculations performed on the same system. However, when analyzing aggressive polarization gradings such as $PbTiO_3$-$BaTiO_3$ (spontaneous polarization, P_s, of $75\mu C/m^2$ and

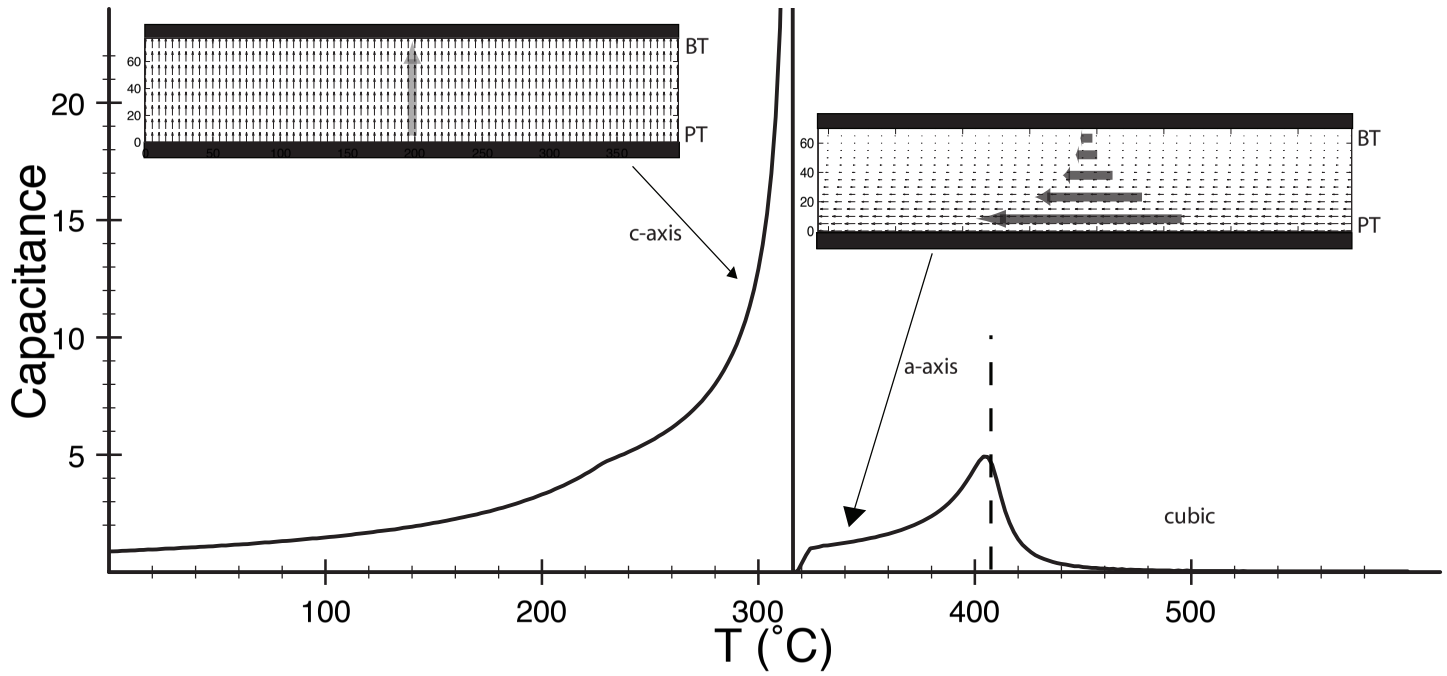

Figure 5.4: The dielectric response of a graded 200nm $PbTiO_3$-$BaTiO_3$ thin film. Aggressive compositional grading can lead to switching of polarization components upon applying an electric field, even for the parallel plate electrodes geometry, as evidenced by the sample computed polarization vectors before and after 300°C. Starting with a c-axis film and until ~ 300°C, a large built-in potential accumulates in the film, and a small polarization gradient along the thickness of the film is observed. Switching to an a-axis film allows for a larger polarization gradient, until finally the entire film transitions to the cubic state.

$25\mu C/m^2$, respectively, at room temperature), we noted switching behavior for the PE geometry that cannot be captured using the simple 1D model. Figure 5.4 illustrates the capacitance behavior of a graded c-axis $PbTiO_3$-$BaTiO_3$ thin film between two parallel electrodes. Below $\sim 300°C$, the graded film has a small polarization gradient and a large built-in potential, as is predicted by the one-dimensional approach (for example Figure 5.2). Above 300°C, this profile becomes unstable and switches to an a-axis film. This transition rids the film of the depolarizing field and allows a larger polarization gradient, as is illustrated in the inset of Figure 5.4, which represents the calculated polarization vector field at 326°C. At higher temperatures the entire film finally transitions into the paraelectric state. These results suggest that switching must be taken into account for films with large polarization grading, as it may strongly influence the overall dielectric response. The simple one-dimensional approach only predicts a ferroelectric-paraelectric phase transition at 300 °C, but not the switching that acts to relieve the film of the large cost of electrostatic interactions between the c-axis graded layers.

5.4 Conclusion

To conclude, we presented a continuum model that accounts for the spatial variation in properties and the long-range electrostatic interactions in functionally graded ferroelectric thin films, with an emphasis on the dielectric behavior. Two geometries are emphasized as case studies: parallel electrode and interdigitated electrode configurations. In both cases, we look for solutions of the polarization nominally

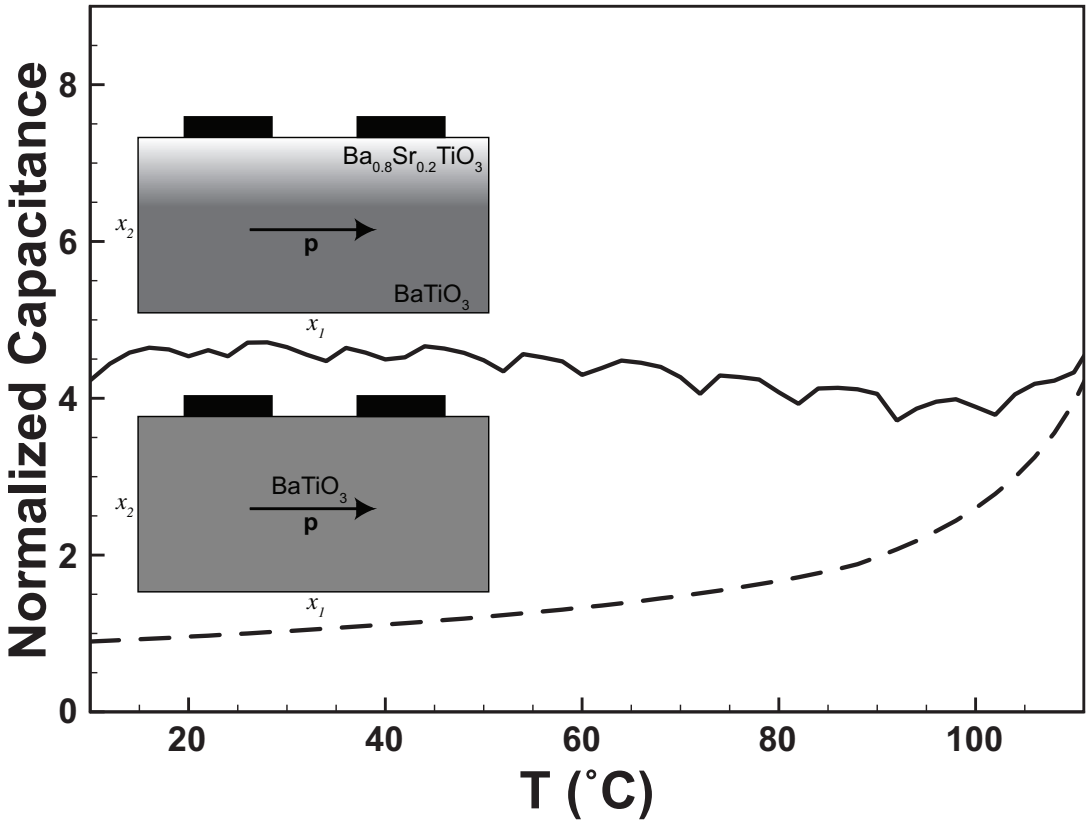

Figure 5.5: Temperature-insensitivity and high capacitance achieved in a graded ferroelectric BST capacitor via interdigitated electrodes.

aligned with the applied electric field and compute the temperature-dependent dielectric response. We find that the parallel electrodes configuration results in a strong temperature-dependence of the dielectric constant due to the strong electrostatic interactions between the different layers. On the other hand, interdigitated electrodes lead to a parallel capacitance geometry that results in a broad phase transition with temperature, as is desired for tunable filter applications. Figure 5.5 illustrates the temperature stability and high capacitance of such a device compared to a pure film of $BaTiO_3$ over a wide range of important operating temperatures.

Furthemore, we commented on the applicability of the one-dimensional approach

to describe the dielectric behavior of graded ferroelectric films. Aggressive compositional grading can lead to switching, which can be taken into account by a two-dimensional model. We expect that these results will be beneficial as design tools for functionally graded tunable devices.

Chapter 6

Conclusion

Ferroelectric materials have been investigated heavily in the last few decades. The focus has mainly been on ferroelectricity as a bi-stable phenomenon for memory applications and on the associated direct piezoelectric coupling in the linear regime for sensors/actuators. This thesis has investigated two more recent topics concerning the connection between structure and property in ferroelectric materials for the benefit of specific applications.

The first topic stems from recent strategies designed to enhance the traditionally limited strains available from ferroelectrics. One design calls for the manipulation of ferroelectric microstructure (domains) to generate large strains by combining mechanical and electrical loading to create competition between microstructural variants (Shu and Bhattacharya, 2001). While large strains have been generated from $BaTiO_3$ single crystals this way (Burcsu et al., 2000), this approach is yet to be demonstrated in miniaturized (thin film) form. To do so would require the synthesis of highly-textured (ideally single crystal) films with complex crystal structures and nonstoichiometric compositions (Bhattacharya and James, 2005).

Chapters 3 and 4 demonstrate the deposition of such a textured ferroelectric sys-

tem ($Pb_xBa_{1-x}TiO_3$) directly on silicon, along with lattice-matching oxide electrodes to enable high-strain actuation on technologically-relevant substrates. This has led to the creation of ferroelectric/$SrRuO_3$/MgO/Si_3N_4/Si heterostructures. The ferroelectric layer is deposited by metalorganic chemical vapor deposition (MOCVD) and is the functional layer in the heterostructure. $SrRuO_3$, grown by pulsed laser deposition (PLD), is the oxide electrode that allows us to electrically address the active layer, but is also a highly-textured template. Both the ferroelectric and oxide electrode layers are found to inherit the biaxial texture of the underlying MgO template which can be deposited by ion beam-assisted deposition (IBAD) directly on the amorphous layers (such as Si_3N_4), commonly available during back-end processing of silicon wafers. In addition, we demonstrated control of the ferroelectric film stoichiometry using a spectroscopic control loop that monitors the ultraviolet spectra of the gas-phase MOCVD precursors during growth.

In addition to the synthesis, we explored the microstructural details of these materials. Specifically, we correlated the presence or absence of 90° domain boundaires in the ferroelectric to the grain size, using x-ray and electron backscatter diffraction (EBSD). High temperature x-ray characterization allowed us to directly observe microstructural changes with temperature that are consistent with domain switching. Furthermore, the stress was measured *in situ* during deposition and thermal cycling of $Pb_xBa_{1-x}TiO_3$ on single crystal MgO, and the results suggest that the rate of stress accumulation (due to lattice and thermal expansion coefficient mismatch) decreases upon transition to the ferroelectric tetragonal state, but the stress relaxation is not

complete. The ability to measure stress during processing is a great advantage since final performance is tied to the stress history of any device.

In ongoing and future work, it will be beneficial to examine in detail the effect of texture on ferroelectric device performance. Specifically: is the degree of biaxial texture achieved here, using an assortment of deposition methods, enough to generate the theoretically expected high strains, or must the films used be essentially single crystals? This issue can be examined experimentally and theoretically using devices of varying degrees of texture and by studying the effect of grain boundaries of various angles on the mobility of ferroelectric domains.

The second topic of the thesis is motivated by the recent upsurge of interest in using ferroelectrics in microwave circuit applications. Thin films of $Ba_xSr_{1-x}TiO_3$ have been studied as microwave components, due to their high dielectric constants (200-300), high tunability (effect of applied DC bias on capacitance) and relatively low loss tangents ($\tan\delta < 0.01$) (Xu et al., 2004). These unique properties can enable compact DC blocking capacitors and tunable filters in the rf and microwave regime, but the dielectric behavior in ferroelectrics is very sensitive to changes in temperature, especially near the ferroelectric-paraelectric phase transition where the dielectric constant and tunability are highest. Compositionally-graded ferroelectric films have been experimentally investigated to reduce this sensitivity, where the compositional heterogeneity along the growth direction would result in a diffuse phase transition and a high but smooth dielectric response over a wide temperature range that encompasses the transition temperatures of the individual layers.

Chapter 5 examined the graded film problem using a continuum model that accounts for the spatial variation in properties and the long range electrostatic interactions. The model is an integrated one in the sense that it allows for direct computation of the built-in electric potentials, polarization gradients, as well as the overall capacitive behavior in the presence and absence of externally-applied electric fields. We examined two geometries as case studies: parallel electrodes and interdigitated electrode configurations with graded $Ba_xSr_{1-x}TiO_3$ thin films. We find that the parallel electrode configuration results in high temperature sensitivity of the dielectric constant due to strong electrostatic interactions between the c-axis layers that strongly suppresses polarization gradients. Interdigitated electrodes used on a-axis poled coplanar capacitors, however, lead to a parallel capacitance configuration resulting a broad phase transition, as is desired for many applications.

In future work on graded ferroelectric capacitors, it will be necessary to experimentally and systematically validate the role of geometry explored in this thesis. This will involve the growth of graded ferroelectric heterostructures (for example by the composition control method used to grow ferroelectrics in Chapter 3) and detailed microstructural characterization that determines the nature of the grading and polarization state of the sample to compare with the right computations. The role of stress is yet to be examined in this model. While simplified models do exist to account for internal mismatch strains and bending in one dimension, the incorporation of a detailed elasticity calculation in two dimensions alongside this model may be critical to understanding how stress affects graded ferroelectrics, specifically those with high

tetragonality and complex domain patterns. This is especially important for the interdigitated electrode configuration that is found to be most effective in redressing the temperature sensitivity of graded capacitors.

Bibliography

Acikel, B., Taylor, T. R., Hansen, P. J., Speck, J. S., York, R. A., 2002. A new high performance phase shifter using $Ba_xSr_{1-x}TiO_3$ thin films. IEEE Microw. Wireless Compon. Lett. 12, 237–239.

Alpay, S. P., Roytburd, A. L., 1998. Thermodynamics of polydomain heterostructures. III. Domain stability map. J. Appl. Phys. 83 (9), 4714–4723.

AlShareef, H. N., Dimos, D., Warren, W. L., Tuttle, B. A., 1997. A model for optical and electrical polarization fatigue in $SrBi_2Ta_2O_9$ and $Pb(Zr,Ti)O_3$. Integr. Ferroelectr. 15, 53–67.

Antognazza, L., Char, K., Geballe, T. H., King, L. L. H., Sleight, A. W., 1993. Josephson coupling of $YBa_2Cu_3O_{7-x}$ through a ferromagnetic barrier $SrRuO_3$. Appl. Phys. Lett. 63, 1005–1007.

Ban, Z. G., Alpay, S. P., Mantese, J. V., 2003. Fundamentals of graded ferroic materials and devices. Phys. Rev. B 67.

Bhattacharya, K., DeSimone, A., Hane, K. F., James, R. D., Palmstrom, C. J., 1999. Tents and tunnels on martensitic films. Mat. Sci. Eng. B-Solid 275, 685–689.

Bhattacharya, K., James, R. D., 1999. A theory of thin films of martensitic materials with applications to microactuators. J. Mech. Phys. Solids 47 (3), 531–576.

Bhattacharya, K., James, R. D., 2005. The material is the machine. Science 307, 53–54.

Boyd, D. A., El-Naggar, M., Goodwin, D., 2006. In situ measurements of stress with temperature in thin film $Pb_xBa_{1-x}TiO_3$. Integr. Ferroelectr.Accepted for publication.

Boyd, D. A., El-Naggar, M. Y., Goodwin, D. G., 2005. In situ measurements of macroscopic film stress during growth, cooling, and thermal cycling of thin film PbTiO3. Integr. Ferroelectr. 71, 21+.

Brewer, R., 2004. Quantitative Biaxial Texture Analysis with Reflection High-Energy Electron Diffraction for Ion Beam-Assisted Deposition of MgO and Heteroepitaxy of Perovskite Ferroelectrics. Ph.D. thesis, California Institute of Technology.

Brewer, R. T., Boyd, D. A., El-Naggar, M. Y., Boland, S. W., Park, Y. B., Haile, S. M., Goodwin, D. G., Atwater, H. A., 2005. Growth of biaxially textured $Ba_xPb_{1-x}TiO_3$ ferroelectric thin films on amorphous Si_3N_4. J. Appl. Phys. 97 (3), art. No. 034103.

Burcsu, E., Ravichandran, G., Bhattacharya, K., 2000. Large strain electrostrictive actuation in barium titanate. Appl. Phys. Lett. 77, 1698–1700.

Burns, G., 1974. Lattice modes in ferroelectric perovskites 2. $Pb_{1-x}Ba_xTiO_3$ including $BaTiO_3$. Phys. Rev. B 10 (5), 1951–1959.

Chase, D. R., Chen, L. Y., York, R. A., 2005. Modeling the capacitive nonlinearity in thin-film BST varactors. IEEE T. Microw. Theory 53, 3215–3220.

Chateigner, D., Wenk, H. R., Patel, A., Todd, M., Barber, D. J., 1998. Analysis of preferred orientations in PST and PZT thin films on various substrates. Integr. Ferroelectr. 19 (1-4), 121–140.

Chen, C. L., Cao, Y., Huang, Z. J., Jiang, Q. D., Zhang, Z., Sun, Y. Y., Kang, W. N., Dezaneti, L. M., Chu, W. K., Chu, C. W., 1997. Epitaxial $SrRuO_3$ thin films on (001) $SrTiO_3$. Appl. Phys. Lett. 71, 1047–1049.

Chen, Y. F., Chen, J. X., Shun, L., Yu, T., Li, P., Ming, N. B., Shi, L. J., 1995. Preparation of epitaxial $PbTiO_3$ thin-films by metalorganic vapor-phase epitaxy under reduced pressure. J. Cryst. Growth 146 (1-4), 624–629.

Chrisey, D. B., Hubler, G. K. (Eds.), 2004. Pulsed Laser Deposition of Thin Films. John Wiley & Sons, Inc.

Cole, M. W., Nothwang, W. D., Hubbard, C., Ngo, E., Ervin, M., 2003. Low dielectric loss and enhanced tunability of $Ba_0.6Sr_0.4TiO_3$ based thin films via material compositional design and optimized film processing methods. J. Appl. Phys. 93, 9218–9225.

Cullity, B., 1978. Elements of X-ray Diffraction. Addison-Wesley.

Dahmen, K. H., Gerfin, T., 1993. MOCVD of high Tc superconducting materials. Prog. Cryst. Growth Ch. 27, 117–161.

Damjanovic, D., 1998. Ferroelectric, dielectric and piezoelectric properties of ferroelectric thin films and ceramics. Rep. Prog. Phys. 61, 1267–1324.

Dayal, K., 2006. Nonlocal microstructural mechanics of active materials. Ph.D. thesis, California Institute of Technology.

De Veirman, A., Cillessen, J., De Keijser, M., Wolf, R., Taylor, D., Staals, A., Dormans, G. J. M., 1994. Epitaxial oxide thin films and heterostructures. In: Fork, D., Phillips, J., Ramesh, R., Wolf, R. (Eds.), Mat. Res.Soc. Symp. Proc. Vol. 341. Materials Research Society, San Francisco, pp. 329–340.

DeFlaviis, F., Alexopoulos, N. G., Stafsudd, O. M., 1997. Planar microwave integrated phase-shifter design with high purity ferroelectric material. IEEE T. Microw. Theory 45, 963–969.

Dekeijser, M., Deleeuw, D. M., Vanveldhoven, P. J., Deveirman, A. E. M., Neerinck, D. G., Dormans, G. J. M., 1995. The structure of heteroepitaxial lead titanate layers grown by organometallic chemical-vapor-deposition. Thin Solid Films 266 (2), 157–167.

Desisto, W. J., Rappoli, B. J., 1998. Ultraviolet absorption sensors for precursor delivery rate control for metalorganic chemical vapor deposition of multiple component oxide thin films. J. Cryst. Growth 191 (1-2), 290–293.

Devonshire, A. F., 1949. Theory of barium titanate -1-. Philos. Mag. 40, 1040–1063.

Devonshire, A. F., 1951. Theory of barium titanate -2-. Philos. Mag. 42, 1065–1079.

Devonshire, A. F., 1954. Theory of ferroelectrics. Adv. Phys. 3, 85–130.

Didomenico, M., Pantell, R. H., Johnson, D. A., 1962. Ferroelectric harmonic generator and large-signal microwave characteristics of a ferroelectric ceramic. J. Appl. Phys. 33, 1697–1706.

Duiker, H. M., Beale, P. D., Scott, J. F., Dearaujo, C. A. P., Melnick, B. M., Cuchiaro, J. D., Mcmillan, L. D., 1990. Fatigue and switching in ferroelectric memories - theory and experiment. J. Appl. Phys. 68, 5783–5791.

Eom, C. B., Cava, R. J., Fleming, R. M., Phillips, J. M., Vandover, R. B., Marshall, J. H., Hsu, J. W. P., Krajewski, J. J., Peck, W. F., 1992. Single-crystal epitaxial thin-films of the isotropic metallic oxides $Sr_{1-x}Ca_xRuO_3$. Science 258, 1766–1769.

Eom, C. B., Vandover, R. B., Phillips, J. M., Werder, D. J., Marshall, J. H., Chen, C. H., Cava, R. J., Fleming, R. M., Fork, D. K., 1993. Fabrication and properties of epitaxial ferroelectric heterostructures with $SrRuO_3$ isotropic metallic oxide electrodes. Appl. Phys. Lett. 63, 2570–2572.

Fatuzzo, E., Merz, W., 1967. Selected Topics in Solid State Physics: Ferroelectricity, E.P. Wohlfarth, Ed. North-Holland Publishing Co., Amsterdam.

Flinn, P. A., Gardner, D. S., Nix, W. D., 1987. Measurement and interpretation of

stress in aluminum-based metallization as a function of thermal history. IEEE T. Electron. Dev. 34, 689–699.

Foster, C., Pompe, W., Daykin, A., Speck, J., 1996. Relative coherency strain and phase transformation history in epitaxial ferroelectric thin films. J. Appl. Phys. 79 (3), 1405–1415.

Foster, C. M., Li, Z., Buckett, M., Miller, D., Baldo, P. M., Rehn, L. E., Bai, G. R., Guo, D., You, H., Merkle, K. L., 1995. Substrate effects on the structure of epitaxial pbtio$_3$ thin films prepared on mgo, laalo$_3$, and srtio$_3$ by metalorganic chemical-vapor deposition. J. Appl. Phys. 78 (4), 2607.

Gao, Y., Bai, G., Merkle, K. L., Chang, H. L. M., Lam, D. J., 1993. Effects of substrate orientation and cooling rate on microstructure of $PbTiO_3$ thin-films grown by metal-organic chemical-vapor-deposition. Thin Solid Films 235 (1-2), 86–95.

Hammond, K. D., 2003. Temperature sensing by in-situ infrared spectroscopy in a chemical vapor deposition reactor. Senior Thesis, California Institute of Technology.

Hsu, W. Y., Raj, R., 1995. X-ray characterization of the domain-structure of epitaxial lead titanate thin-films on (001)-strontium-titanate. Appl. Phys. Lett. 67 (6), 792–794.

Hull, R. (Ed.), 1999. Properties of Crystalline Silicon. Institute of Electrical Engineers, London.

Jaffe, B., Cook, W. R., Jaffe, H. L. (Eds.), 1971. Piezoelectric Ceramics. Non-metallic solids, v. 3. Academic Press, London, New York,.

Jia, Q. X., Foltyn, S. R., Arendt, P. N., Groves, J. R., Holesinger, T. G., Hawley, M. E., Lu, P., 2002. Role of $SrRuO_3$ buffer layers on the superconducting properties of $YBa_2Cu_3O_7$ films grown on polycrystalline metal alloy using a biaxially oriented MgO template. Appl. Phys. Lett. 81, 4571–4573.

Jia, Q. X., Foltyn, S. R., Arendt, P. N., Holesinger, T., Groves, J. R., Hawley, M., 2003. Growth and characterization of $SrRuO_3$ buffer layer on MgO template for coated conductors. IEEE T. Appl. Supercon. 13, 2655–2657.

Jia, Q. X., Foltyn, S. R., Hawley, M., Wu, X. D., 1997. Pulsed laser deposition of conductive $SrRuO_3$ thin films. J. Vac. Sci. Technol. A 15, 1080–1083.

Jiang, J. C., Tian, W., Pan, X., Gan, Q., Eom, C. B., 1998. Effects of miscut of the $SrTiO_3$ substrate on microstructures of the epitaxial $SrRuO_3$ thin films. Mat. Sci. Eng. B-Solid 56, 152–157.

Kennedy, B. J., Hunter, B. A., 1998. High-temperature phases of $SrRuO_3$. Phys. Rev. B 58, 653–658.

Kim, C. J., Yoon, D. S., Lee, J. S., Choi, C. G., Lee, W. J., No, K., 1994. Electrical characteristics of (100), (111), and randomly aligned lead-zirconate-titanate thin-films. J. Appl. Phys. 76 (11), 7478–7482.

Kim, T. W., Yom, S. S., 1999. Microstructural, electrical, and transmittance proper-

ties of $PbTiO_3$ films grown on p-InP (100) substrates at low temperature. J. Phys. Chem. Solids 60 (7), 935–942.

Koukhar, V. G., Pertsev, N. A., Waser, R., 2001. Thermodynamic theory of epitaxial ferroelectric films with dense domain structures. Phys. Rev. B 64, 214103.

Krulevitch, P., Lee, A. P., Ramsey, P. B., Trevino, J. C., Hamilton, J., Northrup, M. A., 1996. Thin film shape memory alloy microactuators. J. Microelectromech. S. 5 (4), 270–282.

Kwak, B. S., Erbil, A., Budai, J. D., Chisholm, M. F., Boatner, L. A., Wilkens, B. J., 1994. Domain formation and strain relaxation in epitaxial ferroelectric heterostructures. Phys. Rev. B. 49 (21), 14865–14879.

Longo, J. M., Raccah, P. M., Goodenou.jb, W., 1968. Magnetic properties of $SrRuO_3$ and $CaRuO_3$. J. Appl. Phys. 39, 1327.

Lu, S. G., Zhu, X. H., Mak, C. L., Wong, K. H., Chan, H. L. W., Choy, C. L., 2003. High tunability in compositionally graded epitaxial barium strontium titanate thin films by pulsed-laser deposition. Appl. Phys. Lett. 82, 2877–2879.

Malacara, D., Servin, M., Malacara, Z., 1998. Interferogram Analysis for Optical Testing. Marcel Decker, Inc.

Mansour, S., Vest, R., 1992. The dependence of ferroelectric and fatigue behaviors of PZT films on microstructure and orientation. Integr. Ferroelectr. 1, 57–69.

Nakazawa, H., Yamane, H., Hirai, T., 1991. Metalorganic chemical vapor-deposition of $BaTiO_3$ films on MgO (100). Jpn. J. Appl. Phys. 1 30 (9B), 2200–2203.

Okada, M., Takai, S., Amemiya, M., Tominaga, K., 1989. Preparation of c-axis-Oriented $PbTiO_3$ Thin-Films by MOCVD under Reduced Pressure. Jpn. J. Appl. Phys. 1 28 (6), 1030–1034.

Park, S. E., Shrout, T. R., 1997. Ultrahigh strain and piezoelectric behavior in relaxor based ferroelectric single crystals. J. Appl. Phys. 82, 1804–1811.

Pertsev, N., Zembilgotov, A., 1995. Energetics and geometry of 90 degree domain structures in epitaxial ferroelectric and ferroelastic films. J. Appl. Phys. 78 (10), 6170–6180.

Pertsev, N., Zembilgotov, A., 1996. Domain populations in epitaxial ferroelectric thin films: Theoretical calculations and comparison with experiment. J. Appl. Phys. 80 (11), 6401–6406.

Pertsev, N. A., Zembilgotov, A. G., Tagantsev, A. K., 1998. Effect of mechanical boundary conditions on phase diagrams of epitaxial ferroelectric thin films. Phys. Rev. Lett. 80, 1988–1991.

Potrepka, D. M., Hirsch, S., Cole, M. W., Nothwang, W. D., Zhong, S., Alpay, S. P., 2006. Effect of strain on tunability in $Ba_0.60Sr_0.40TiO_3$ thin films on Pt-Si substrates. J. Appl. Phys. 99.

Ramesh, R., Chan, W. K., Wilkens, B., Gilchrist, H., Sands, T., Tarascon, J. M.,

Keramidas, V. G., Fork, D. K., Lee, J., Safari, A., 1992. Fatigue and retention in ferroelectric Y-Ba-Cu-O/Pb-Zr-Ti-O/Y-Ba-Cu-O heterostructures. Appl. Phys. Lett. 61, 1537–1539.

Ren, S. B., Lu, C. J., Liu, J. S., Shen, H. M., Wang, Y. N., 1996. Size-related ferroelectric domain structure transition in a polycrystalline $PbTiO_3$ thin film. Phys. Rev. B. 54 (20), 14337–14340.

Rosakis, A. J., Singh, R. P., Tsuji, Y., Kolawa, E., Moore, N. R., 1998. Full field measurements of curvature using coherent gradient sensing: application to thin film characterization. Thin Solid Films 325, 42–54.

Rossetti, G. A., Cline, J. P., Navrotsky, A., 1998. Phase transition energetics and thermodynamic properties of ferroelectric $PbTiO_3$. J. Mater. Res. 13, 3197–3206.

Ruglovsky, J., Dicken, M., Diest, K., El-Naggar, M., Bolyard, S., Goodwin, D., Ravichandran, G., Bhattacharya, K., Atwater, H., 2006. Surface micromachined ferroelectric MEMS devices: correlating device performance with film microstructure.

Schafer, P., Ritter, S., Ganster, R., Ehrhart, P., Hoffmann, S., Waser, R., 2000. Preparation of $(Pb_xBa_{1-x})TiO_3$ thin films by MOCVD using an aerosol-assisted liquid delivery system. Integr. Ferroelectr. 30 (1-4), 165–173.

Schwartz, A. J., Kumar, M., Adams, B. L. (Eds.), 2000. Electron Backscatter Diffraction in Materials Science. Kluwer Academic, New York.

Scott, J., 2000. Ferroelectric Memories. Springer.

Scott, J. F., Araujo, C. A., Melnick, B. M., Mcmillan, L. D., Zuleeg, R., 1991. Quantitative measurement of space-charge effects in lead zirconate-titanate memories. J. Appl. Phys. 70, 382–388.

Serraiocco, J., Acikel, B., Hansen, P., Taylor, T., Xu, H., Speck, J. S., York, R. A., 2002. Tunable passive integrated circuits using BST thin films. Integr. Ferroelectr. 49, 161–170.

Serraiocco, J. L., Hansen, P. J., Taylor, T. R., Speck, J. S., York, R. A., 2003. Compact distributed phase shifters at X-band using BST. Integr. Ferroelectr. 56, 1087–1095.

Shirane, G., Hoshino, S., Suzuki, K., 1950a. Crystal structures of lead titanate and of lead-barium titanate. J. Phys. Soc. Jpn. 5 (6), 453–455.

Shirane, G., Hoshino, S., Suzuki, K., 1950b. X-ray study of the phase transition in lead titanate. Phys. Rev. 80 (6), 1105–1106.

Shu, Y. C., Bhattacharya, K., 2001. Domain patterns and macroscopic behaviour of ferroelectric materials. Philos. Mag. B 81, 2021–2054.

Singh, S. K., Lees, M. R., Singh, R. K., Palmer, S. B., 2002. Growth of $SrRuO_3$ thin films on MgO substrates by pulsed laser ablation. J. Phys. D Appl. Phys. 35, 2243–2246.

Slowak, R., Hoffmann, S., Liedtke, R., Waser, R., 1999. Functional graded high-K $(Ba_{1-x}Sr_x)TiO_3$ thin films for capacitor structures with low temperature coefficient. Integr. Ferroelectr. 24, 169–179.

Speck, J., Daykin, A., Seifert, A., 1995. Domain configurations due to multiple misfit relaxation mechanisms in epitaxial ferroelectric thin films. III. Interfacial defects and domain misorientations. J. Appl. Phys. 78 (3), 1696–1706.

Speck, J., Pompe, W., 1994. Domain configurations due to multiple misfit relaxation mechanisms in epitaxial ferroelectric thin films. I. Theory. J. Appl. Phys. 76 (1), 466–476.

Speck, J., Seifert, A., Pompe, W., 1994. Domain configurations due to multiple misfit relaxation mechanisms in epitaxial ferroelectric thin films. II. Experimental verification and implications. J. Appl. Phys. 76 (1), 477–483.

Stoney, G. G., 1909. The tension of metallic films deposited by electrolysis. P. Roy. Soc. Lond. A Mat. A82, 172.

Sun, L., Chen, Y. F., He, L., Ge, C. Z., Yu, T., Zhang, M. S., Ming, N. B., Ding, D. S., Chang, Y. C., 1997. Epitaxial growth of $PbTiO_3$ thin film on (110) $NdGaO_3$ substrate by metalorganic chemical vapor deposition. Z. Phys. B Con. Mat. 102 (4), 479–482.

Sun, L., Chen, Y. F., Yu, T., Ming, N. B., Ding, D. S., Lu, Z. H., 1996. (001) textured $PbTiO_3$ thin films grown on redoping n-Si by metalorganic chemical vapor deposition under reduced pressure. Appl. Phys. A-Mater. 63 (4), 381–384.

Tagantsev, A. K., Sherman, V. O., Astafiev, K. F., Venkatesh, J., Setter, N., 2003. Ferroelectric materials for microwave tunable applications. J. Electroceram. 11, 5–66.

Tischler, J. Z., Budai, J. D., Ice, G. E., Habenschuss, A., Jan 1988. Multiple scattering and the 200 reflection in silicon and germanium. Acta Crystallogr. A 44 (1), 22–25.

Touloukian, Y., Kirby, R., Taylor, R., Lee, T. (Eds.), 1977. Thermal Expansion of Nonmetallic Solids, Vol. 13 of Thermophysical Properties of Matter. IFI/Plenum, New York.

Tripathi, A., 2001. In Situ Diagnostics for Metalorganic Chemical Vapor Deposition of YBCO. Ph.D. thesis, California Institute of Technology.

Vanderah, T. A., 2002. Talking Ceramics. Science 298 (5596), 1182–1184.

Vreeland, T., Dommann, A., Tsai, C.-J., Nicolet, M.-A., 1989. X-ray diffraction determination of stresses in thin films. Mater. Res. Soc. Proc. 130, 3.

Wang, C. P., Do, K. B., Beasley, M. R., Geballe, T. H., Hammond, R. H., 1997. Deposition of in-plane textured MgO on amorphous Si_3N_4 substrates by ion-beam-assisted deposition and comparisons with ion-beam-assisted deposited yttria-stabilized-zirconia. Appl. Phys. Lett. 71 (20), 2955–2957.

Xiao, Y., 2004. The Influence of Oxygen Vacancies on Domain Patterns in Ferroelectric Perovskites. Ph.D. thesis, California Institute of Technology.

Xiao, Y., Shenoy, V. B., Bhattacharya, K., 2005. Depletion layers and domain walls in semiconducting ferroelectric thin films. Phys. Rev. Lett. 95.

Xu, H. T., Pervez, N. K., Hansen, P. J., Shen, L. K., Keller, S., Mishra, U. K., York, R. A., 2004. Integration of $Ba_xSr_{1-x}TiO_3$ thin films with AlGaN/GaN HEMT circuits. IEEE Elec. Device L. 25, 49–51.

Xu, H. T., Pervez, N. K., York, R. A., 2005. Tunable microwave integrated circuits using BST thin film capacitors with device structure optimization. Integr. Ferroelectr. 77, 27–35.

Yoon, Y. S., Yom, S. S., Kim, T. W., Lee, D. U., Kim, C. O., 1996. Improvement of the crystallinity in $PbTiO_3$ films grown on indium tin oxide-coated glass by metalorganic chemical vapor deposition using the continuous cooling process. Appl. Surf. Sci. 93 (4), 285–289.

Yu, T., Chen, Y. F., Shun, L., Chen, J. X., Ming, N. B., 1995. Phase-transition of $PbTiO_3$ polycrystalline thin-film prepared by metalorganic chemical-vapor-deposition on yttrium stabilized zirconium. Solid State Commun. 96 (7), 477–480.

Zakharov, N. D., Satyalakshmi, K. M., Koren, G., Hesse, D., 1999. Substrate temperature dependence of structure and resistivity of $SrRuO_3$ thin films grown by pulsed laser deposition on (100) $SrTiO_3$. J. Mater. Res. 14, 4385–4394.

Zhai, J., Yao, X., Xu, Z., Chen, H., 2006. Ferroelectric properties of $Pb_xSr_{1-x}TiO_3$ and its compositionally graded thin films grown on the highly oriented $LaNiO_3$ buffered $Pt/Ti/SiO_2/Si$ substrates. J. Appl. Phys. 100 (3), art. No. 034108.

Zhang, J. M., Beetz, C. P., Krupanidhi, S. B., 1994. Photoenhanced chemical-vapor-deposition of $BaTiO_3$. Appl. Phys. Lett. 65 (19), 2410–2412.

Zhang, R., 2005. Mechanical characterization of thin films with application to ferroelectrics. Ph.D. thesis, California Institute of Technology.

Zhang, W., Bhattacharya, K., 2005. A computational model of ferroelectric domains. Part I: Model formulation and domain switching. Acta. Mater. 53, 185–198.

Zhong, S., Alpay, S. P., Ban, Z. G., Mantese, J. V., 2005. Dielectric permittivity and pyroelectric response of compositionally graded ferroelectrics. Integr. Ferroelectr. 71, 1–9.

Zhu, X., Chan, H. L. W., Choy, C. L., Wong, K. H., 2002a. Epitaxial growth and dielectric properties of functionally graded $(Ba_{1-x}Sr_x)TiO_3$ thin films with stoichimetric variation. J. Vac. Sci. Technol. A 20, 1796–1801.

Zhu, X. H., Chong, N., Chan, H. L. W., Choy, C. L., Wong, K. H., Liu, Z., Ming, N., 2002b. Epitaxial growth and planar dielectric properties of compositionally graded $(Ba_{1-x}Sr_x)TiO_3$ thin films prepared by pulsed-laser deposition. Appl. Phys. Lett. 80, 3376–3378.

Zhu, X. H., Zhu, J. M., Zhou, S. H., Liu, Z. G., Ming, N. B., Chan, H. L. W., Choy, C. L., Wong, K. H., Hesse, D., 2005. Microstructure and dielectric properties of compositionally-graded $(Ba_{1-x}Sr_x)TiO_3$ thin films. Mat. Sci. Eng. B-Solid 118, 219–224.